REPORT SRL-07-F-1989

COMPACT, LIGHTWEIGHT CO_2 LASERS FOR SDIO APPLICATIONS

AD-A207 052

Principal Investigator
Dr. Jonah Jacob

SCIENCE RESEARCH LABORATORY, INC.
15 Ward Street
Somerville, MA 02143

11 April 1989

FINAL REPORT

Period for September 30, 1988 to March 31, 1989
Contract Number N00014-88-C-0727

APPROVED FOR PUBLIC RELEASE; DISTRIBUTION UNLIMITED

Sponsored by

DTIC
ELECTE
APR 1 3 1989
S D
H

"The views and conclusions contained in this document are those of the authors and should not be interpreted as representing the official policies, either expressed or implied, of the Strategic Defense Initiative Organization or the U.S. Government."

89

REPORT SRL-07-F-1989

COMPACT, LIGHTWEIGHT CO₂ LASERS FOR SDIO APPLICATIONS

Principal Investigator
Dr. Jonah Jacob

SCIENCE RESEARCH LABORATORY. INC.
15 Ward Street
Somerville, MA 02143

11 April 1989

FINAL REPORT

Period for September 30, 1988 to March 31, 1989
Contract Number N00014-88-C-0727

APPROVED FOR PUBLIC RELEASE; DISTRIBUTION UNLIMITED

Sponsored by

SCIENCE RESEARCH LABORATORY

REPORT DOCUMENTATION PAGE

1a. REPORT SECURITY CLASSIFICATION	1b. RESTRICTIVE MARKINGS
Unclassified	

2a SECURITY CLASSIFICATION AUTHORITY	3. DISTRIBUTION/AVAILABILITY OF REPORT
	Approved for Public Release;
2b DECLASSIFICATION/DOWNGRADING SCHEDULE	Distribution Unlimited

4. PERFORMING ORGANIZATION REPORT NUMBER(S)	5. MONITORING ORGANIZATION REPORT NUMBER(S)
SRL-07-F-1989	S405803SRV01/06-22-88 (1112LO)

6a. NAME OF PERFORMING ORGANIZATION	6b. OFFICE SYMBOL (If applicable)	7a. NAME OF MONITORING ORGANIZATION
Science Research Laboratory		Office of Naval Research

6c. ADDRESS (City, State, and ZIP Code)	7b ADDRESS (City, State, and ZIP Code)
15 Ward St.	800 N. Quincy St.
Somerville, MA 02143	Arlington, VA 22217-5000

8a. NAME OF FUNDING/SPONSORING ORGANIZATION	8b. OFFICE SYMBOL (If applicable)	9 PROCUREMENT INSTRUMENT IDENTIFICATION NUMBER
SDIO		N00014-88-C-0727

8c. ADDRESS (City, State, and ZIP Code)	10 SOURCE OF FUNDING NUMBERS			
	PROGRAM ELEMENT NO	PROJECT NO	TASK NO	WORK UNIT ACCESSION NO.
The Pentagon Washington, DC 20301-7100	63220			

11 TITLE (Include Security Classification)

Compact, Lightweight CO_2 Lasers for SDIO Applications

12. PERSONAL AUTHOR(S)
Jonah Jacob

13a. TYPE OF REPORT	13b. TIME COVERED	14. DATE OF REPORT (Year, Month, Day),	15. PAGE COUNT
Final	FROM 9/30/88 TO 3/31/89		

16. SUPPLEMENTARY NOTATION

carbon dioxide

17	COSATI CODES		18. SUBJECT TERMS (Continue on reverse if necessary and identify by block number)
FIELD	GROUP	SUB-GROUP	compact CO_2 lasers, self-sustained discharge
			CO_2 lasers, carbon dioxide lasers.

19. ABSTRACT (Continue on reverse if necessary and identify by block number)

During the past decade, substantial investments have been made in the development of gas discharge pumped CO_2 lasers for military and civilian applications. The DoD community and SDIO in particular is developing compact, lightweight CO_2 lasers for airborne and spaced-based radar applications directed toward target ranging, imaging, and discrimination. These CO_2 laser systems are being developed under the SDIO Lowkater Program, in the Airborne Laser Experiment (ALE) Program by the Army/SDC and in Lincoln Laboratory's space based CO_2 laser radar research and development program. The three major components of a CO_2 laser radar are the laser head and flow loop, the pulsed power system and the optics and beam control system. In this report SRL presents a novel self sustained discharge concept that should result in the stable and efficient extraction of large specific energies (50 J/liter atmosphere) for pulse lengths as long as 100 μs. This factor of ten increase in the energy per unit volume will

20. DISTRIBUTION/AVAILABILITY OF ABSTRACT	21. ABSTRACT SECURITY CLASSIFICATION
☐ UNCLASSIFIED/UNLIMITED ☒ SAME AS RPT ☐ DTIC USERS	Unclassified

22a. NAME OF RESPONSIBLE INDIVIDUAL	22b. TELEPHONE (Include Area Code)	22c. OFFICE SYMBOL

enable laser heads to be fabricated which are factors of 4 to 5 times smaller in volume and weight than with conventional discharge approaches. Further, the reduced cross section of the optical beam will result in a significant reduction in the size and weight of the optics and beam control system.

DTIC
COPY
INSPECTED
4

Accession For	
NTIS GRA&I	☑
DTIC TAB	☐
Unannounced	☐
Justification	
By	
Distribution/	
Availability Codes	

Dist	Avail and/or Special
A-1	

Table of Contents

SCIENCE RESEARCH LABORATORY

Table of Contents (continued)

SCIENCE RESEARCH LABORATORY

List of Illustrations

SCIENCE RESEARCH LABORATORY

SCIENCE RESEARCH LABORATORY

List of Illustrations (Continued)

SCIENCE RESEARCH LABORATORY

CHAPTER 1

INTRODUCTION

During the past decade, substantial investments have been made in the development of compact gas discharge pumped CO_2 lasers for military and civilian applications. The DOD community and SDIO in particular is developing compact, lightweight CO_2 lasers for airborne and space-based radar applications directed toward target ranging, imaging, and discrimination. These CO_2 laser systems are being developed in the LOWKATER and LICD programs.

The three major components of a CO_2 laser radar are the laser head and flow loop, the pulsed power supply and the optics and beam control system. In this proposal SRL will present a novel self-sustained discharge concept that should result in the stable and efficient extraction of large specific energies (50 J/liter atmosphere) for pulse lengths as long as 100 μs. This factor of five increase in the energy per unit volume will enable laser heads to be fabricated which are factors of 4 to 5 times smaller in volume and weight than with conventional discharge approaches. Further the smaller cross section of the optical beam will result in a significant reduction in the size and weight of the optics and beam control system.

The new laser discharge concept proposed by SRL is compatible with SDIO applications which require efficient operation of compact, lightweight CO_2 lasers at kilowatt power levels. This concept is based on a new discharge method which will insure the macroscopic and microscopic stability of the discharge at high pump power density and for long pulse lengths. This discharge concept promises pulse lengths of up to 100 microseconds duration. scalability to multikilowatt high average power, high volumetric efficiency (up to 50 joules/liter-atm), and high electrical efficiency. This new discharge method utilizes spatially-uniform x-ray or UV preionization of the laser medium followed by a discharge pulse which initially supplies a voltage across the discharge electrodes, approximately equal to two or three times the sustaining voltage, to avalanche the electron density uniformly

1-1

to 10^{12} electrons/cm^3. The energy to drive the discharge is supplied by an all solid state rf-modulated driver with high incremental source impedance; that is, the driver acts as a current source to incremental changes in impedance. In this concept, the current source drive prevents discharge instabilities which increase the electron density and therefore the current density in a spatially-uniform manner. In addition, the oscillating discharge voltage prevents localized electron density avalanche by controlling the ionization and recombination during the peaks and valleys of the RF waveform and by limiting, with inductance, the localization of discharge current. A common example of such a localized instability in a flowing CO_2 laser are arcs that occur in the downstream side of the laser cavity where the laser mixtur= is hotter and residual ionization is generated uniformly at the electrode edges. Present methods to minimize this problem rely on increasing the gas flow rate to reduce the ionization level at the edges of the discharge electrodes or utilizing electron beam preionized discharges. Both of these solutions are unacceptable if a reliable compact, lightweight CO_2 laser is required. Increasing the gas flow rate will increase the weight and volume of the laser flow loop. Electron beam preionized laser discharges require a thin foil which separates the vacuum where the electron beam is formed from the high pressure laser mixture. This foil can create reliability problems in cases where long duration operation is required without maintenance. In the remainder of this section, existing self sustained techniques for discharge pumping CO_2 lasers will be reviewed.

The x-ray or UV preionized discharge method utilizes x-ray or UV radiation to provide a low level of spatially uniform electron density which can subsequently be avalanched uniformly by applying sufficiently high electric fields. This avalanching discharge method can typically be made to be stable for long single pulse operation since the spatial preionization contours can be carefully controlled so that discharge arcing does not occur at the edges of the electrodes. However repetitive pulse operation requires flowing the laser medium which carries ionization to the downstream edges of the discharge electrodes. The electric field enhancement at these edges can then trigger discharge instabilities. Therefore, this

1-2

discharge concept may not be compatible with development of compact, efficient CO_2 laser devices for space based applications.

CO_2 waveguide lasers have proven to be useful and compact devices for various tactical military applications. A major advantage of waveguide devices is that they do not rely on flowing the gas to remove the waste heat. The narrow waveguide channel allows for heat removal by conduction through the sidewalls of the waveguide channel. Unfortunately, waveguide lasers have been operated at low pressure (< 100 Torr) and so their utility in laser radar has been severely limited. This low pressure limitation arises because the discharge has to be wall stabilized. In fact, the DOD has made a considerable investment to alleviate this constraint on waveguide laser operation. In addition, pulsed operation of 50-100 watt CO_2 waveguide laser is typically possible only with Q-switching which reduces efficiency somewhat and also reduces reliability.

Science Research Laboratory has developed a new CO_2 laser discharge concept which circumvents the limitations on CO_2 laser performance discussed above. This new discharge concept can provide stable discharge operation for pulse durations up to 100 μsec while providing pump power density consistent with specific laser energy densities of 50 J/liter atmosphere. The key technical issue addressed by this new compact CO_2 laser discharge concept is maintaining discharge stability for pulse durations up to 100 μsec. In this new discharge concept, stability is maintained by two distinct processes. First, a current source is chosen to drive the discharge to prevent spatially uniform ionization instabilities from terminating the discharge. With current source drive, if the electron density increases uniformly, discharge conductivity increases and the voltage across the discharge decreases. Since for CO_2 laser discharges the ionization rate decreases rapidly with decreasing E/N, the ionization rate falls and the discharge is stable. Of course, stabilizing the total discharge current is a necessary, but not sufficient, condition for discharge stability.

Even with constant current drive, instabilities at regions of high electric stress can lead to localized discharge arcing and impedance collapse. To stabilize the discharge against

1-3

instabilities having a small spatial scale size, oscillations are imposed on the current and voltage pulses to prevent constriction of the discharge current. This is accomplished by choosing the oscillating frequency to be sufficiently rapid to allow the inductance of the constriction to suppress current flow until the discharge voltage has dropped below the sustaining voltage where recombination dominates ionization. Therefore, the oscillating voltage waveform prevents localized electron density avalanche and subsequent arcing while the current source drive prevents instabilities which are of large spatial scale. By enhancing discharge stability, the pulse duration and laser energy extracted per liter can be increased and the weight and volume of the laser head and the flow loop can be decreased by factors of 4 to 5.

SCIENCE RESEARCH LABORATORY

CHAPTER 2

TECHNICAL OBJECTIVES OF PHASE I

Science Research Laboratory has successfully met all the objectives of Phase I. The primary objective of this phase was to develop a two dimensional discharge model. This model which will be discussed later in the report predicts stable operation for pulse lengths as long as 100 μs. The second objective of the Phase I effort was to develop a conceptual design for a repetitively pulsed CO_2 laser experiment. SRL has completed the design of a laser head and pulse power system that is capable of operating up to a pulse repetition rate of 50 Hz. The details of this design is also presented in this report. The SRL two-dimensional model has, of course, been used to model the discharge in the laser head design.

During Phase I of the proposed program, a comprehensive, interactive model for the new CO_2 laser discharge concept was developed and used to determine regions of stable discharge operation and efficient CO_2 laser performance. In the model it was assumed that x-ray or UV preionization provides a spatially-uniform electron density of approximately 10^6 - 10^8 electrons/cm^3 which is then increased to approximately 10^{12} electrons/cm^3 in 200 - 300 nsec by avalanching during the front end of the main discharge pulse. The main discharge pulse maintains the electron density at approximately 10^{12} electrons/cm^3 at discharge electric fields (and therefore electron temperatures) which efficiently pump the CO_2 laser mixture. The discharge voltage is assumed to be sinusoidal at a given frequency.

The period of oscillation is chosen to be short compared to the CO_2 laser transition lifetimes and the time scale on which ionization instabilities develop. On these grounds, it is estimated that the oscillation frequency should be between 10 and 10^2 megahertz. The upper limit on oscillation frequency is constrained by the requirement that the discharge skin depth be greater than the transverse dimension of the discharge. These conditions ensure a continuous, near constant laser output during the pulse as well as instability suppression. An analysis which treats volumetric (large scale) discharge stability will be presented in

the following chapters. The remainder of this chapter discusses the consideration that goes into choosing the RF frequency.

RF modulation of the discharge pulse will have an impact on discharge and laser parameters such as electron density, temperature and small signal gain. These effects will be discussed briefly below.

The electron, n_e, production and loss rate is given by

$$\frac{dn_e}{dt} = S + \nu_i n_e - \alpha n_e^2 - \beta n_e \qquad (2.1)$$

where ν_i is the electron impact ionization rate, α is the electron ion recombination-rate and β is the attachment rate. For a self sustained discharge the source function, S=0. Typically, CO_2 laser discharges are recombination dominated. Because of the RF modulation, the discharge electric field will vary in time. The electron temperature and recombination rate will also vary. As the electric field decreases, the average electron energy decreases and recombination rate increases which will have a stabilizing effect and allow slightly constricted regions in the discharge to recover to the ambient electron density.

It is desirable to keep the electron density constant in time. From Eq. (2.1) it is clear that for $\beta << \alpha n_e$, the electron density will be constant if f $>> \alpha n_e$. Typically, $n_e \sim 10^{12}$ cm^{-3} and $\alpha \sim 10^{-6}$ cm^3/sec. So if f $>>$ 1 MHz, n_e will be essentially constant.

The RF electric field can also lead to variations in the average electron energy. Reductions in the electron temperature during minima in the applied RF modulation to the main discharge pulse allow localized regions of increased electron density to relax during the RF pulse to insure discharge stability. The electron temperature will vary appropriately if the RF modulation frequency is $f << k_e N_a$ where k_e is the electron impact excitation rate of ground state of N_2 and N_a is the N_2 density. Typically $k_e \simeq 5 \times 10^{-9} cm^3$/sec and $N_a \simeq 5 \times 10^{18}$cm^{-3} and therefore f $< 2 \times 10^{10}$ Hz. Since the RF modulation frequency will certainly be lower than 10^{10} Hz, the average electron energy will follow the modulation frequency in time and therefore discharge stability will be enhanced.

2-2

For the small signal gain to be constant, $f \gg k_e N_c$, where k_e ($\sim 10^{-11}$ cm^3/sec)[1] is the vibrational transfer rate from N_2 to CO_2 and $N_c \simeq 10^{18}$ cm^{-3} is the CO_2 number density. So for a constant small signal gain, f must be greater than 10 MHz. The streamer stability criterion is consistent with this modulation frequency so the small signal gain will be constant which is important for maintaining high laser power extraction efficiency.

For efficient coupling of power into the laser discharge it is important that the impedance of the discharge be roughly constant during the RF modulation period. The power reflection R from a load having an impedance Z_L is given by $R = \left(1 - Z_o/Z_L\right)^2/\left(1 + Z_o/Z_L\right)^2$ where Z_o is the impedance of the RF power supply and $Z_L \propto E/en_e v_D$ where E is the applied electric field. From a Boltzmann code analysis of typical CO_2 laser mixtures the drift velocity, v_D varies approximately as $(E)^{1/2}$. From Eq. (2.1), $n_e \simeq \nu_i/\alpha$. ν_i is a very strong function of the electric field while α decreases with increasing electric field. So n_e could vary quite strongly with the electric field, i.e, $n_e \sim E^7$. Such a strong variation could result in power reflection from the discharge and the overall efficiency of the discharge could be adversely effected. It is in part for this reason that the RF frequency be chosen such that the electron density is constant, i.e. $f \gg \alpha n_e \simeq 10^6$ Hz.

Finally the cross sectional area of the discharge will be constrained by the skin depth of the RF portion of the discharge current. For a given RF frequency the cross sectional dimensions, h, must be smaller than a skin depth if the current through the cross section is to be uniform. This unequality is given by

$$\ell \leq \left(\frac{1}{\pi f \nu \sigma}\right)^{1/2} \tag{2.2}$$

where σ, the conductivity of CO_2 laser discharges, is typically 2-3 $\times$ 10^{-2} mhos/M. This constraint has been discussed quantitatively in conjunction with the development of the criterion for streamer suppression.

From the preceding discussions, a scaling map for CO_2 can be drawn as shown in Fig. 2.1. This figure is a plot of RF frequency vs cross sectional area of the discharge. As

discussed earlier the RF frequency should be larger than 30 MHz for the small signal gain and electron density to be constant. On the high end. the frequency is constrained by the skin effect. Also shown in Fig. 2.1 is the expected 10.6 μ laser energy that can be extracted per pulse. From this figure it is clear that this pumping technique can provide enough laser energy for laser radar applications.

CO$_2$ SCALING MAP
FREQUENCY VERSUS CROSS SECTIONAL AREA
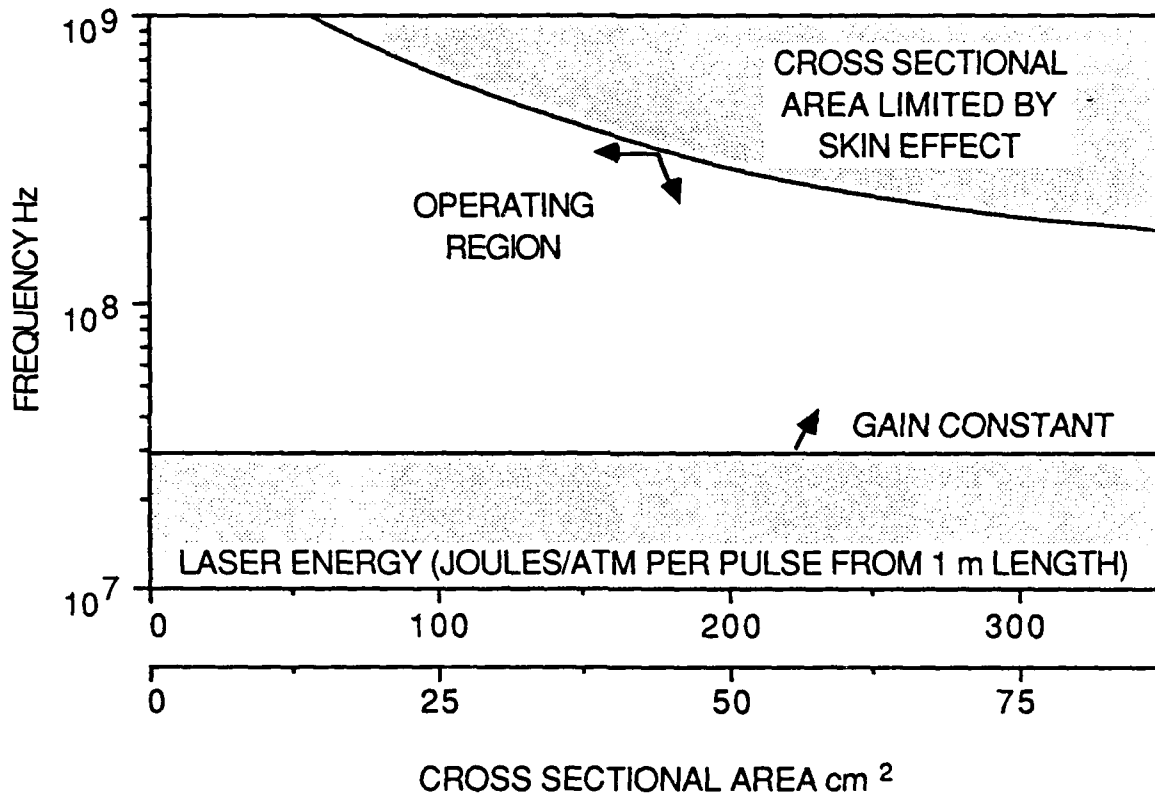
Figure 2.1: Clearly operation at modulation frequencies as high as possible
consistent with the discharge skin depth constraint is optimum
for early suppression.

SCIENCE RESEARCH LABORATORY

CHAPTER 3

REVIEW OF THE ONE DIMENSIONAL DC VOLUMETRIC DISCHARGE STABILITY

3.1   INTRODUCTION

The stability of high pressure discharges has been a subject of major concerns in the high power laser community over the last fifteen years. Most of the discharge stability research, especially for CO_2 laser discharges concentrated on thermal instabilities[1] and their effect on the constriction and arcing of the discharge.[2] Vibrational stabilization methods have been proposed to suppress these instabilities.[3]

The thermal instabilities, by their nature, can only develop on the acoustic (millisecond) time scales. However, in many cases[4] the arcing occurs on a much faster (microsecond and submicrosecond) scale. The phenomenon is characteristic of systems where the electron loss by attachment is present and the two-step electron impact ionization is dominant[4]. Such a model successfully explained the experimentally observed temporally rapid instability scales in the KRF laser discharges.[4]

In addition to the KRF discharge case, subacoustic arcing time scales have been also observed in the high power CO_2 laser experiments. An example of such arcing is in connection with the gas recirculation in the laser, resulting in the buildup of the attaching oxygen component in the laser gas mixture.[5] These observations could also be explained within the two- step ionization model.[4] Although the details of the kinetics in a high pressure molecular discharge, are complex, the concept of two-step ionization as the dominant ionization source in the discharge, is plausible. The basic reason stems from the fact that the electron temperature in these discharges are relatively low (typically 1-2 electron volts) and very few electrons in the tail of the distribution function can directly ionize the ground state, while the ionization of a variety of available excited and metastable states requires much lower energies and is accessible by the bulk of the electron energy distribution. It is precisely this reason, though speculative in its details, but almost certain in reality, which

makes the further development of the multi-step ionization discharge theory necessary.

3.2 THE STEADY STATE SOLUTION

Consider a system, shown schematically in Fig. 3.1 with a DC voltage source V_o. The voltage is distributed between the external resistor R and the plasma, so that

$$V_o = RI + LE \tag{3.1}$$

where I is the discharge current, L is the plasma length and E is the electric field in the plasma, which is assumed to be uniform at all times. In writing Eq.(3.1) it is assumed that the cathode fall voltage is negligible compared to LE (a situation typical of *high pressure* discharges).

Three regimes of operation will be investigated:

A. **Stiff Voltage Case** - Here $R \simeq 0$ and thus the field in the discharge

$$E = \frac{V_0}{L} = \text{Const} \tag{3.2}$$

is not affected by a possible time variation of discharge characteristics, such as the electron density, temperature etc.

B. **Stiff Current Case** - In this case $R \to \infty$ and $V_o \to \infty$, so that the current

$$I \simeq \frac{V_0}{R} = \text{const} \tag{3.3}$$

is time independent and fully described by the external circuit.

C. **Finite External Impedance Case** - In this intermediate case $(0 < R < \infty)$ both the current

$$I(t) = \frac{V_0 - LE(t)}{R} \tag{3.4}$$

and the electric field $E(t)$ depend on the details of the time evolution of the discharge.

At this point it will be informative to discuss the kinetics of the self- sustained discharge. The densities of various species in the discharge will be assumed to be spatially
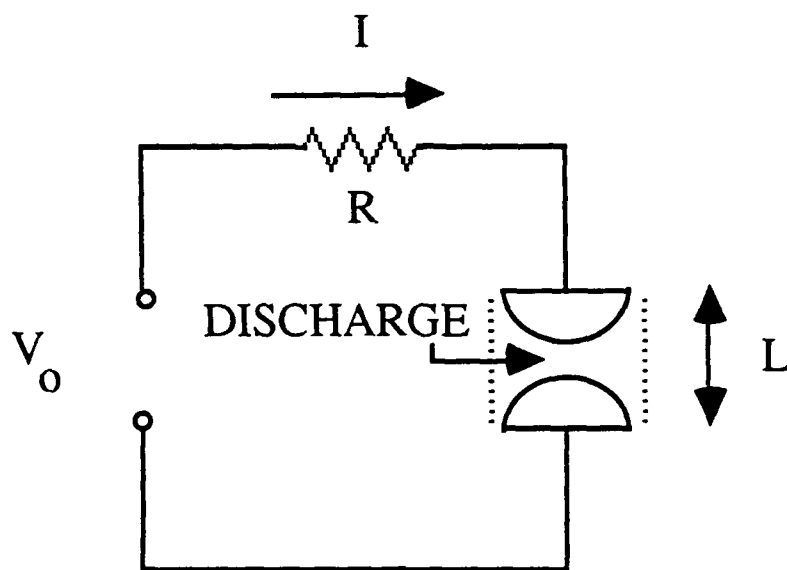
Figure 3.1: General circuit model.

uniform, and the discharge is described by the following system of rate equations ·

$$\frac{dn_e}{dt} = \nu n_m n_e - \alpha n_e^2 - \beta n_e \tag{3.5}$$

$$\frac{dn_m}{dt} = \gamma n_e n_a - \frac{n_m}{\tau} \tag{3.6}$$

Here n_e is the electron density, governed by the ionization of an excited or metastable state having a density n_m and by recombination and attachment losses (ν, α and β are the corresponding rate constants). The density of the excited or metastable state is defined by the balance between the processes of the excitation by electron impact of atoms from the ground state (of density n_a) and the collisional quenching by the neutral gas (with characteristic time constant τ). The time scales $\tau, (\alpha n_e)$ and β^{-1} are assumed to be much shorter than the acoustic times and thus the neutral gas temperature and density are constants.

Equations (3.5) and (3.6) yield the steady state in which all the discharge characteristics are constant and

$$n_m = n_{mo} = \gamma_o \tau n_{eo} n_a \tag{3.7}$$

$$n_e = n_{eo} = \frac{\beta_o}{(\nu_o \gamma_o \tau n_a - \alpha_o)} \tag{3.8}$$

The question of whether this steady state can be reached for a given set of parameters of the external circuit (V_o, R and L) will be considered next. The answer to this question depends on the regime of operation:

A. **Stiff Voltage Case** - Here $E = E_o$ is given, which defines all the rates in Eq. (3.8) so that n_{eo} is known. This, in turn, defines the current density $j = en_{eo}v_{do}$ in the plasma (v_{do} being the drift velocity of the electrons). Thus the steady state exists, provided of course (see Eq. (3.8)) the quantity

$$Q(E_o) \cong \nu_o \gamma_o \tau n_a - \alpha_o \tag{3.9}$$

is *positive*. This condition restricts the accessibility of the steady state and needs a further discussion. Consider the dependence of Q on E_o. Typically, the excitation and ionization rates (γ_o, ν_o) are increasing functions of the electric field,

SCIENCE RESEARCH LABORATORY

while the attachment rate α_o normally decreases with E_o. Furthermore, $\lim_{E_o \to 0} Q \simeq -\alpha_{(E_o \to 0)} < 0$ and with the increase of E_o, $Q \to \nu_o \gamma_o \tau n_a > 0$. Therefore there exists a *single* value of the electric field $E_o = E^*$ at which $Q(E^*) = 0$. The steady state operation of the discharge under the stiff voltage conditions (E_o is given) is thus only possible when

$$E_0 \simeq \frac{V_0}{L} > E^* \qquad (3.10)$$

B. Stiff Current Case - Here the current I_o is defined by the external circuit. On the other hand from Eq. (3.8)

$$I_o = ev_{do} n_{eo} S = \frac{ev_{do} \beta_o S}{Q(E_o)} \equiv F(E_o) \qquad (3.11)$$

where S is the cross section area of the discharge. Equation (3.11) now defines the steady state electric field value E_o. A graphical illustration of the solution of this equation is given in Fig. 3.2, where the qualitative dependence of function F on E is shown based on our earlier discussion of function $Q(E)$. A possible minimum of F at $E = E_m$ is also shown. Such a minimum may exist at high values of E_o at which the ionization and excitation rates grow slower than the drift velocity v_d as the electric field increases. It can be seen in Fig. 3.2 that the steady state exists for any current I_o, provided it is larger than I_m. It is noteworthy that the operation near E_o^* requires rather high currents.

C. Finite Impedance Case - In this intermediate case Eq.(3.11) is replaced by (see Eq. (3.4) for the current)

$$\frac{V_o - LE_o}{R} = F(E_o) \qquad (3.12)$$

The graphical solution of this equation for E_o is shown in Fig. 3.3. One observes that for given values of V_o there exists a critical impedance R_{cr} such that when $R < R_{cr}$ two steady state solutions (E_{o1} and E_{o2}) exist for the electric field, while for $R > R_{cr}$ no steady state exists at all. For $R = R_{cr}$ there is a single steady state.
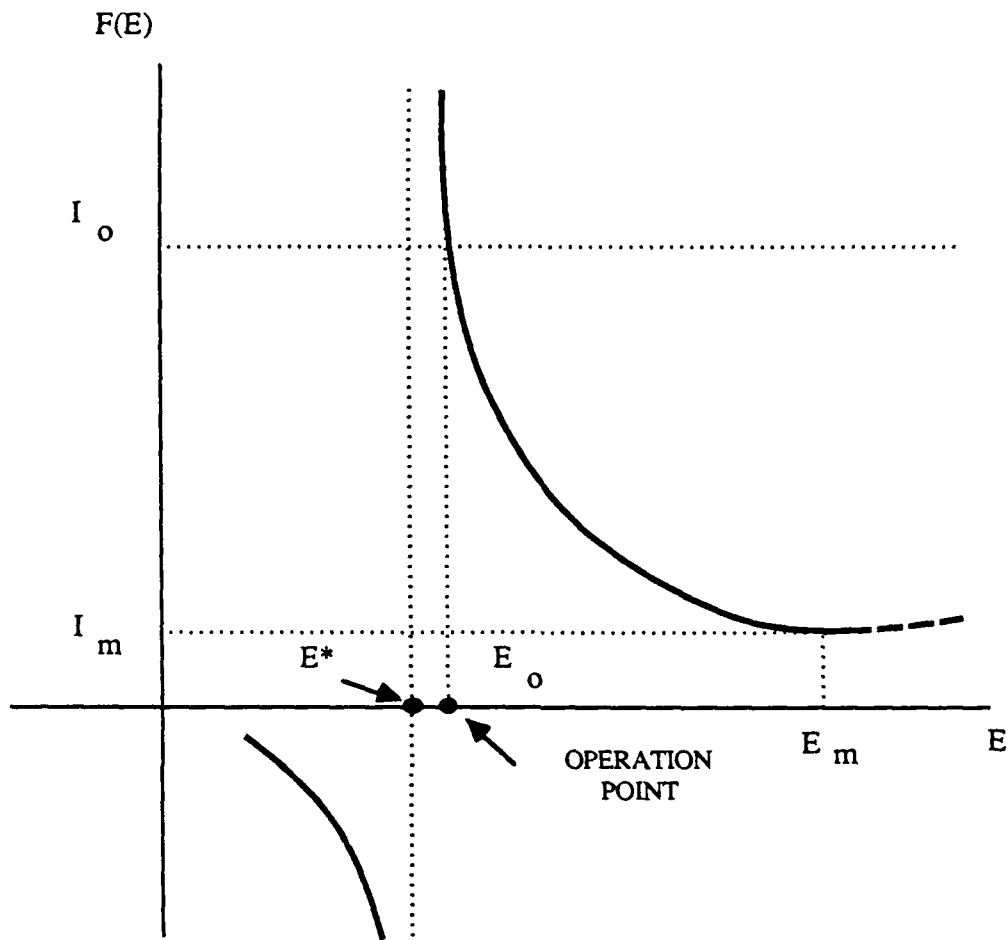
Figure 3.2: Graphical solution for the electric field in the discharge under stiff current condition (I_0 is given).
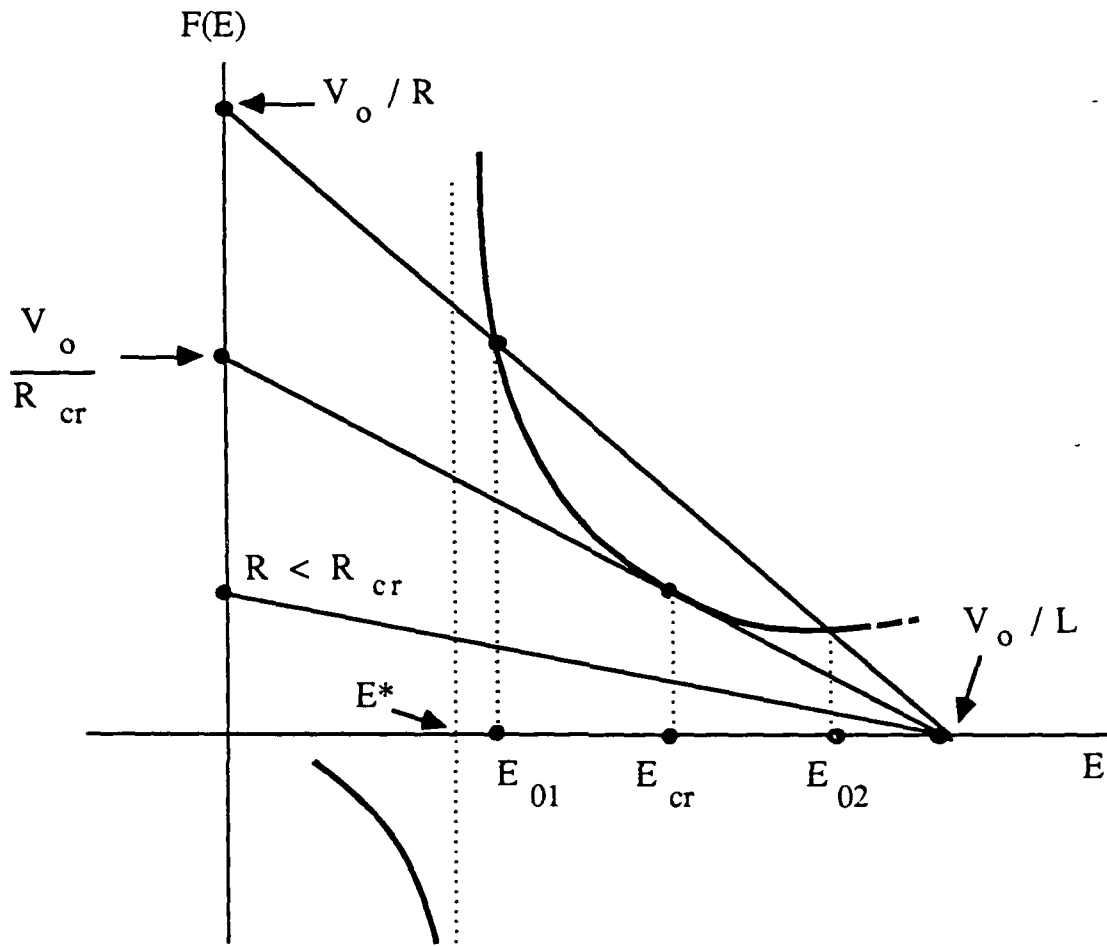
Figure 3.3: Graphical solution for the electric field E_0 in the discharge under finite impedance conditions. The straight lines describe the function $(V_0 - LE_0)/R$ for different values of the external impedance R.

The value of R_{cr} can be found from

$$L = -R_{cr}F'(E_{cr}) \qquad (3.13)$$

where $F' = dF/dE_o$ and E_{cr} is given implicitly by

$$E_{cr} - \frac{V_o}{L} = \frac{F(E_{cr})}{F'(E_{cr})} \qquad (3.14)$$

This completes the analysis of the possiblity of a steady state solution at various external circuit conditions.

3.3 VOLUMETRIC STABILITY ANALYSIS

At this stage one can analyse the problem of the stability of the steady state discharge with respect to a small *uniform* (volumetric) perturbations of the electron and excited state densities. Accordingly, one looks for solutions of Eqs. (3.5) and (3.6) in the form

$$n_e(t) = n_{eo} + \delta n_e(t) \,; \; n_m(t) = n_{mo} + \delta n_m(t) \qquad (3.1)$$

where n_{eo} and n_{mo} are the steady state solutions described in the previous section and $\delta n_e, \delta n_m$ are small perturbations. Again consider *the stiff voltage, stiff current* and finite impedance cases will be considered separately.

A. **Stiff Voltage Case** - Since the electric field in the discharge in this case is a constant of time (E_o) all the rates in Eqs. (3.5) and (3.6) are also constants of time and, after the linearization, one can write

$$\frac{d(\delta n_e)}{dt} = \nu n_{eo}\delta n_m + (\nu n_{mo} - 2\alpha n_{eo} - \beta)\delta n_e \qquad (3.2)$$

$$\frac{d(\delta n_m)}{dt} = \gamma n_a\delta n_e - \frac{\delta n_m}{\tau} \qquad (3.3)$$

Assuming solutions $\delta n_m, \delta n_e \sim \exp(-i\omega t)$, one then obtains the characteristic equation

$$\omega^2 + i\omega(\alpha n_{eo} + \frac{1}{\tau}) + \frac{\beta}{\tau} = 0 \qquad (3.4)$$

The roots of Eq. (3.4) are

$$\omega_{1,2} = -\frac{i}{2}\left[\left(\alpha n_{eo} + \frac{1}{\tau} \right) \pm \sqrt{\left(\alpha n_{eo} + \frac{1}{\tau} \right)^2 + \frac{4\beta}{\tau}} \right] \qquad (3.5)$$

3-8

and, since one of these roots has $Im\omega > 0$, the solution of Eqs. (3.2) and (3.3) is generally unstable [except when $\beta = 0$, in which case one of the roots, $\omega_2 = 0$, indicates a marginal stability]. It can be also seen that if τ is the shortest characteristic time in the problem, Eq. (3.5) yields $\omega_2 \simeq i\beta$, i.e., the growth rate is approximately the rate of attachment.

B. **Stiff Current Case** - Here, the current $I = ev_d n_e S$ in the discharge remains constant in time, regardless the variation in the electron density. Therefore,

$$\delta v_d n_{eo} + \delta n_e v_{do} = 0$$

and, since

$$\delta v_d = \frac{dv_{do}}{dE_o}\delta E \quad ,$$

the electron density perturbation results in the perturbation of the electric field, given by

$$\delta E = -\frac{v_{do}\delta n_e}{v'_{do}n_{eo}} \tag{3.6}$$

where $v'_{do} = dv_{do}/dE_o$. Typically $v'_{do} > 0$ and thus the variation of the electron density leads to the *opposite* change in the electric field E_o in the discharge. This, of course, plays a stabilizing role via the appropriate change in the electron production rate. The phenomenon can be demonstrated analytically. Indeed, in the case of interest, perturbed Eqs. (3.2) and (3.3) should now be replaced by

$$\frac{d(\delta n_e)}{dt} = \nu_o n_{eo}\delta n_m + (\nu_o n_{mo} - 2\alpha_o n_{eo} - \beta_o)\delta n_e$$
$$+ (\nu'_o n_{mo}n_{eo} - \alpha'_o n_{eo}^2 - \beta'_o n_{eo})\delta E \tag{3.7}$$

$$\frac{d(\delta n_m)}{dt} = \gamma_o n_a \delta n_e - \frac{\delta n_m}{\tau} + \gamma'_o n_a n_{eo}\delta E \tag{3.8}$$

where $\xi' = d\xi/dE_o$ for $\xi = \nu_o, \alpha_o, \beta_o$ and γ_o. The substitution of expression for δE transforms Eqs. (3.7) and (3.8) into a system of linear first order differential equations for δn_e and δn_m. The characteristic equation for this system is

$$\omega^2 + i\omega A + \frac{\beta}{\tau} - B = 0 \tag{3.9}$$

3-9

where

$$A = \alpha n_{eo} + \frac{1}{\tau} + \frac{v_{do}}{v'_{do}}(n_{mo}\nu'_o - n_{eo}\alpha'_o - \beta'_o) \tag{3.10}$$

and

$$B = \frac{v_{do}}{v'_{do}}\left[\alpha_o n_a \nu_o n_{eo}\left(\frac{\nu'_o}{\nu_o} + \frac{\gamma'_o}{\gamma_o}\right) - \frac{\alpha'_o n_{eo} + \beta'_o}{\tau}\right] \tag{3.11}$$

The roots of Eq. (3.9) are

$$\omega_{1,2} = -\frac{i}{2}\left[A \pm \sqrt{A^2 + 4\left(\frac{\beta}{\tau} - B\right)}\right] \tag{3.12}$$

Finally, by inspecting Eqs. (3.5 and (3.11)) one observes that

$$\frac{\beta}{\tau} - B = \frac{Q(E_o)F'(E_o)}{eS\tau v'_{do}} \tag{3.13}$$

and therefore $\beta/\tau - B < 0$, if $F'(E_o) < 0$. In this case Eq. (3.12) yields characteristic roots with $Im\omega < 0$ and thus the discharge is *stable* in the decreasing region of function $F(E_o)$ ($E^* < E_o < E_m$ see Fig. 3.2.).

C. Finite Impedance Case - In this *intermediate* case (see Eq. (3.12))

$$\frac{V_o}{R} = ev_d n_e S + \frac{LE}{R} = \text{const}(t) \tag{3.14}$$

Therefore, instead of (3.6), one has

$$\delta E = -v_{do}\frac{\delta n_e}{(v'_{do} + L/eRSn_{eo})n_{eo}} \tag{3.15}$$

This shows that Eqs. (3.9) through (3.12) also holds in the finite impedance case if, in these equations, one replaces

$$v'_{do} \longrightarrow v'_{deff} \equiv v'_{do} + L/eRSn_{eo} \tag{3.16}$$

As $R \rightarrow \infty$, $v'_{deff} \rightarrow v'_{do}$ and the stiff current discharge is recovered (except for the fact that V_0 is finite) (Case B). If, in contrast, $R \rightarrow 0$ then $\nu'_{deff} \rightarrow \infty$ and $B \rightarrow 0$, which is the unstable case, corresponding to the stiff voltage conditions.

3-10

3.4 NUMERICAL EXAMPLE

In this section the discharge model developed so far will be applied to the specific case of a CO_2 laser discharge. Before this can be done, however, one has to know the relevant rate constants for the CO_2 mixture as a function of the electric field. A one atmosphere total pressure, 3/2/1, $He/N_2/CO_2$ mixture will be chosen as an example. The rate constants for the ionization and excitation of the electronic states of N_2 in this mixture, the fraction of discharge energy that goes into vibrational excitation and the drift velocity as predicted by the Boltzman code[6] are shown in Figs. 3.4 and 3.5. Form Fig. 3.4, which is a plot of T_e, v_d and the efficiency of exciting the vibrational levels of N_2. It is clear that efficient CO_2 laser operation occurs between 5-10 kV/cm.

Figure 3.5 shows the variation of ν and γ (see Eqs. (3.5 and (3.6)) as functions of the electric field. Also shown in Fig. 3.5 is the curve for the ionization rate from the ground state (ν_a). The curve for γ shown in Fig. 3.5 is the total excitation rate constant for all the electronic levels. This was chosen since it is difficult to identify the relevant metastable or electronic state that will be subsequently ionized. It is probable that this state will be a high lying state such as the C state of N_2. The ionization rate constant ν of the excited electronic state has the same shape as the electron impact ionization rate of N_2 (a $\sum_u$),[7] its magnitude, however, was increased by 10^2, since this state is about 9 eV below the ionization level of N_2 as opposed to the C level which is less than 4 eV below the ionization level. From Fig. 3.5 it is clear that $\nu_a << \nu$ in the region of interest and so for any reasonable metastable density ($n_m > 10^{12}$ cm^{-3}) the metastable ionization will be dominant. Fig. 3.6 shows the recombination coefficient as a function of the electric field. Measurements of the recombination coefficient for a 3/2/1 laser mixture has been made for electric field strengths between 2.5 and 5 kV/cm.[6] The curve shown in Fig. 3.6 makes use of these measurements and assumes an almost constant recombination rate for $10 < E < 15$ kV/cm.

SCIENCE RESEARCH LABORATORY
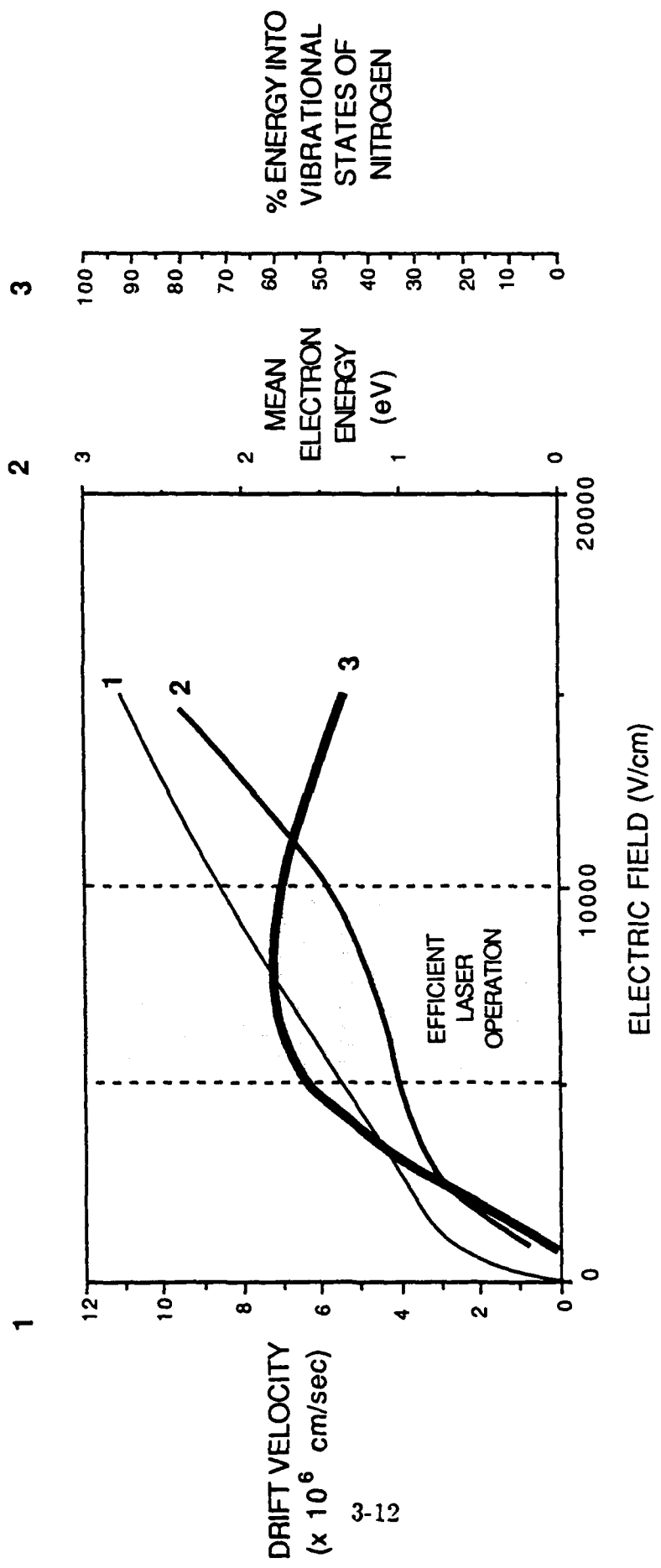
Figure 3.4: The dependence of the electron temperature, drift velocity and the vibrational excitation efficiency on the electric field in a 1 atm pressure 3/2/1 He/N$_2$/CO$_2$ laser discharge.
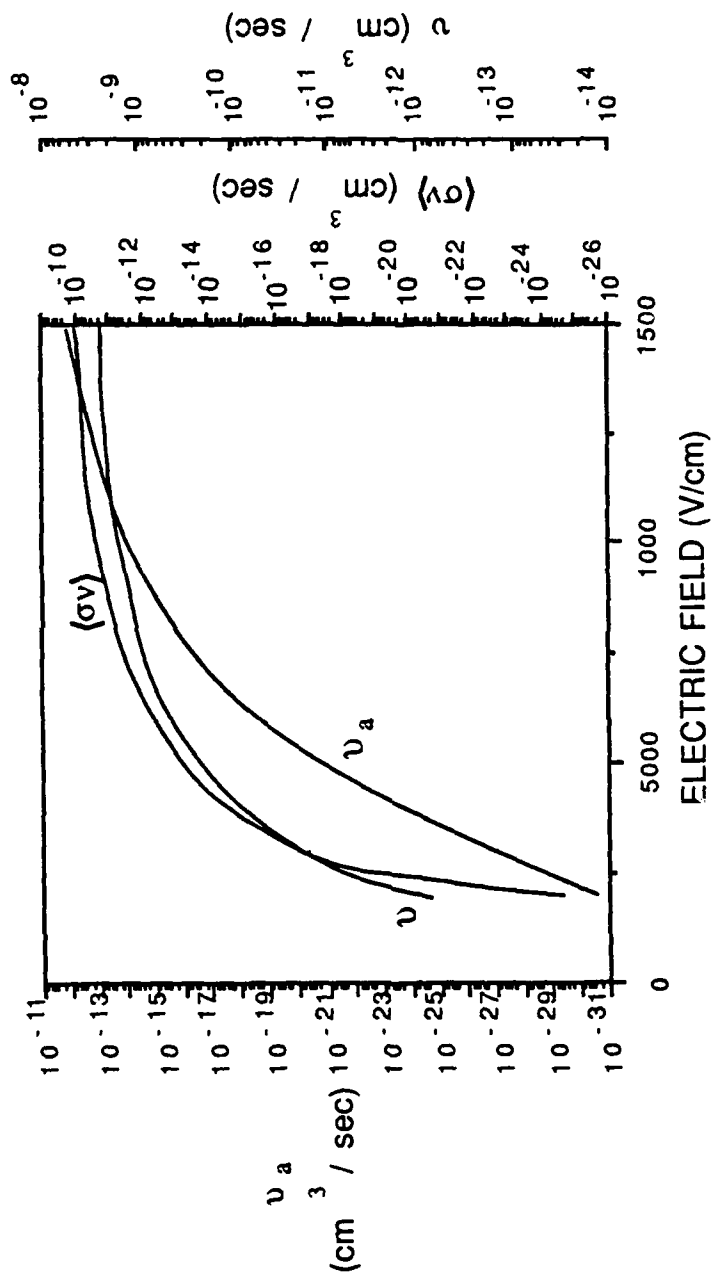
Figure 3.5: The dependence of various excitation rates in a 1 atm 3/2/1, CO_2 laser mixture discharge on the electric field ν_a is the ionization rate from the ground state; ν is the indirect ionization rate; and γ is the total excitation rate from the ground.
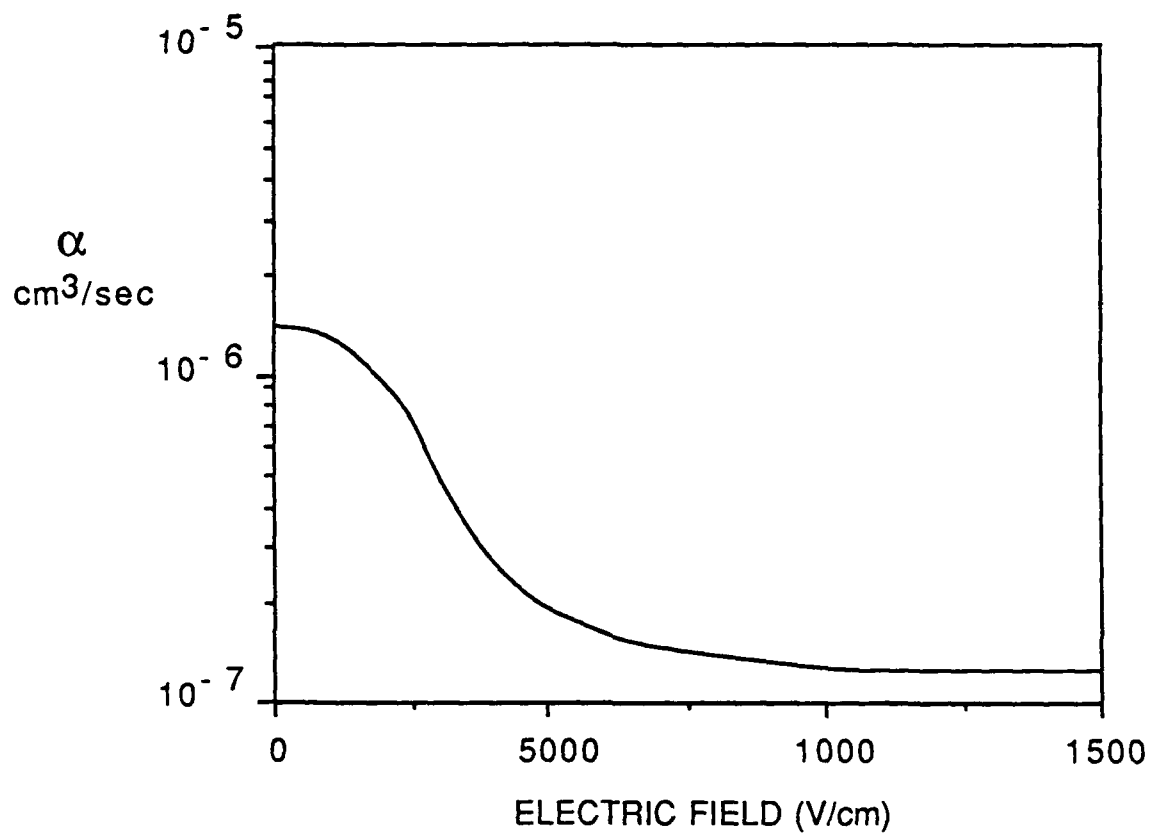
Figure 3.6: The dependence of the recombination rate on the electric field in a 1 atm, 3/2/1 CO_2 laser mixture discharge.

SCIENCE RESEARCH LABORATORY

At this stage the stability of the discharge at various operating conditions will be analysed. The analysis will be started by presenting the dependence of function $F(E)/S$ on the electric field (see Eq. (3.11)). This dependence, is shown in Fig. 3.7 for the case of interest. One observes that $E^* \simeq 8.05$ kV/cm, so that the steady state discharge operation is possible for 8.05 kV/cm $< E <$ 15 kV/cm (see the discussion in Section 2 and Figs. 3.2 and 3.3). The graphical solution for the electric field E_o in the steady state discharge is also shown under the following conditions: $V_o = 9$ kV, $RS = 400$ Ωcm^2, $L = 1$ cm, $\tau = 1$ μsec and $\beta_o = 10^5$ sec^{-1}. The steady state electric field is 8.45 kV/cm which, by using Eq. (3.8), and data in Figs. 3.4 through 3.6, yields the steady state plasma density $n_{eo} = 1.07 \cdot 10^{12}$cm^{-3}. Prior to studying the stability of the discharge at these conditions, the stiff voltage situation is considered. The analysis in Section 3 shows that the discharge is *unstable* in the stiff voltage case for $\beta_o \neq 0$. This unstable behavior is demonstrated in Figs. 3.8 and 3.9, where the numerical solutions of Eqs. (3.5) and (3.6) are shown for E_o = 8.45 kV/cm = Const(t) (stiff voltage condition) and two different initial values for the electron density. The electric field E_o defines various rates in Eqs. (3.5) and (3.6) which remain constants in the calculations, consistent with the stiff voltage conditions. Figure 3.8 shows the case when $n_e(0) = n_m(0) = 5.10^{11}$cm^{-3}. This initial density is lower than the above mentioned steady state density $(n_{eo} = 1.07 \cdot 10^{12}cm^{-3})$. Figure 3.8 shows that the electron density decays in time, in this case, and the discharge is quenched. Figure 3.9, in contrast, shows the case of $n_e(o) = n_m(o) = 2 \cdot 10^{12}$ cm^{-3} which is larger than the steady state electron density n_{eo}. n_e then grows indefinitely in time, verifying the instability. One finds that Figs. 3.8 and 3.9 represent the general time evolution of the discharge in the stiff voltage case, depending on whether $n_e(o)$ is larger or smaller than n_{eo}.

At this point it is appropriate to proceed to the numerical simulation of the finite external impedance discharge case. Again setting $V_o = 9$ kV/cm, $L = 1$ cm, $\tau = 1$ μsec and $\beta = 10^5$ sec^{-1} = Const(t). Nevertheless, in contrast to the stiff voltage case, the rate Eqs. (3.5) and (3.6) have now been solved simultaneously with the circuit Eq. (3.14).

3-15
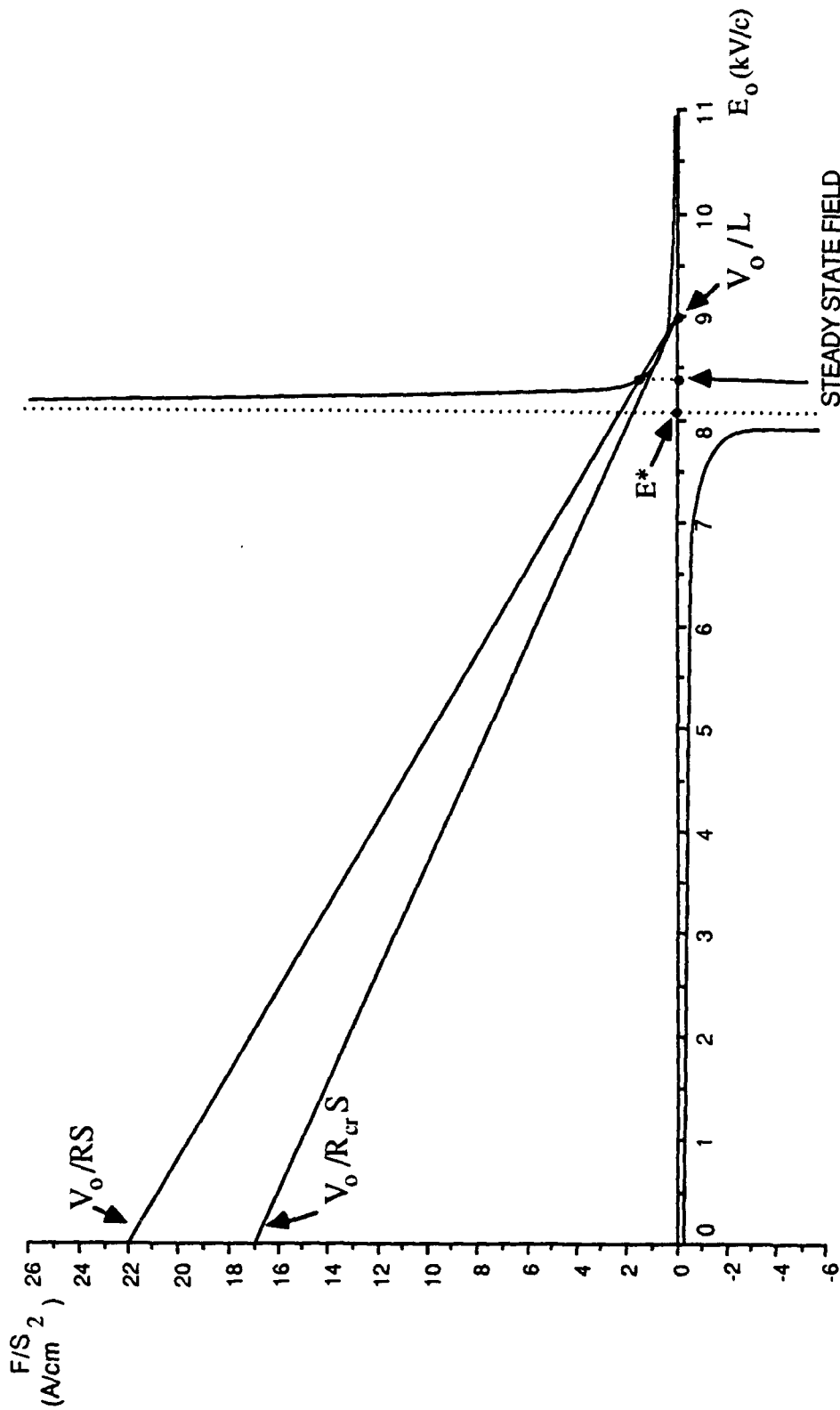
Figure 3.7: The dependence of F/S on the electric field in a 1 atm, CO_2 laser discharge mixture. The operating field ($E_0 = 8.45$ kV/cm found graphically for the case: $V_0 = 9$ kV/cm, RS = 400 Ω cm^2, L = 1 cm, $\tau = 1$ μsec, and $\beta_0 = 10^5$ sec^{-1} The straight line tangent to the curve F/S allows to determine the impedance ($R_\alpha S = 520$ Ω cm^2).
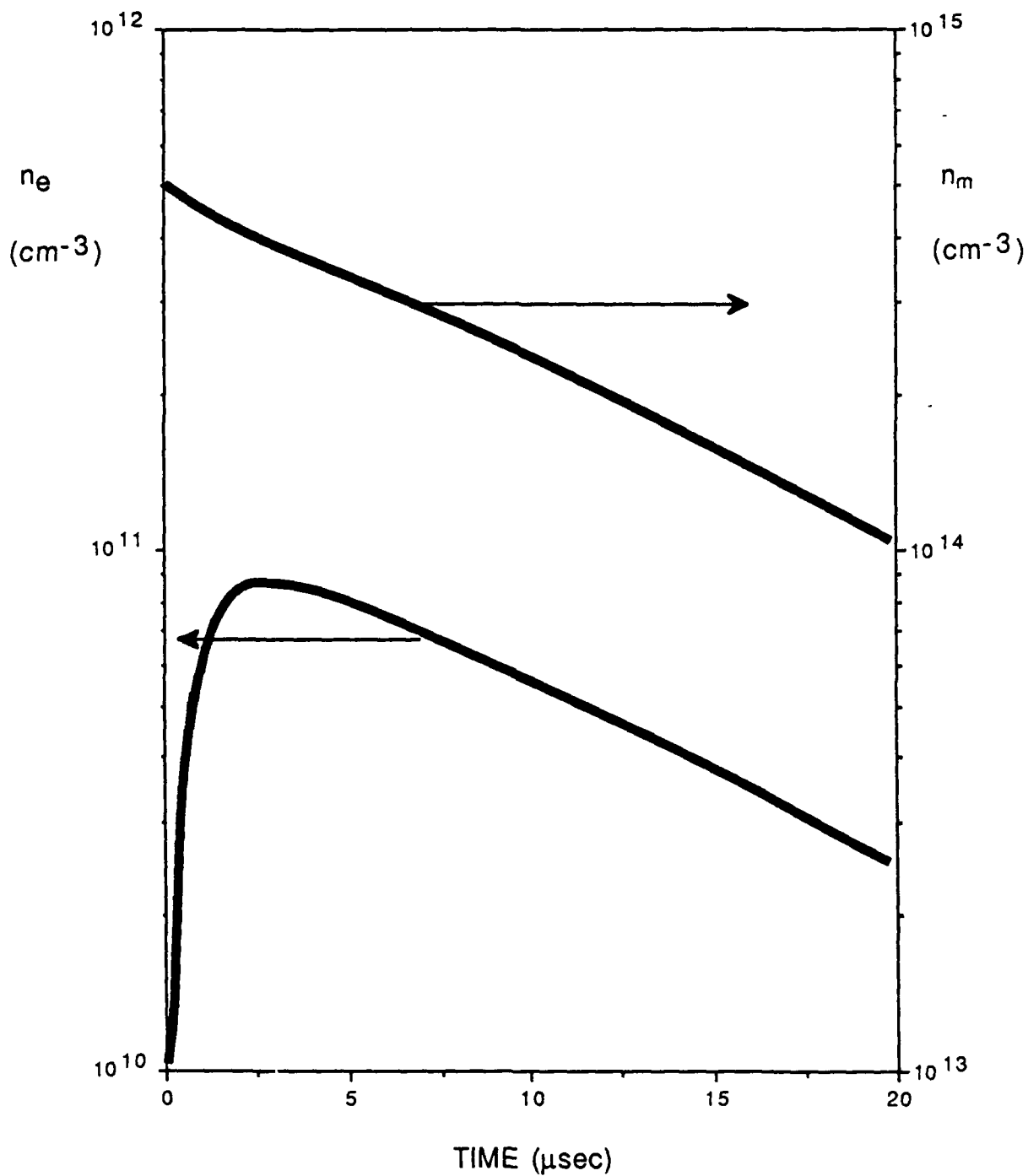
Figure 3.8: The time evolution of the electron and metastable densities in a stiff voltage discharge. The initial electron density ($n_e(0) = 5 \times 10^{11}$ cm^{-3}) is lower than the steady state density ($n_{eo} - 1.07 \times 10^{12}$ cm^{-3}) at the given voltage ($V_0 = 8.45$ kV).

3-17
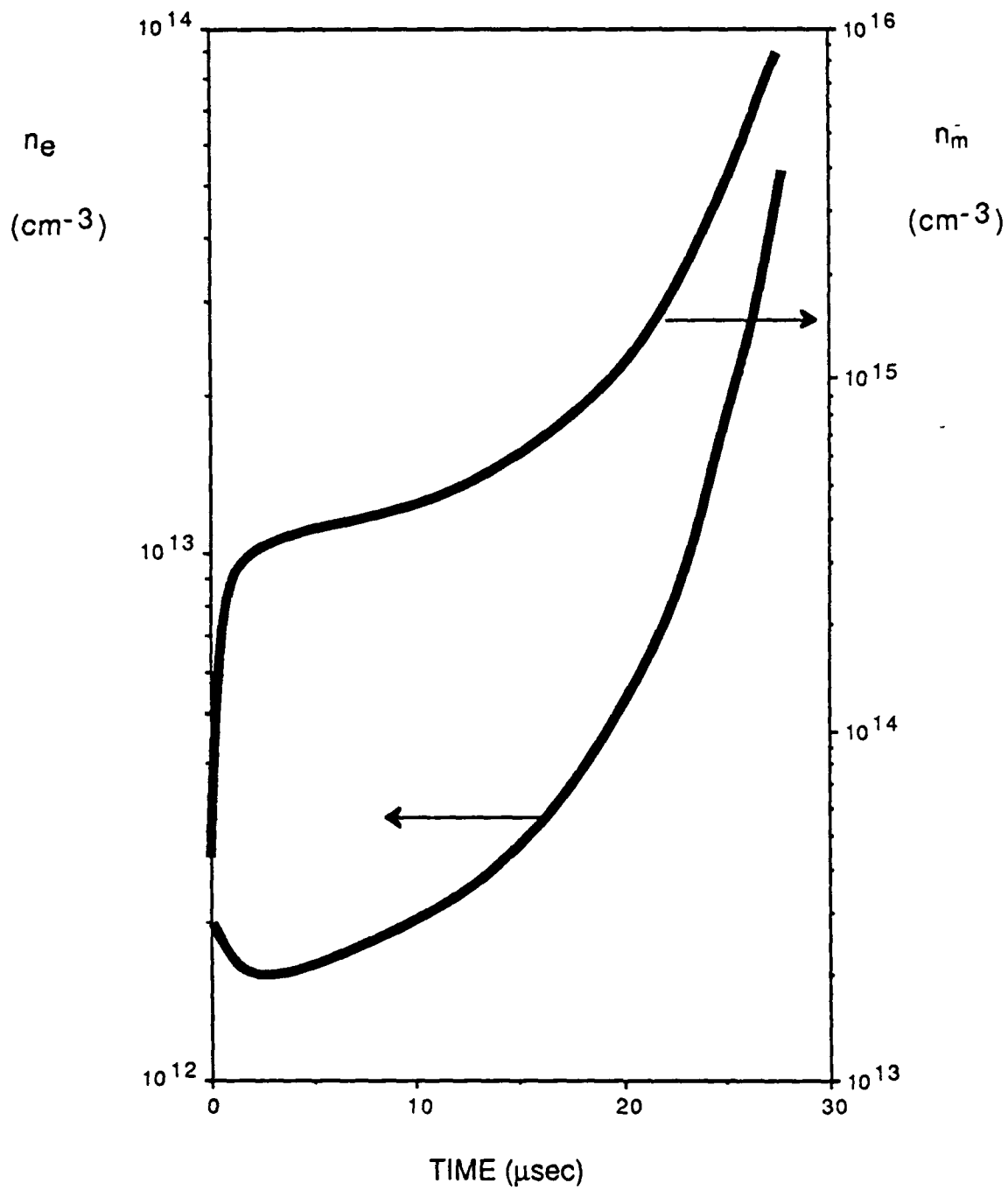
Figure 3.9: The time evolution of the electron and metastable densities in a stiff voltage discharge with attachment. Initial electron density (2×10^{12} cm^{-3}) is higher than the steady state density ($n_{eo} = 1.07 \times 10^{12}$ cm^{-3}) at the given voltage ($V_0 = 8.45$ kV).

3-18

The code also makes use of the dependencies of the rate constants shown in Figs. 3.4-3.6. The predictions of the code are plotted in Figs. 3.10, 3.11 and 3.12. Figure 3.10 shows the temporal variation of n_e and E for the circuit impedance of $RS = 400 \ \Omega cm^2$. The initial electron density was assumed to be $10^{12} cm^{-3}$. One observes that the electron density increases by about 10% to $1.07 \cdot 10^{12} cm^{-3}$ and the electric field decreases from its initial value of 9 kV/cm to 8.45 kV/cm. These are the steady state electron density and the electric field under the above conditions (see the graphical solution in Fig. 3.7). Figure 3.11 shows the effect of lowering the external impedance to $RS = 1 \ \Omega \ cm^2$. Under these conditions, as can be seen in the figure, the discharge has stiff voltage characteristics during the first $\sim 10 \ \mu sec$ of the discharge. It is unstable as predicted by the analysis and the electron density suddenly increases by almost three orders of magnitude after 10 μsec. The discharge becomes stable at this large value of $n_e \sim 8.10^{14} cm^{-3}$. However, in practice, any initial spatial nonuniformities in n_e amplified in time by the instability could result in streamer formation during the fast transition period. We shall consider the details of such **spatial** inst abilities in the next chapter of this report. Finally, Fig. 3.12 illustrates a typically situation in a discharge with an above-critical external impedance ($R > R_{cr}$, see the discussion in the previous section). In the case considered (see Fig. 3.7) $R_{cr} \simeq 520$ Ωcm^2, while the results presented in Fig. 3.12 correspond to the case $R = 800 \ \Omega cm^2$. No steady state exists in this case, as predicted by the theory, and one observes in Fig. 3.12 that the discharge is quenched.

3.5 CONCLUSIONS

(i) We have considered the volumetric stability dynamics of discharges dominated by **two step ionization**. In the presence of an attacher these discharges are shown to be potentially unstable on much shorter time scales than those characteristic of conventional thermal instabilities.

(ii) The theoretical modeling of the discharge included the discharge kinetics coupled to the **external electric circuit** and its response to varying current conditions. A
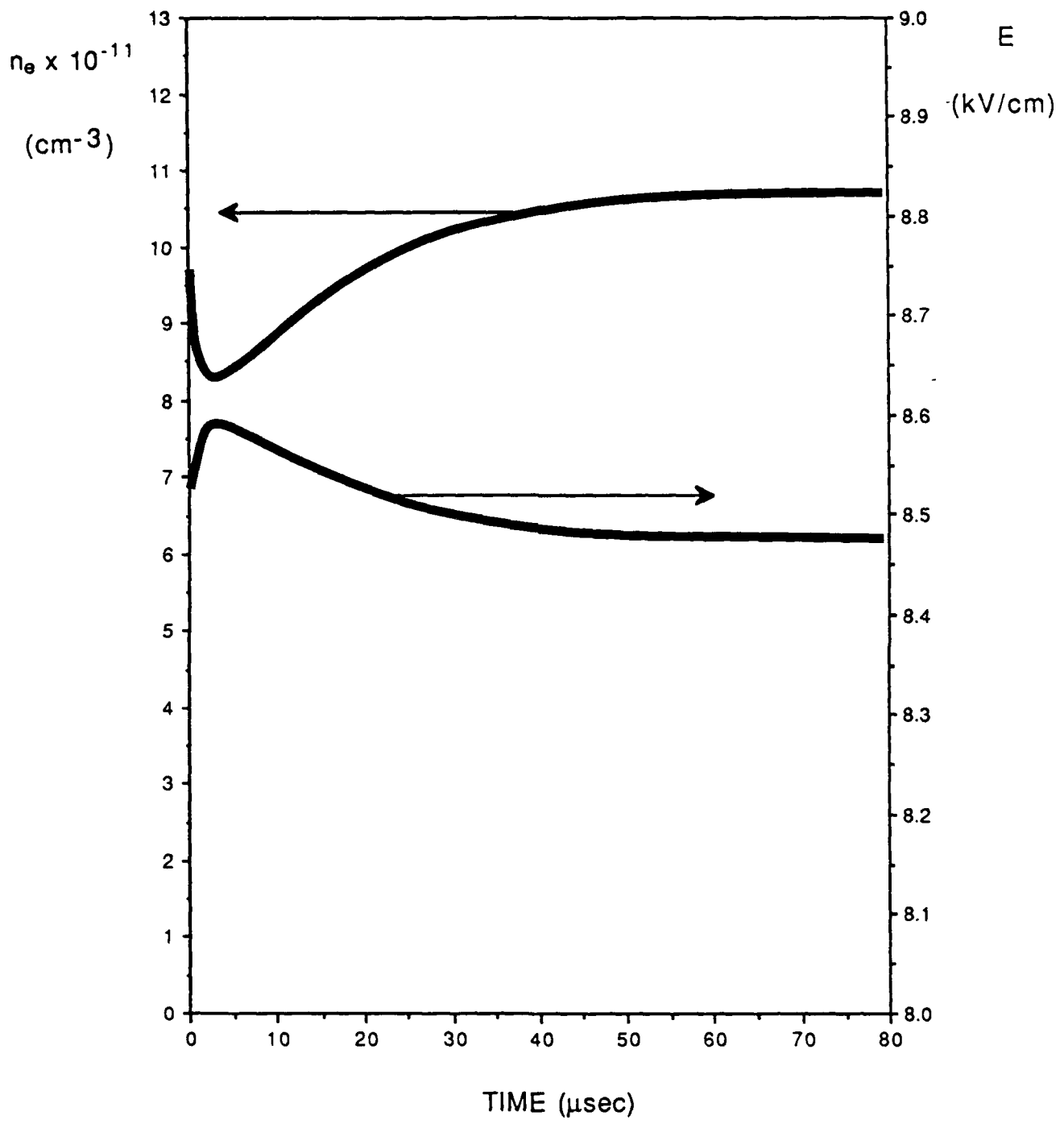
Figure 3.10: Curves of n_e and E for a volumetrically stable discharge. The parameters are: $n_e(0) = 10^{12} \, cm^{-3}$, $V_0 = 9 \, kV/cm$, $RS = 400 \, \Omega \, cm^2$, $l = 1 \, cm$, $\tau = 1 \, \mu sec$, $\beta = 10^5 \, sec^{-1}$.

3-20
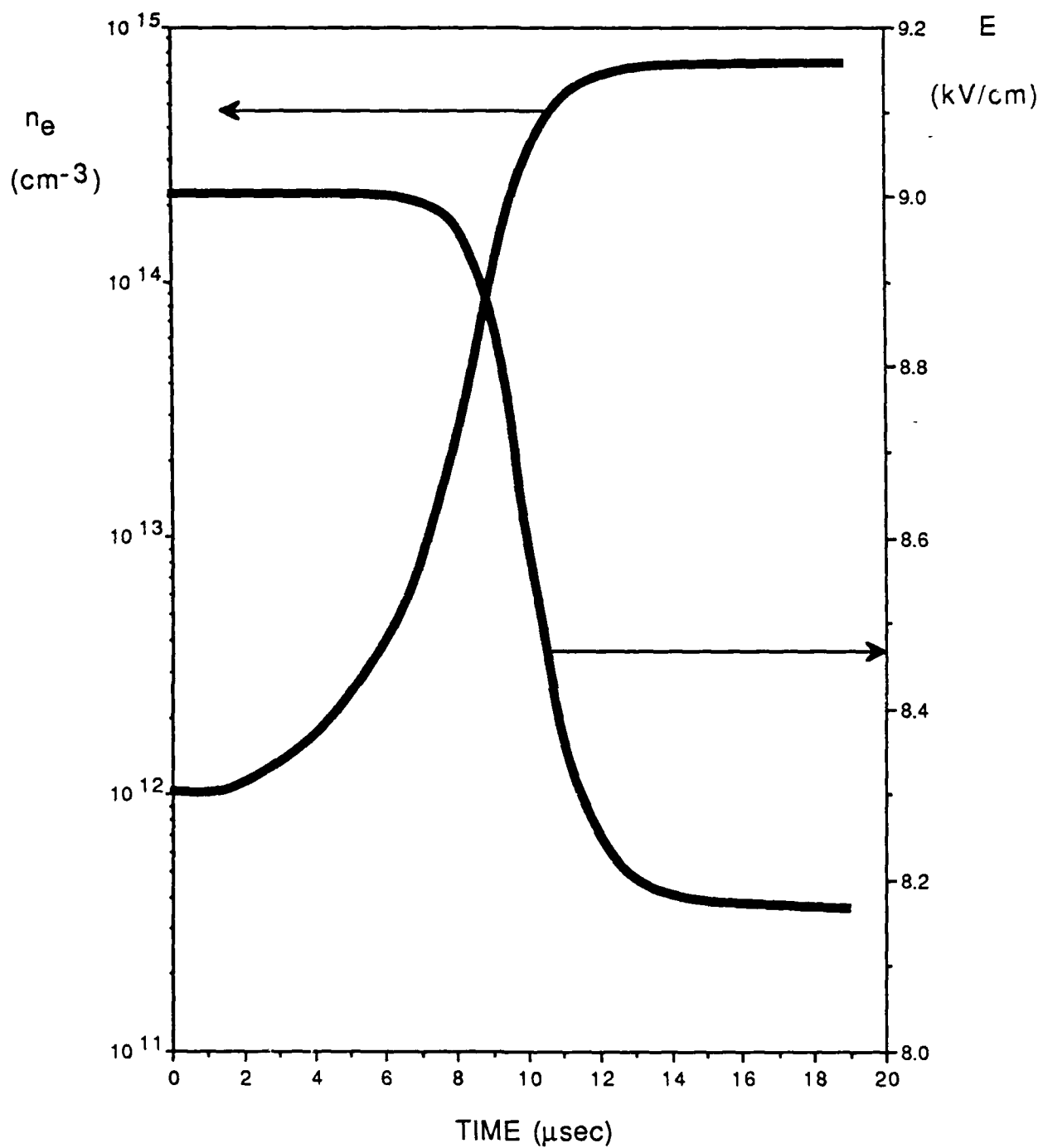
Figure 3.11: Curves of n_e, and E for a low external impedance discharge ($RS = 1$ W cm^2). The parameters are $n_e(0) = 10^{12}$ cm^{-3}, $V_0 = 9$ kV/cm, L = 1cm, t = 1msec and b = 10^5 sec^{-1}. The discharge is unstable during the initial evolution phase (t < 15 msec).

SCIENCE RESEARCH LABORATORY
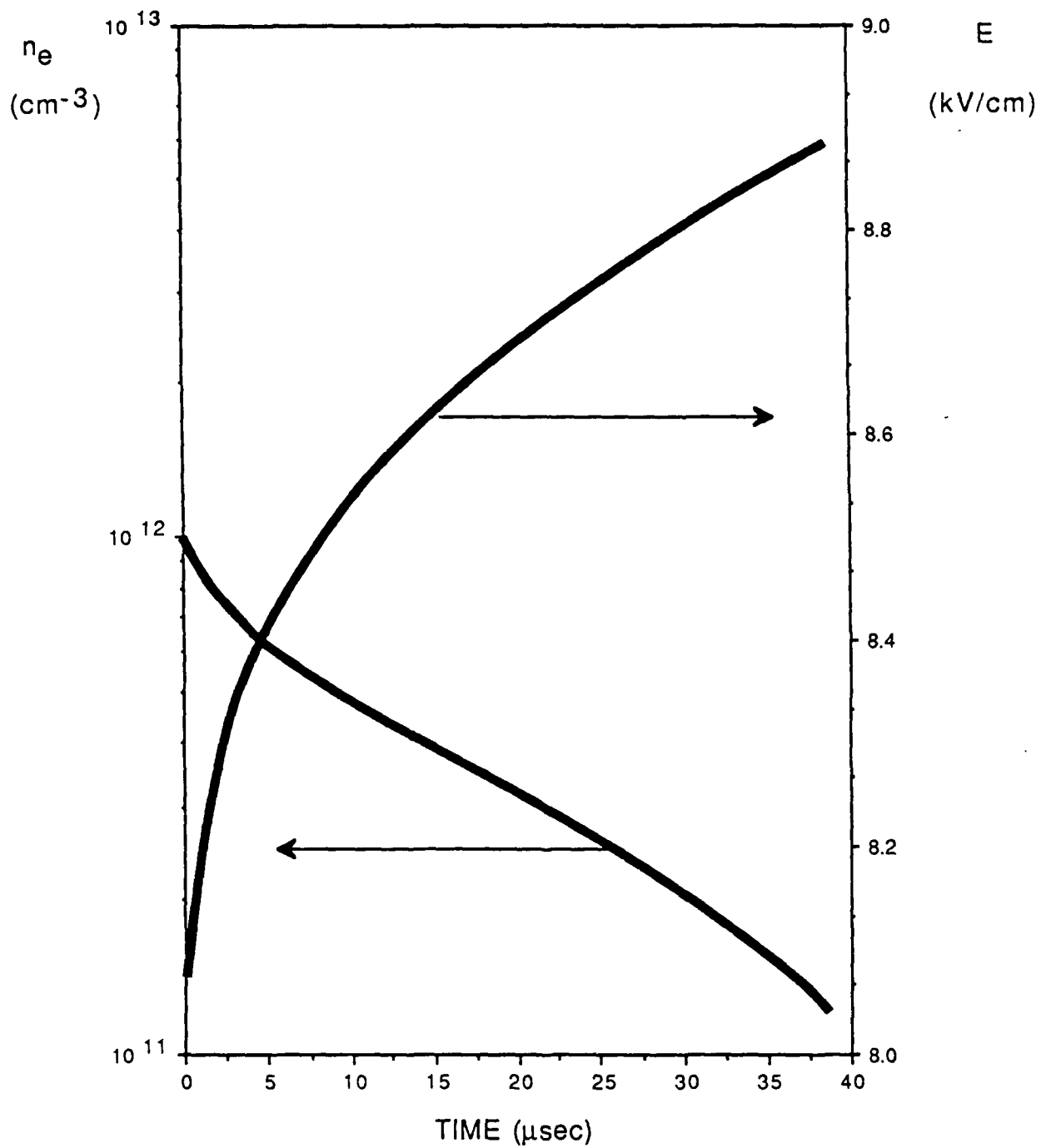
Figure 3.12: The curves of n_e and E for a discharge with an above- critical impedance
(RS = 800 Ω cm^2). All other parameters are the same as in Figs. 3.10 and 3.11. No steady
state exists for RS > $R_{cr}S$ = 520 Ω cm^2 and the discharge is quenched.

SCIENCE RESEARCH LABORATORY

number of discharge configurations, such as stiff voltage, stiff current and finite external impedance were considered in searching for a steady state stable regime of operation.

(iii) In the stiff voltage discharge [the electric field in the discharge $E = $ const (t)] the steady state exists for $E > E^*$, where E^* is the value at which the characteristic function $Q(E)$ [see Eq. (3.9)] vanishes. Nevertheless, even if the steady state is reached, the discharge is volumetrically unstable under the stiff voltage condition. Practically, if at t = 0 the initial electron density $n_e(0) > n_{eo}$ (n_{eo} being the steady state density) the current density j increases indefinitely on a finite time scale, while for $n_e(0) < n_{eo}$ the discharge is quenched ($j(+) \rightarrow 0$). The linear instability temporal rate is typically proportional to the attachment rate β (if β is sufficiently small).

(iv) The stiff current discharge [$j = $ const(t)] has a steady state at **all** currents and the discharge is volumetrically stable, provided the characteristic function F(E) [see Eq. (3.11)] is **decreasing** function of the electric field.

(v) In the finite external impedance discharge case we found the existence of a critical impedance value R_{cr} such that there exist two steady state when $0 < R < R_{cr}$ and no steady state is possible when $R > R_{cr}$. Furthermore, only if R_{cr} is large enough, the above mentioned steady state solutions are stable in a part of the interval $[0, R_{cr}]$.

(vi) The theoretical predictions were illustrated in the example of an atmospheric CO_2 laser discharge model. The numerical solutions of the kinetic and external circuit equations, underlying the problem in this case were found in an agreement with the theory.

SCIENCE RESEARCH LABORATORY

CHAPTER 4

RF STABILIZATION OF MOLECULAR DISCHARGES

4.1 INDUCTIVE STABILIZATION OF THE DISCHARGE AGAINST STREAMER FORMATION

In the preceding chapter, the volumetric or bulk stability of the discharge has been analyzed and stable operating regions for the CO_2 laser discharge have been identified. Although a discharge can be volumetrically-stable, micro-instabilities can lead to constriction of the discharge and streamer formation. To stabilize the discharge against streamer formation, SRL proposes to use an RF pulsed power source. Since a streamer is far more inductive than the discharge, its formation and growth will be suppressed because the RF power component will be excluded from the region of a localized instability as it attempts to form. The inductance of the localized instability region is responsible for excluding RF currents (and therefore power) from this region.

The effectiveness of inductive discharge stabilization can be evaluated from an analysis of the equivalent circuit shown in Fig. 4.1. The discharge impedance, which has inductive and resistive components, L_D and R_D, while operating stably, is driven by an oscillating current source. The currents through these components are I_L and I_R respectively. The voltage drop across the inductor and resistor must be equal hence

$$i\omega L I_L = R I_R \tag{4.1}$$

By conservation of current,

$$I_L + I_R = I \tag{4.2}$$

where I is the source current. Equations (4.1) and (4.2) can be solved simultaneously to give

$$I_L = \frac{R(R - i\omega L)}{R^2 + \omega^2 L^2} I \tag{4.3}$$

and

SCIENCE RESEARCH LABORATORY
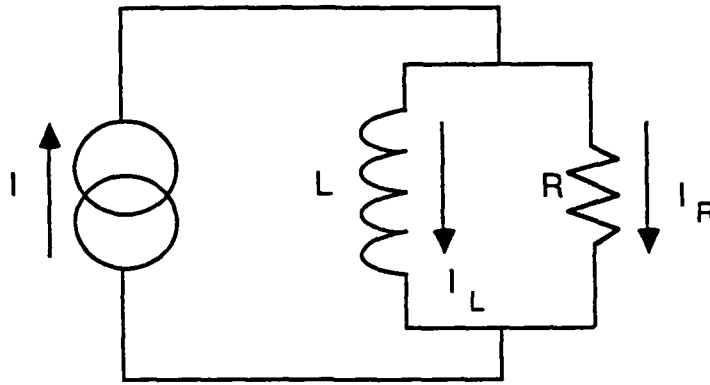
Figure 4.1: Stabilization of discharge by inductance

$$I_R = \frac{\omega^2 L^2 + i\omega RL}{R^2 + \omega^2 L^2} I \qquad (4.4)$$

For efficient discharge pumping the inductive current should be minimized. i.e., $R \ll \omega L$, and $I \simeq I_R$. If the reverse is true, then $I \simeq I_L$ and the transfer of energy to the discharge will be inefficient especially if additional resistive losses are present in the system.

Should the discharge begin to constrict, the inductance will increase and the resistance will decrease. Under these conditions the frequency of RF modulation can be chosen to exclude RF current and power from the constricting region and thereby inhibit arc formation.

From the equations above, it is clear that the RF frequency, f, should be selected such that $R_D/2\pi L_D > f > R_s/2\pi L_S$ where R_s and L_s are the resistance and inductance of the perturbed discharge region. These constraints on the modulation frequency have a simple physical explanation. The constraint, $R_D/2\pi L_D > f$, insures that the skin depth at the modulation frequency is larger than the transverse dimension of the discharge. This constraint leads to spatially uniform discharge pumping of the laser medium. On the other hand, the constraint $R_s/2\pi L_s < f$ insures that the skin depth at the modulation frequency is smaller than the transverse dimension of the discharge constriction. Therefore, oscillating discharge power is prevented from penetrating to the center of the constricted region and continuing the process of streamer formation. Regions of ionization instability in CO_2 laser discharges are dominated by the multistep ionization processes discussed in the preceding section. In this case, the ionization rate, ν_i, is not simply a function of the effective electric field, E/N, but is a function of the power density deposited into the discharge $E \cdot J/N$. Consequently the limited power flow into the constricted discharge region reduces the ionization rate in the region and enhances stability.

The intrinsic inductance of the discharge can be estimated from the geometrical considerations shown schematically in Fig. 4.2. Also shown in Fig. 4.2 is the shape of the magnetic field for the symmetric current condition with no electron density perturbations.

SCIENCE RESEARCH LABORATORY
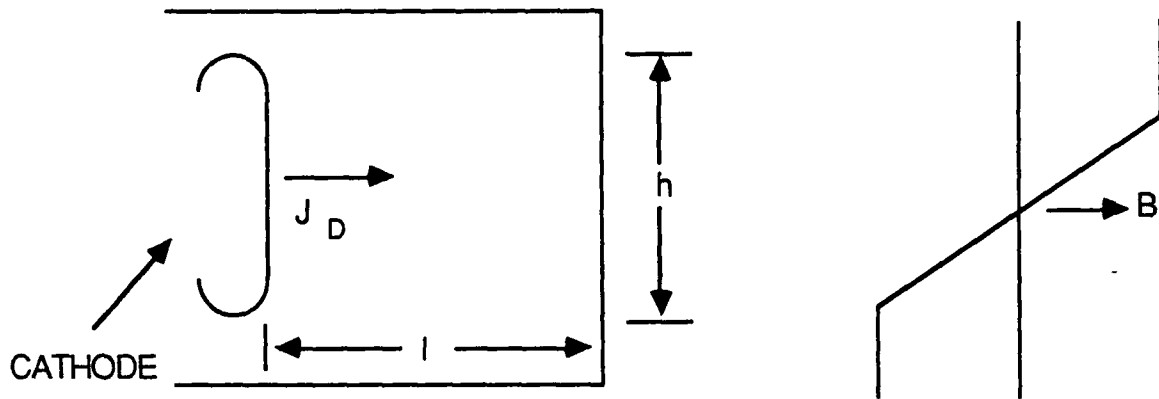
Figure 4.2: Intrinsic inductance of discharge

The discharge inductance is defined as $L_D = \int B \cdot ds/I$. For a square aspect ratio (i.e., ℓ = h in Fig. 4.2)

$$L_D = \frac{\mu_o \ell^2}{4L} \tag{4.5}$$

where L is the length of the active volume in the lasing direction and μ_o is the permeability of free space.

The inductance of the streamer representing the electron density perturbation can be calculated in a similar manner. The geometry of the streamer is shown in Fig. 4.3. Assuming that the streamer has collapsed to a radius a,

$$L_s \simeq \frac{\mu_o \ell}{2\pi} ln \frac{2\ell}{a} \tag{4.6}$$

Dividing Eq. (4.6) by Eq. (4.5) one gets $L_s/L_D \sim 2L(ln2\ell/a)/\pi\ell$. Typically $\ell = 0.15$ meters, $\ell n\, 2\ell/a \sim 4$ and $L_s/L_D \sim 20$.

To calculate the required frequency of modulation the resistance of the CO_2 discharge must be estimated. The conductivity of the discharge is typically 3×10^{-2} mhos/m. For a discharge cross section of 1.5×10^3 cm^2 and a discharge length, ℓ, of 0.15 meters, the discharge resistance is 35 ohms. The inductance as given by Eq. (4.5) is 7 nH. So for the example cited above, the RF modulation frequency should be in the range

$$5.3 \times 10^7 \frac{R_s}{R_D} Hz < f < 8 \times 10^8 Hz \tag{4.7}$$

As stated above, the upper limit on modulation frequency, 800 MHz, insures that the skin depth of the discharge is larger than the transverse dimension of the discharge so that the laser medium is pumped uniformly and efficiently. The remaining inequality relates to inductive stabilization of constrictions in the discharge current. This inequality insures that the oscillating portion of the discharge current does not contribute to the current in the constricted region. The utility of this inequality is best understood by rewriting it as $R_s/R_D < f(MHz)/53$. This inequality relates the streamer resistance (normalized to the stable discharge resistance) to the modulation frequency required to insure that the

4-5
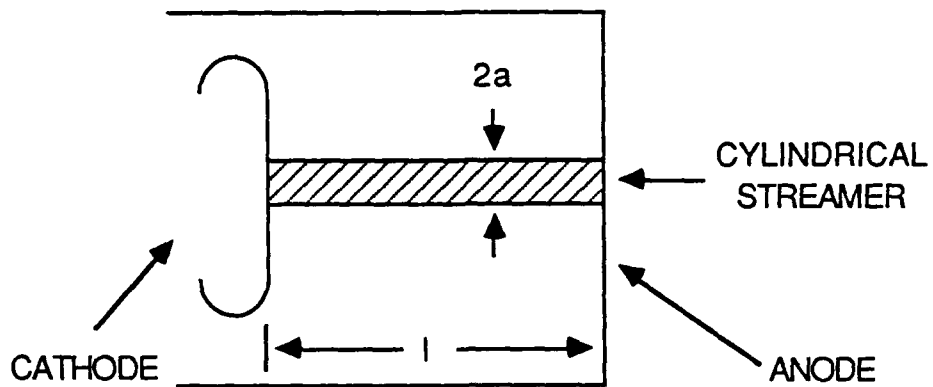
Figure 4.3: Inductance of constricted discharge

SCIENCE RESEARCH LABORATORY

oscillating current does not flow through the streamer. Initially, in the stable discharge regime R_s is infinite and therefore $R_s/R_d \gg f/53$ MHz. As the discharge constricts, R_s/R_D falls below $f/53$ MHz and the oscillating current is cut off from the constricted region. At this point, the excess electron density in the constricted region should rapidly decay thereby driving the discharge back to stable operation. If the modulation frequency in this example were chosen to be 50 MHz, then stabilization should begin to occur when the streamer resistance begins to drop below the discharge resistance, i.e. as the streamer begins to form.

4.2 TWO DIMENSIONAL RF STABILITY THEORY

Two rate equations are important in determining the stability of the discharge. The first is the electron production and loss

$$\frac{dn_e}{dt} = \nu n_m n_e - \alpha n_e^2 - \beta n_e \qquad (4.8)$$

and the second is the metastable production and loss

$$\frac{dn_m}{dt} = \langle \sigma v \rangle n_e n_a - n_m/\tau_m \qquad (4.9)$$

where n_e is the electron density, n_m is the metastable density, α is the recombination rate, β is the attachment rate, $\langle \sigma v \rangle$ is the electron impact metastable production rates constant and τ_m is the metastable lifetime. The ionization rate constant ν in Eq. (4.8) is assumed to be the result of metastable ionization. Since the metastable levels have a much smaller ionization energy than the ground state the ionization rate of the discharge is dominated by electron impact ionization of the metastables. The stability of Eqs. (4.8) and (4.9) will be analyzed assuming that the applied discharge is sinusoidally varying. Hence the various rates are determined by the local RF electric field of frequency w which is generated externally by the system shown in Fig. 4.4. From the analysis performed in Phase I Science Research Laboratory (SRL) has shown that a current source is volumetrically stable and so the initial analysis will assume an RF current source.

4-7
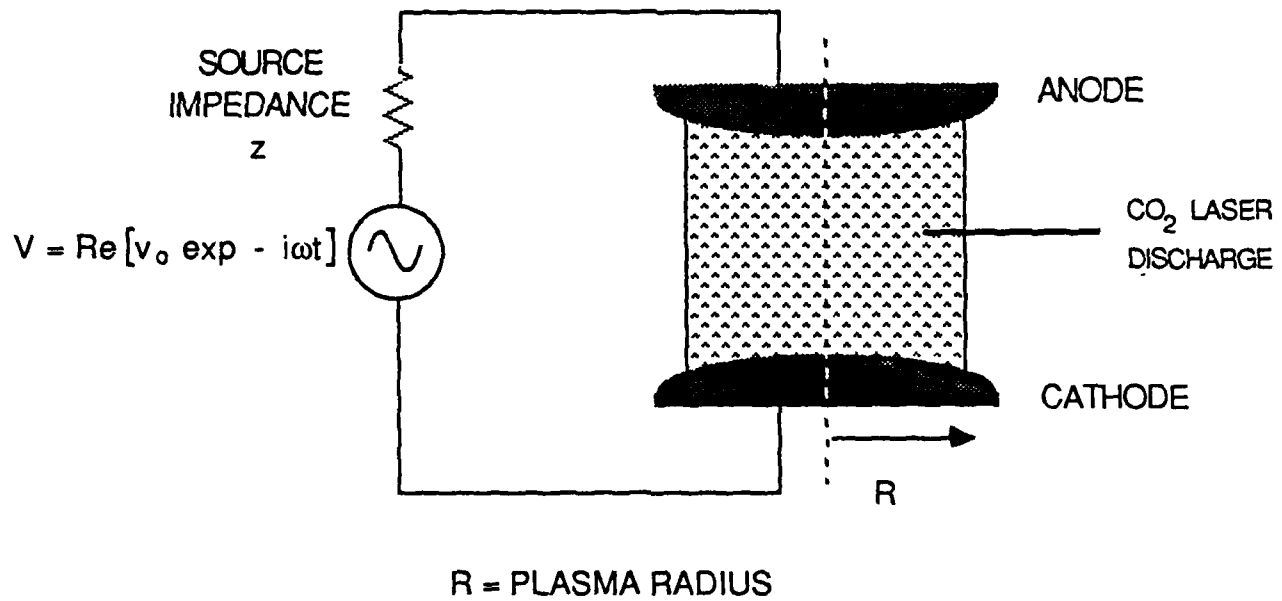
Figure 4.4: Schematic of a four dimensional discharge and electrical circuit

We shall assume now that the rates describing the variation of n_e and n_m in Eqs. (4.8) and (4.9) (i.e. νn_m, αn_e, β, $\gamma n_e / n_m$) are much smaller than $\omega / 2\pi$, so that one can use **time averaged** rate constants in these equations. On the other hand, we shall assume that $\omega / 2\pi$ is much smaller than the electron energy distribution equilibration rate ($\nu_{inelastic}$), and therefore in the above mentioned time averaging process one can use the rates corresponding to the stationary discharge with the electric field equal everywhere to the field in the RF discharge at a given time. Thus we assume

$$\nu n_m << \omega / 2\pi << \nu_{inelastic} \tag{4.10}$$

Assuming a 100 Torr discharge, $\nu n_m \sim 10^6$ sec^{-1} and $\nu_{coll}^{in} = 10^{11}$ sec^{-1}, so that 1 MHz $<< f = \omega / 2\pi << 10^2$ GHz.

At this stage it will also be assumed that the vacuum wavelength of our oscillator ($\lambda = 2\pi c / \omega$) is much larger than L, so that in the vicinity of the discharge one can neglect the relativistic retardation of time due to the extended volume, and treat the electromagnetic problem as being quasistationary. For $L = 1$ m, the condition $L << \lambda$ yields $f << c/L = 3 \cdot 10^8$ sec^{-1}. So that we are limiting our discussion to frequencies in the range 10 MHz $< f <$ 100 MHz.

The quasistationarity condition means that in the Maxwell equation for $\nabla \times \vec{B}$ one can neglect the displacement current and use the "magnetstatic" law

$$\nabla \times \vec{B} = \frac{4\pi}{c} \vec{j}(t) \tag{4.11}$$

while $\vec{E}$ is given by the Faraday law and the quasi- neutrality

$$\nabla \times \vec{E} = -\frac{1}{c} \frac{\partial \vec{B}}{\partial t} \tag{4.12}$$

$$\nabla \cdot \vec{E} = 0 \tag{4.13}$$

Equations (4.11), (4.12) and (4.13) yield

$$\nabla^2 \vec{E} = \frac{\pi}{c^2} \frac{\partial \vec{j}}{\partial t} \tag{4.14}$$

4-9

where the current density in the plasma is given by $\vec{j} = \sigma \vec{E}$, with the conductivity $\sigma = -en_e\mu$. The simplest model for the mobility μ will be used to give

$$\sigma = \frac{e^2 n_e}{m\nu_{coll}} \qquad (4.15)$$

Now we shall consider the steady state of Eqs. (4.8) - (4.9) assuming cylindrical symmetry and that

$$\vec{E} = Re(E_o e^{-\omega t})\hat{e}_z$$

Therefore, all the parameters of the steady state (n_{eo}, n_{mo}, σ_o, E_o) are functions of r alone. In steady state one obtains

$$n_{mo} = \gamma\tau n_{eo} \qquad (4.16)$$

$$n_{eo} = \frac{\beta}{\nu\gamma\tau - \alpha} \qquad (4.17)$$

All the rate constants are temporally averaged over the voltage oscillation.

Returning back to Eq. (4.7), the steady state equation gives

$$\frac{1}{r}\frac{d}{dr}\left(r\frac{dE_o}{dr}\right) + i\frac{4\pi e^2 n_{eo}}{mc^2}\frac{\omega}{\nu_{coll}}E_o = 0 \qquad (4.18)$$

The solution of this equation is (assuming $n_{eo} \simeq \text{const}(r)$)

$$E_o = AJ_o(\chi r) \qquad (4.19)$$

where

$$\chi^2 = i\frac{4\pi e^2 n_{eo}}{mc^2}\frac{\omega}{\nu_{coll}} = \frac{2i}{\delta^2} \qquad (4.20)$$

and δ is the collisional skin-depth

$$\delta = \frac{c}{\sqrt{2\pi\sigma\omega}} = \left(\frac{cm\nu_{coll}}{2\pi e^2 n_{eo}\omega}\right)^{1/2} \qquad (4.21)$$

The constant A in Eq. (4.19) can be found from the condition that the magnetic field on the surface of the plasma equals to $2I_o/cR$, where $I_o = V_o/Z$ is the current given by the external current source. From the Faraday law

$$\frac{i\omega}{c}B_\phi = (\nabla\times\vec{E})_\phi = -\frac{\partial E_o}{\partial r} \qquad (4.22)$$

4-10

so that

$$B_\phi = -\frac{ic}{\omega}\chi A J_1(\chi r) \tag{4.23}$$

and therfore

$$A = i\frac{2I_o\omega}{c^2 R\chi j_1(\chi R)} \tag{4.24}$$

In the limit of low frequencies, when

$$\frac{R}{\delta} << 1 \longrightarrow \omega << \frac{c^2 m\nu_{coll}}{2\pi e^2 n_{eo}R^2} \tag{4.25}$$

we can use the small argument expansion of the Bessel function to obtain the expression for E_o:

$$E_o(r) \simeq \frac{2I_o\omega}{c^2}\left(\frac{\delta}{R}\right)^2\left[1 - \frac{i}{2}\left(\frac{r}{\delta}\right)^2\right] \tag{4.26}$$

Condition (4.25) is important, since, as follows from (4.26), it allows one to have a radially uniform discharge in the steady state. For example, in the case of a 100 Torr laser discharge ($\nu_{coll} \sim 3\cdot 10^{11}$ sec^{-1}), $R = 3$ cm and $n_{eo} = 10^{12}$ cm^{-3}, (4.25) yields $\omega << 2\cdot 10^{10}$ ($f << 3$ GHz) which is within the quasistationary limit ($f < 100$ MHz) described earlier.

When (4.25) is satisfied, Eq. (4.26) yields

$$E_o(r) \simeq \frac{2I_o\omega}{c^2}\left(\frac{\delta}{R}\right)^2 \sim \frac{1}{n_{eo}} = \text{const}(r)$$

It is precisely this inverse dependence of E_o on n_e which assures the **global** stability of the discharge in the current source scheme. Any increase (or decrease) of the total density leads to the decrease (or increase) of E_o and therfore to the decrease (or increase) of the electron and metastable production rates. This suppresses the initial perturbation. The details of such a global stabilization by the current source are similar to those already considered previously for the DC discharge. In contrast to the DC discharge, however, the RF current source also allows to control the local, streamer type instabilities via the skin-effect. This analysis will be presented next.

4-11

4.3 STABILITY ANALYSIS

Assume that the large skin-depth condition (4.25) is satisfied for a given steady state so that n_{eo}, n_{mo}, σ_o, E_o are "almost" (to order $(R/\delta)^2$) uniform throughout the plasma volume. One can introduce a small <u>local</u> streamer type density perturbation of a characteristic transverse size Λ. The diffusion term will be added to the rate equations since non-uniformities are of interest. Hence one can write

$$\frac{\partial n_e}{\partial t} = \gamma n_m n_e - \alpha n_e^2 - \beta n_e + D_a \nabla^2 n_e \tag{4.27}$$

$$\frac{\partial n_m}{\partial t} = \gamma n_e - \frac{n_m}{\tau} + D_m \nabla^2 n_m \tag{4.28}$$

where D_a and D_m are the ambipolar and metastable atomic diffusion coefficients respectively. D_m is of the order $1/3 v_{th} \bar{\lambda} \sim 10^2$ cm^2/sec/Torr while D_a may probably be 10 times larger $(D_a \sim 10^3$ cm^2/sec Torr).

The perturabation in n_e leads to a local conductivity perturbation which in turn results in the decrease or increase in the (rms) electric field value, depending on the sign of the density perturbation. The effect is similar to the skin-effect and can be used to suppress a possible absolute instability in the discharge (as that associated with the attachment). This stabilization phenomenon will be considered in more details. In what follows, the diffusion of metastables will be neglected for simplicity. It will also be assumed that τ^{-1} is the **fastest** rate in Eqs. (4.27) and (4.28), i.e.,

$$\frac{1}{\tau} >> \nu n_{mo}, \quad \alpha n_{eo}, \quad \beta, \quad D_a/\Lambda^2 \tag{4.29}$$

Typically the rate τ^{-1} is in the few MHz region, while the other rates belong to the sub-MHz scale. For times $t > 1\mu s$, condition (4.29) Eq. (4.28) to be replaced by

$$n_m(t) \simeq \tau \gamma n_e(t) \tag{4.30}$$

(this is the fast scale analysis of the previous study) Then Eq. (4.27) becomes

$$\frac{\partial n_e}{\partial t} = (\nu \gamma \tau - \alpha) n_e^2 - \beta n_e + D_a \nabla^2 n_e \tag{4.31}$$

4-12

If $n_e = $ const, Eq. (4.31) again yields the steady state Eq. (4.17).

At this point the perturbation analysis, will be employed i.e. solution of Eqs. (4.14) and (4.31) in the form

$$\left. \begin{array}{l} n_e = n_{eo} + n_{e1} \\ \overline{E} = (E_o + E_1)e^{i\omega t}\hat{e}_z \end{array} \right\} \qquad (4.32)$$

where all the perturbations (n_{e1}, E_1) vary **slowly** in time

$$\left(\frac{1}{\omega}\left|\frac{d\ln\xi}{dt}\right| << 1, \xi = n_{e1}, E_1 \right) \quad .$$

The perturbed equations become (after the linearization):

$$\nabla^2 E_1 = -i\frac{4\pi e^2 \omega}{c^2 m \nu_{coll}}(n_{e}1E_o + n_{eo}E_1) + \left[\frac{4\pi e^2}{c^2 m \nu_{coll}} \left(\frac{\partial n_{e1}}{\partial t}E_o + n_{eo}\frac{\partial E_1}{\partial t} \right) \right] \qquad (4.33)$$

$$\frac{\partial n_{e1}}{\partial t} = [2(\nu\gamma\tau - \alpha)n_{eo} - \beta]n_{e1} + D_a\nabla^2 n_{e1} + \left[(\nu\gamma\tau - \alpha)'n_{eo}^2 - \beta'n_{eo} \right]E_1 \qquad (4.34)$$

Here $(...)' = \partial/\partial E_o (...)$. Finally, neglecting the selected term in Eq. (4.33) and using the steady state relation (4.17) in rewriting Eq. (4.34) one obtains

$$\nabla^2 E_1 = -i\frac{2}{\delta^2} \left(\frac{n_{e1}}{n_{eo}}E_o + E_1 \right) \qquad (4.35)$$

$$\frac{\partial n_{e1}}{\partial t} = \beta n_{e1} + D_a\nabla^2 n_{e1} + \beta n_{eo} \left[\frac{(\nu\gamma\tau - \alpha)'}{(\nu\gamma\tau - \alpha)} - \frac{\beta'}{\beta} \right]E_1 \qquad (4.36)$$

The skin-depth δ has again been introduced in Eq. (4.35).

At this stage a solution of Eqs. (4.35)-(4.36) in the form $n_{e1}, E_1 \sim e^{i\vec{k}\cdot\vec{r}}$ are searched for, where $|\vec{k}|^2$ is of $O(2\pi/\Lambda)$ Then one has

$$\left[-k^2 + \frac{2i}{\delta^2} \right] E_1 = -\frac{2i}{\delta^2}\frac{E_o}{n_{eo}}n_{e1} \qquad (4.37)$$

$$\frac{dn_{e1}}{dt} = (\beta - D_a k^2)n_{e1} + \beta n_{eo}B'E_1 \qquad (4.38)$$

where

$$B' = \frac{(\nu\gamma\tau - \alpha)'}{(\nu\gamma\tau - \alpha)} - \frac{\beta'}{\beta} \qquad (4.39)$$

By substituting E_1 from (4.37) into (4.38) one obtains

$$\frac{dn_{e1}}{dt} = [(\beta - D_a k^2 - \frac{4\beta n_{eo}E_0 B'}{k^4\delta^4 + 4}) + i\frac{2\beta n_{eo}E_0 B'k^2\delta^2}{k^4\delta^4 + 4}]n_{e1} \qquad (4.40)$$

4-13

Since $k > 2\pi/R$ *and* $S >> R$ one finds $(k\alpha)^4 >> 4$ and therefore (4.40) reduces to

$$\frac{d(\ln n_{e1})}{dt} = \beta - D_a k^2 - \frac{4\beta n_{eo} E_0 B'}{k^4 \delta^4} + L \quad \frac{2\beta n_{eo} E_o B'}{k^2 \delta^2} \tag{4.41}$$

The last equation shows that a stable operation corresponds to the case

$$\Phi \equiv \beta - D_a k^2 - \frac{4\beta n_{eo} E_o B'}{K^4 \delta^4} < 0 \tag{4.42}$$

One observes that there exist two stabilizing phenomena in the system. The first is due to the diffusion and is effective in stabilizing **short scale** density perturbations The diffusion simply smoothes the short scale non-uniformities. The second phenomenum is basically the skin effect. It is more important in suppressing larger scale perturbations, espesially those of size comparable to the radious of the plasma column.

The interplay between the two stabilizing processes can be demonstrated by drawing the curve showing the dependence of $\Phi = \Phi(k^2)$ (see Eq. (4.42)). A typical situation is shown in Fig. 4.5.

$\Phi(k^2)$ reaches its maximum value

$$\Phi_m = \beta - 2.05 \left(\frac{4\beta n_{eo} E_o B' D_a^2}{\delta^4} \right)^{1/3} \tag{4.43}$$

at

$$k_m^2 = \left(\frac{8\beta n_{eo} E_o B'}{D_a \delta^4} \right)^{1/3} \tag{4.44}$$

Therefore, in case $k_m > 2\pi/R$, the stability condition for the entire k - space becomes

$$\beta < 2.9 \left(\frac{4 n_{eo} E_o B' D_a^2}{\delta^4} \right)^{1/2} \equiv G(\sim wn_{eo}^{3/2}) \tag{4.45}$$

Note that the stable operation is easier at higher frequencies and plasma densities. Note also that the final value of Da is important, since (38) can not be satisified for $D_a \longrightarrow 0$.
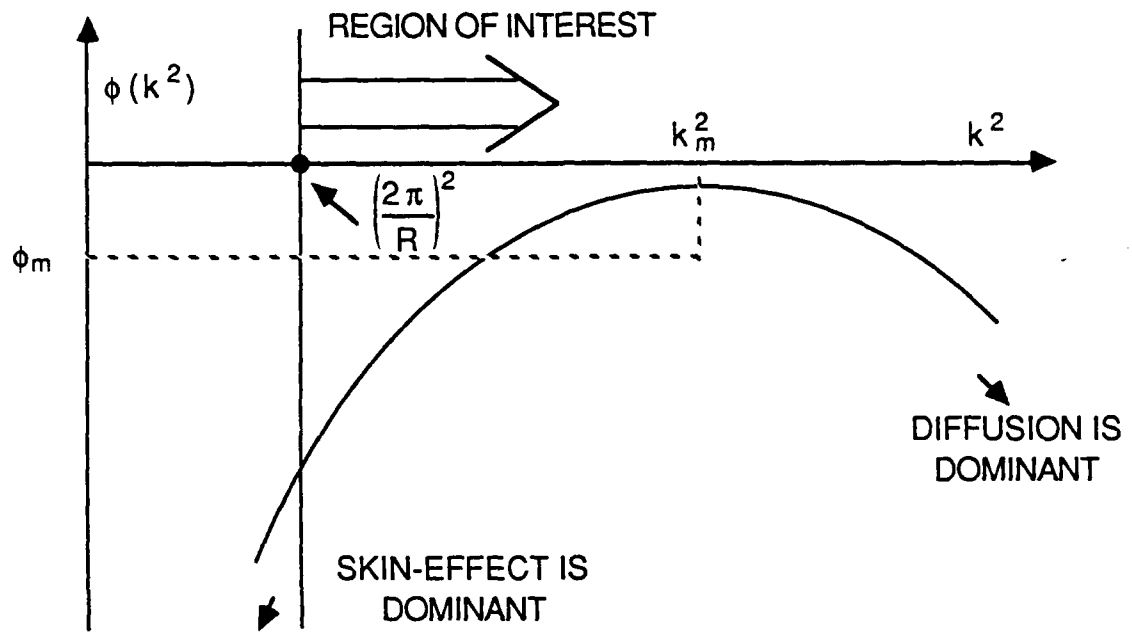
Figure 4.5: Plot showing the functional dependence of $\Phi(k^2)$ vs k^2

4-15

4.4 NUMERICAL SIMULATIONS OF THE TWO DIMENSIONAL CODE

SRL has developed a code based on the two dimensional theory presented earlier in this section. The basic equation is (4.18) which can be in rectlinear coordinates as

$$\frac{\partial^2 E}{\partial x^2} + \frac{i4\pi e^2 n_{eo}}{mc^2} \frac{\omega}{\nu_{coll}} E_o = 0 \tag{4.46}$$

subject to the boundary conditions

$$\frac{\partial E}{\partial x}\Big|_{x=0} = 0 \quad \text{and} \quad \frac{\partial E}{\partial x}\Big|_{x=w} = -\frac{2\omega I_o}{c^2}$$

where I_o is the total current per unit length. Equation (4.46) is valid for a slab geometry i.e. where the z dimension is much longer than x-dimension. Such a geometry conforms more to the CO_2 lasers than the radial geometry. As discussed in Chapter 2 the frequency of osicllation $f >> \alpha n_e$ hence the electron density will remain essentially constant during a period of oscillation. This allows one to use time averaged rates for α, ν and $\langle \sigma v \rangle$. These time averaged rates are defined by the following integral

$$\bar{\xi} = \frac{\omega}{\pi} \int\limits_{0}^{\pi/\omega} \xi(\mid E \mid \sin\omega t)dt = \frac{1}{\pi} \int\limits_{0}^{\pi} \xi(E_o \sin s)ds = \bar{\xi}(\mid E \mid) \tag{4.47}$$

where $\xi = \nu$, α and $\langle \sigma v \rangle$.

In Eq. (4.47) $\mid E \mid$ is just the amplitude of the electric field

$$\mid E \mid = \{(ReE)^2 + (I_m E)^2\}^{1/2} \tag{4.48}$$

For efficient simulation one has to obtain **analytic** expressions for $\bar{\nu}$, $\bar{\alpha}$ and $\langle \sigma v \rangle$ as functions of $\mid E \mid$. It is also convenient to introduce a dimensionless coordiante $\rho = x/w$ in which case Eq. (4.46) can be rewritten as

$$\frac{\partial^2}{\partial \rho^2} E + 2i \left(\frac{w}{\delta}\right)^2 E = 0 \tag{4.49}$$

where the skin depth δ is given by

$$\delta = \left(\frac{c}{2\pi\sigma\omega}\right)^{1/2} = \left(\frac{cm\nu_{coll}}{2\pi e^2 n_e \omega}\right)^{1/2}$$

As stated in Chapter 2 the discharge width $\omega << \delta$ and so one can solve Eq. (4.46) by a perturbation expansion by introducing the small parameter $\Delta = (w/\delta)^2$. The electric field can be expanded as

$$E = E_o + E_1 + E_2.......$$

where the terms are ordered in powers of Δ then Eq. (4.46) gives the following orders

$$\frac{\partial^2 E_o}{\partial \rho^2} = 0 \tag{4.50}$$

$$\frac{\partial^2 E_1}{\partial \rho^2} + 2i\Delta E_0 = 0 \tag{4.51}$$

$$\frac{\partial^2 E_2^2}{\partial \rho^2} + 2i\Delta E_1 = 0 \tag{4.52}$$

$$.....etc.$$

Equation (4.50) perdicts E_0 is constant which after substitution into (4.51) results in

$$E_1(\rho,t) = -2iE_0 \int\limits_0^\rho d\rho' \int\limits_0^{\rho'} \Delta(\rho'')d\rho'' \tag{4.53}$$

Similarly

$$E_2(\rho,t) = -2i \int\limits_0^\rho d\rho' \int^{\rho'} d\rho E_1 \Delta d\rho'' \tag{4.54}$$

etc. The SRL code solves the first order equation given by

$$E(\rho,t) = E_o \left(1 - 2i \int_0^\rho d\rho' \int\limits_0^{\rho'} \Delta(\rho'',t)d\rho'' \right) \tag{4.55}$$

The constant E_o can be found from the boundary condition on the total current

$$\frac{\partial E}{\partial \rho}\Big|_{\rho=1} = -\frac{2i\omega I_o}{c^2} = -2iE_o \int\limits_0^1 \Delta(\rho',t)\rho'd\rho'$$

or

$$E_o = \frac{\omega I_o}{c^2} \Big/ \int_0^1 \Delta(\rho',t)\rho'd\rho' \tag{4.56}$$

The numerical code results will be presented next. The particular slab geometry analysed is shown in Fig. 4.6. The discharge is assumed to be 2.4 cm wide in the x- direction and

4-17
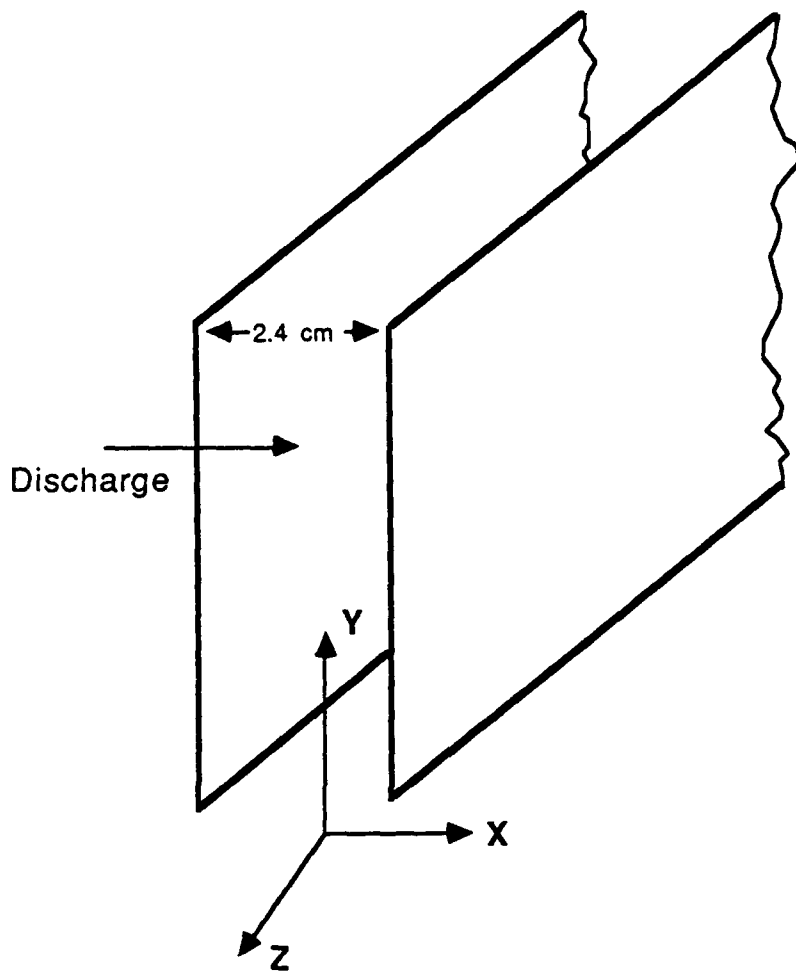
Figure 4.6: Schematic of discharge geometry

long in the z direction. The electric field is applied in the y direction. The origin of the abscissa is located at the center of the discharge i.e. the discharge extends between -1.2 cm to 1.2 cm in the x- direction. The stiff current drive will be discussed first since it was the most stable.

4.4.1   A Stiff Current Case

Figure 4.7 shows the temporal and spatial variation of n_e for the discharge between $0 \leq x \leq 1.2$ cm. The discharge is assumed to be symmetric hence $- 1.2$ cm $\leq x \leq 0$ will just be the mirror image about the ordinate of the plots shown in Fig. 4.7. Also it was assumed that the total current was 2.4 A/cm and the applied electric field was 400 V/cm and the CO_2 laser mixture was 3/2/1 at a total pressure of 30 Torr. The initial spatial electron density was assumed to be slightly greater than 10^{11} cm^{-3} with a non uniformity of 5% between the centre of the discharge and the edge. The attachment rate for electrons was assumed to be 50 μs. The spatial variation of the electrons is shown every 5 μs. The initial spatial profile is labled 1. The curve labled 2 is spatial profile 5 μs later etc. The electron density increased by 20% in the first 10 μs and then decrease by 10% during the next 50 μs. Also the non uniformity at the end of 45 μs increased to about 10%. Figure 4.8 shows the results of the next 45 μs. The curves in Figure 4.8 are spaced every 10 μsec. The curve labled 1 in Fig 4.8 is the same as the curve labled 10 in Fig. 4.7. The curve labled 2 shows the spatial variation of n_e 10μs later, etc. The dominant effect is the continual increase in the non uniformity. The uniformity at the end of 85 μs is 25%.

The result shown in Fig. 4.7 and 4.8 show for the conditions assumed the discharge was stable for about 100 μs. However the spatial non-uniformity increases temporally indicating the discharge will eventually be unstable and arcing will occur. From the many code runs analysed it is clear that a spatial non-uniformity and a finite attachment rate results in an unstable discharge even for a stiff current source and the key for stable operation is to obtain as uniform an initial electron density as possible and to keep the electron attachment rate as small as possible.
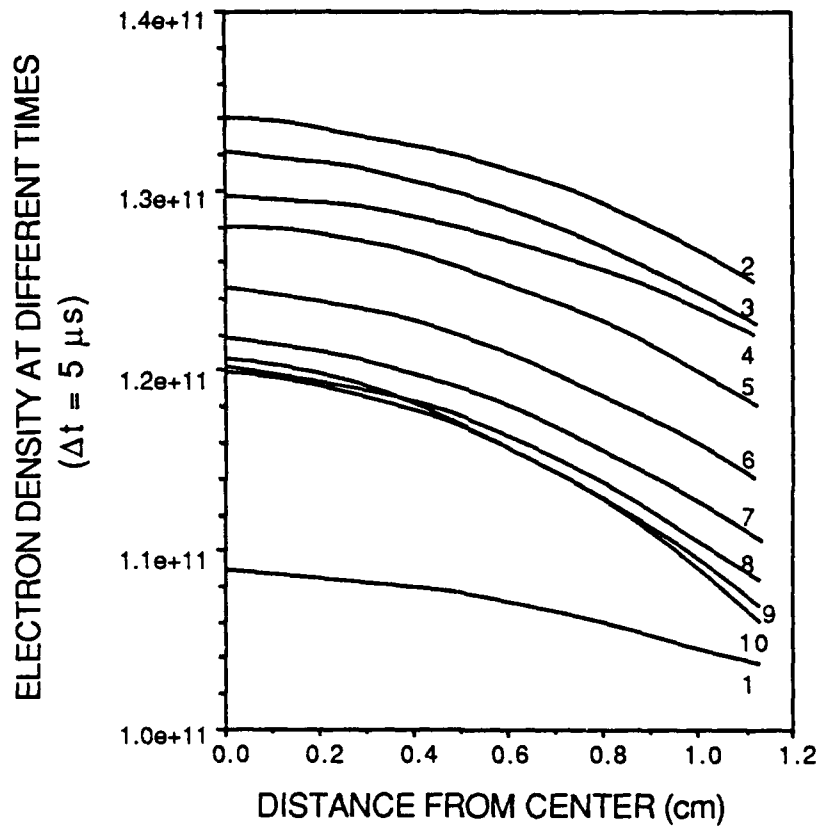
Figure 4.7: Plot showing the spatial and temporal variation of the electron density n_e. Curve 1 is the initial spatial variation of n_e at $t = 0$. Curve 2 is the spatial variation of n_e at $t = 5 \mu s$, etc. The power supply is assumed to be a stiff current source.

4-20
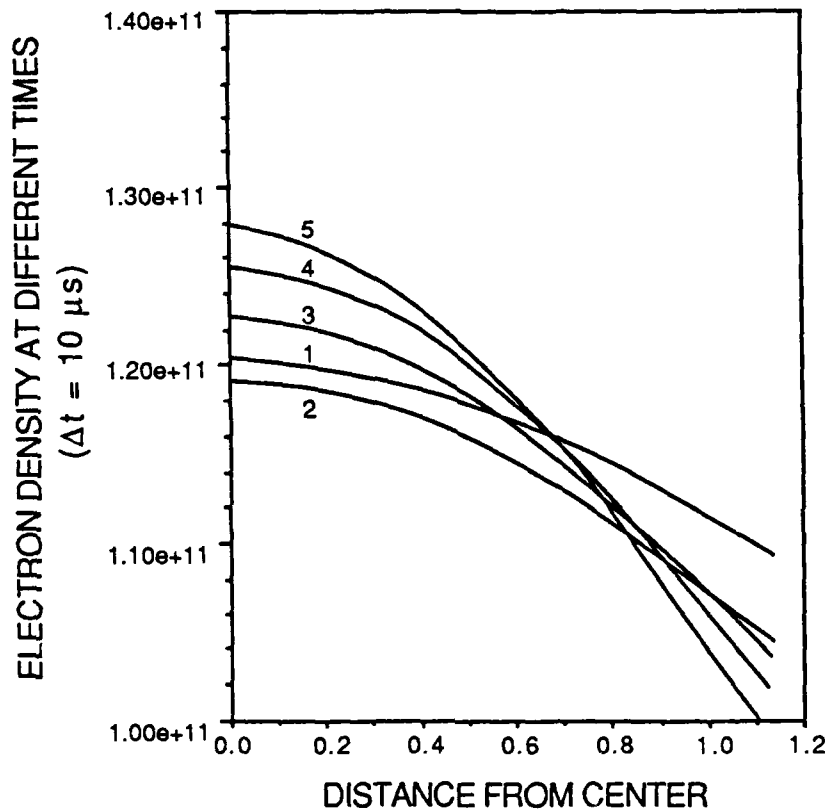
Figure 4.8: The curve labled 1 is the same as the curve labeled 10 in Figure 4.7. This figure shows the spatial variation of n_e every 10 μs.

4.4.2 Stiff Voltage Source

Figures 4.9 and 4.10 show the results of a stiff voltage source for the same conditions discussed previously. In Fig. 4.9 the initial electron density was again chosen to be about 1.1×10^{11} cm^{-3}. The electron density increases by over an order of magnitude in 30 μs. In this figure the spatial variation in the electron density is shown every 3 μs as apposed to every 5 μs in Fig. 4.7 and every 10 μs in Fig. 4.8. This discharge is clearly unstable and it will result in an arc well before the 100 μs pulse length. Figure 4.10 shows the results of initializing the electron density to 10^{10} cm^{-3}. In this case the discharge is clearly quenched. These results are remincent of the one dimensional stiff voltage results shown in Figs. 3.11 and 3.12 where discharge is unstable and it proceeds to an arc or its is quenched depending on the initial electron density. So once again it is clear that the stiff current source is more stable than a stiff voltage source.

SCIENCE RESEARCH LABORATORY
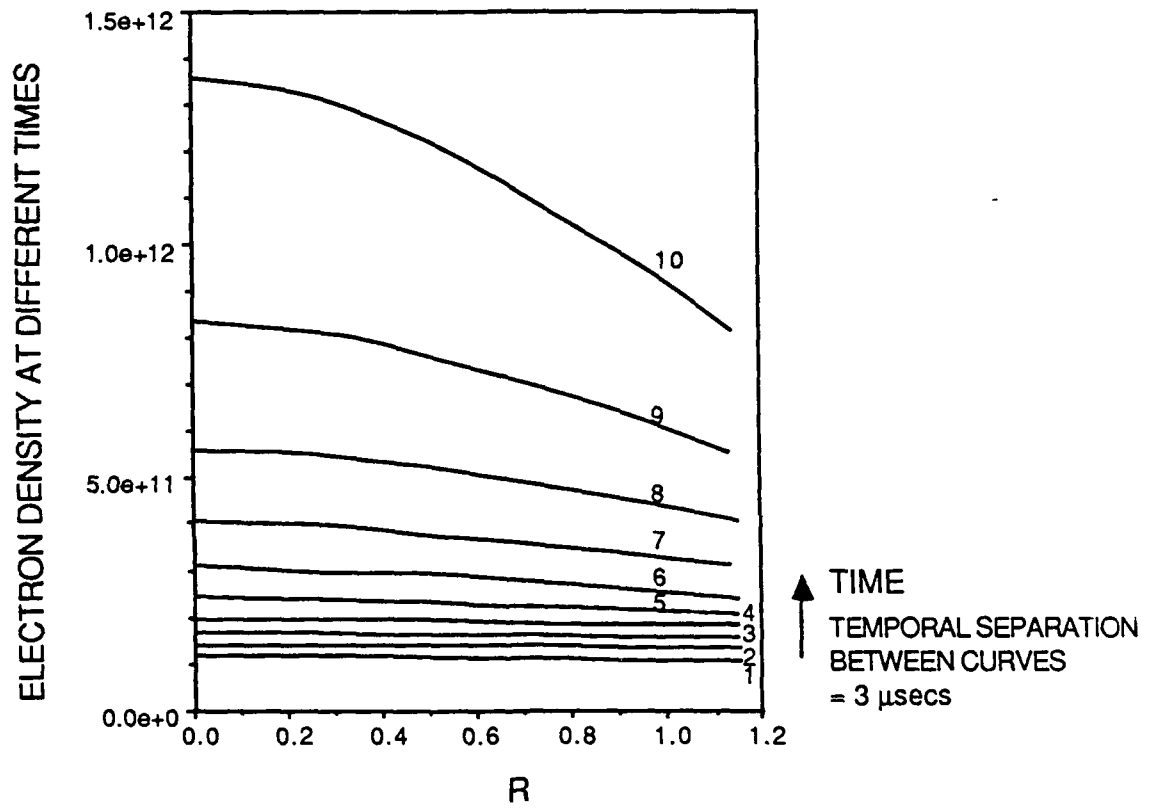
Figure 4.9: Same as Figures 4.7 and 4.8 except that power supply is assumed to be a stiff voltage source and the spatial variation of n_e is shown every 3 μs.
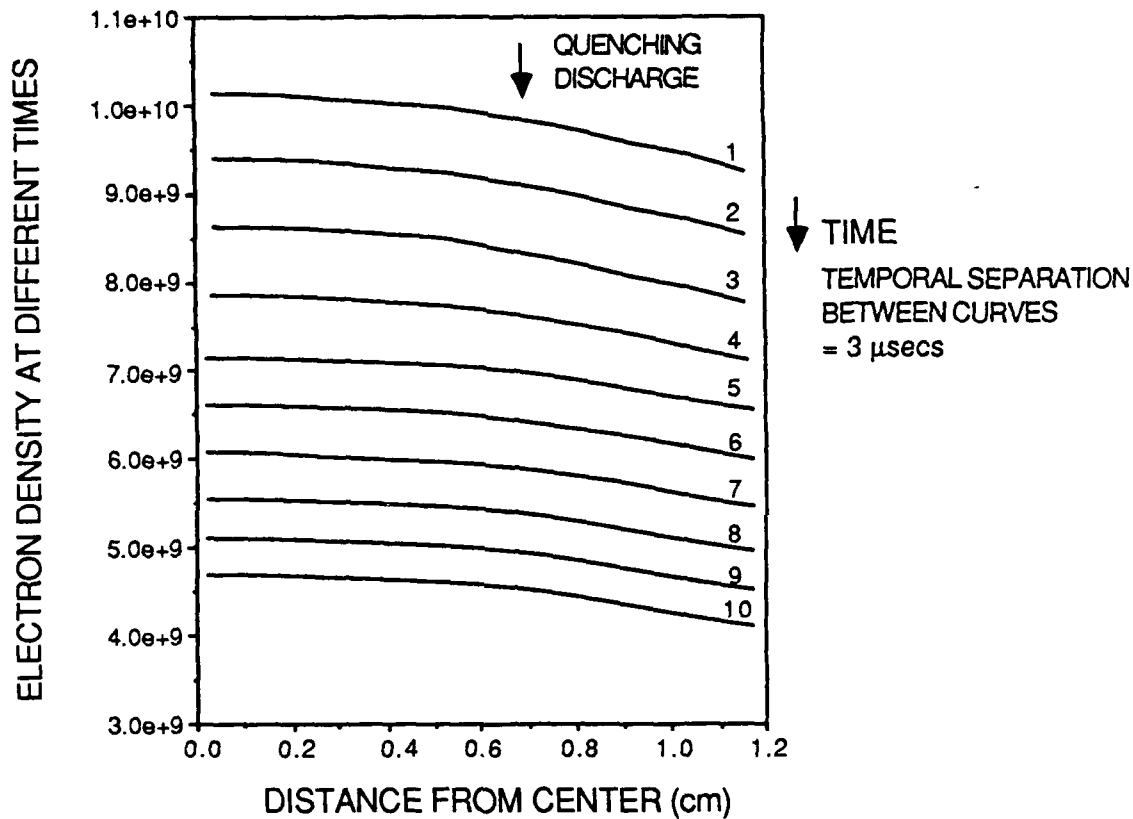
Figure 4.10: Same as Figure 4.9 except that n_e was initialized at 10^{10} cm^{-3}

SCIENCE RESEARCH LABORATORY

CHAPTER 5

CONCEPTUAL DESIGN OF A REPETITIVELY PULSED CO_2 LASER

In this chapter a conceptual design of the laser head and the RF pulse power to drive it will be presented. An assembly drawing of the laser head is shown in Fig. 5.1. The laser head is designed with several spark plugs that provide UV preionization. The waste heat will be removed by conduction to the side walls. Such a design eliminates the flow loop and results is a considerably lighter weight CO_2 laser. Also the design is simpler and subsystems such as a blower and sidewall mufflers are eliminated. The anode and cathode were designed using a Chang profile thereby insuring that the electric field at the edge of the electrodes do not increase substantially. Such an increase in the electric field could result in arcing. The motivation behind choosing the laser head design will be discussed in the remainder of this section.

5.1 GEOMETRIC CONFIGURATION OF THE CO_2 LASER HEAD

In order to size and configure the laser head, several issues must be considered including

- Specific extractable laser energy
- Gas Cooling Method
- Preionization Method
- Efficiency of Optical Extraction

The specific energy extractable from CO_2 lasers is typically 50 J/liter atm. SRL proposes to operate the laser at 30 Torr or 1/25 of an atmosphere and hence we plan to extract approximately 2 J/liter. Therefore a 6 liter laser volume will be adequate for demonstrating the 12 J laser pulse energy required for SDIO applications.

The next design consideration centers on the fact that one of the dimensions is constrained by conduction cooling to be about 2.4 cm. This constraint comes from the fact that the CO_2 laser efficiency decreases at elevated temperatures hence there is a maximum temperature difference that can be tolerated between the walls and the axis of the discharge cell under repetitive pulse operation.

5-1
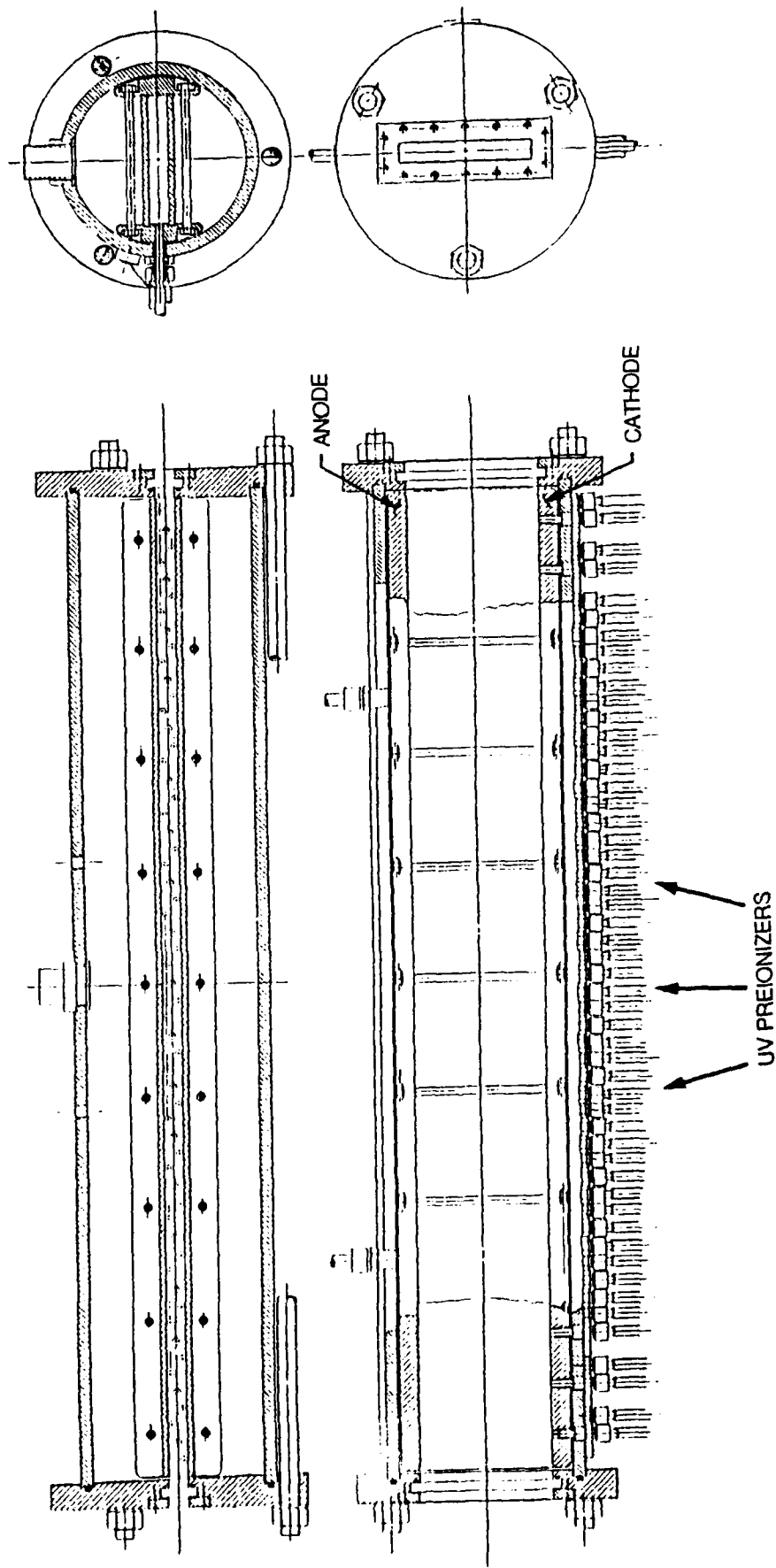
Figure 5.1: Assembly drawing of repetitively pulsed CO_2 laser head

For efficient laser power extraction the integrated optical length through the laser device must be $\geq$ 500 cm. SRL proposes to use a cylindrically expanding beam that will be folded into four passes. Therefore a discharge length of 125 cm will be adequate. The third dimension then must to be 20 cm to provide the required 6 liter volume. Figure 5.2a schematically shows the discharge volume and Fig. 5.2b shows the four folds that enables one to take the expanding beam geometry shown in Fig. 5.3 and make it compatible with a rectangular geometry. The discharge voltage will be applied across the 20 cm length and the UV preionization will be introduced by the use of spark plugs that are placed behind a cathode mesh.

5.2 CO_2 LASER DISCHARGE CHARACTERISTICS

The performance of CO_2 laser discharges is determined by several parameters including electron and gas temperature, gas mixture and the type and level of preionization. For efficient laser operation one must choose the appropriate laser mixture and electric field. The mixture of choice for efficient long pulse CO_2 laser operation is a 3/2/1, $He/N_2/CO_2$ mixture. The rate constants for the ionization and excitation of the electronic states of N_2, the fraction of discharge energy that goes into vibrational excitation. the drift velocity and electron temperature as predicted by the Boltzmann code are shown in Figs. 3.4. 3.5 and 3.6. From Fig. 3.4. in which T_e. v_d and the efficiency of exciting the vibrational levels of N_2 are plotted against the discharge electric field, it is clear that efficient CO_2 laser operation occurs at electric fields between 5-10 kV/cm-atm. Thus for a total mixture pressure of 30 Torr the appropriate electric field will be 200-400 V/cm. A consistent set of CO_2 laser discharge characteristics for generating a 12 joule laser pulse (30 μsec) are given in Table 1. These discharge characteristics have been developed using the comprehensive SRL pulsed CO_2 laser model.

20 cm

2.4 cm
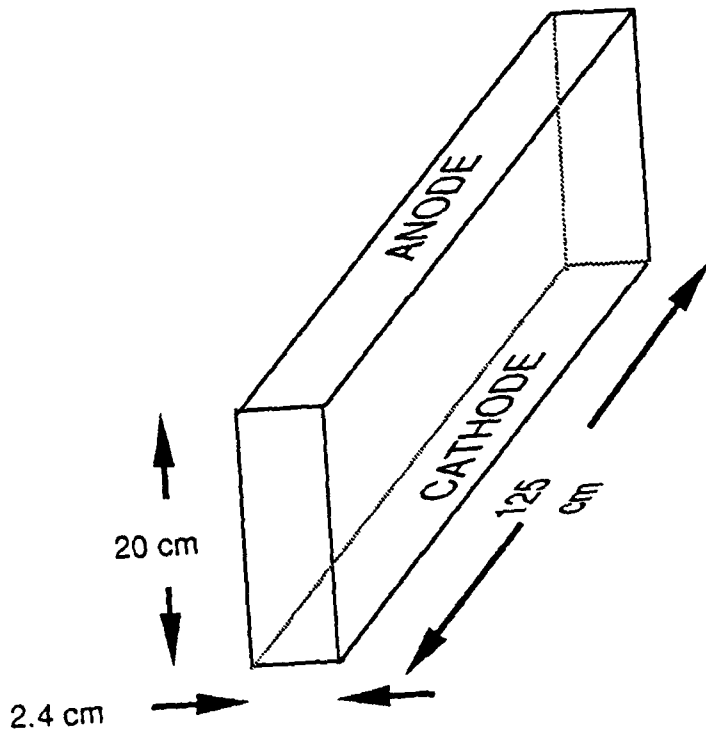
Figure 5.2a: CO_2 gain medium geometry

INJECTED
LASER BEAM

AMPLIFIED
LASER BEAM

20 cm

125 cm
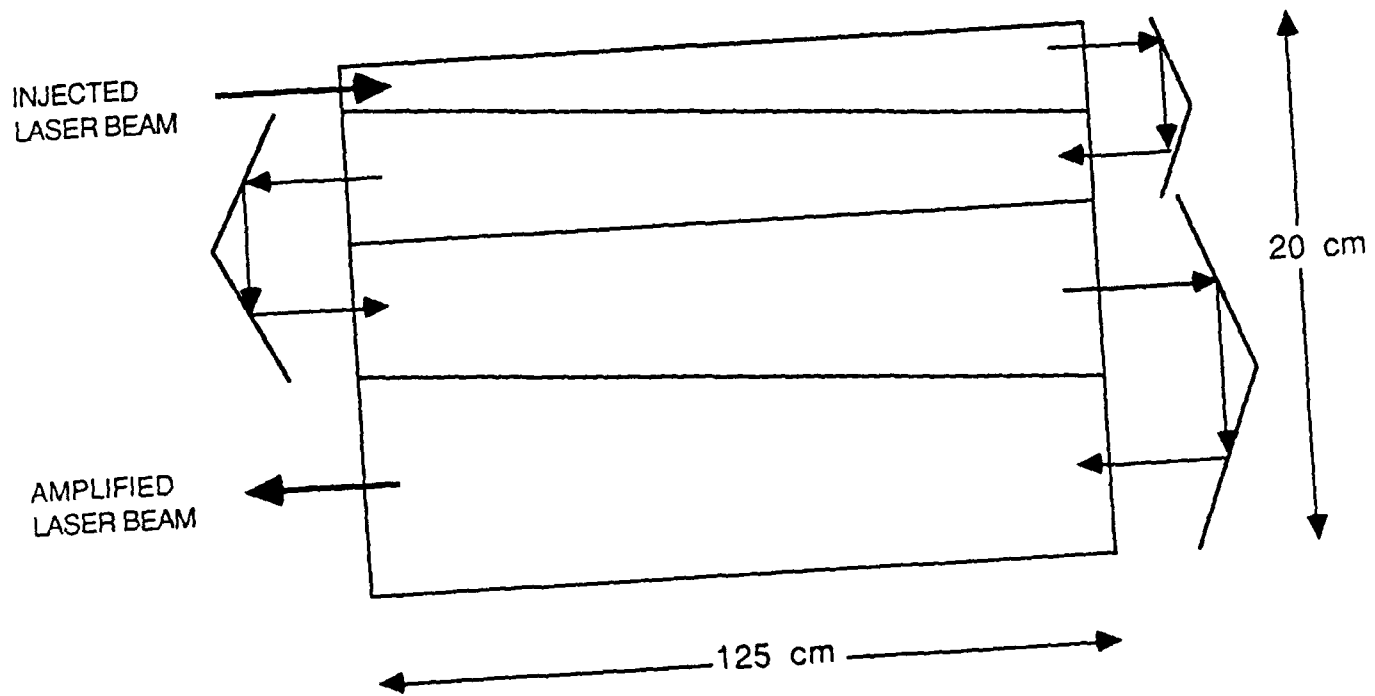
Figure 5.2b: Using four optical folds, the expanding
beam geometry in Figure 5.1 can be made
compatible with regular geometry.

SCIENCE RESEARCH LABORATORY
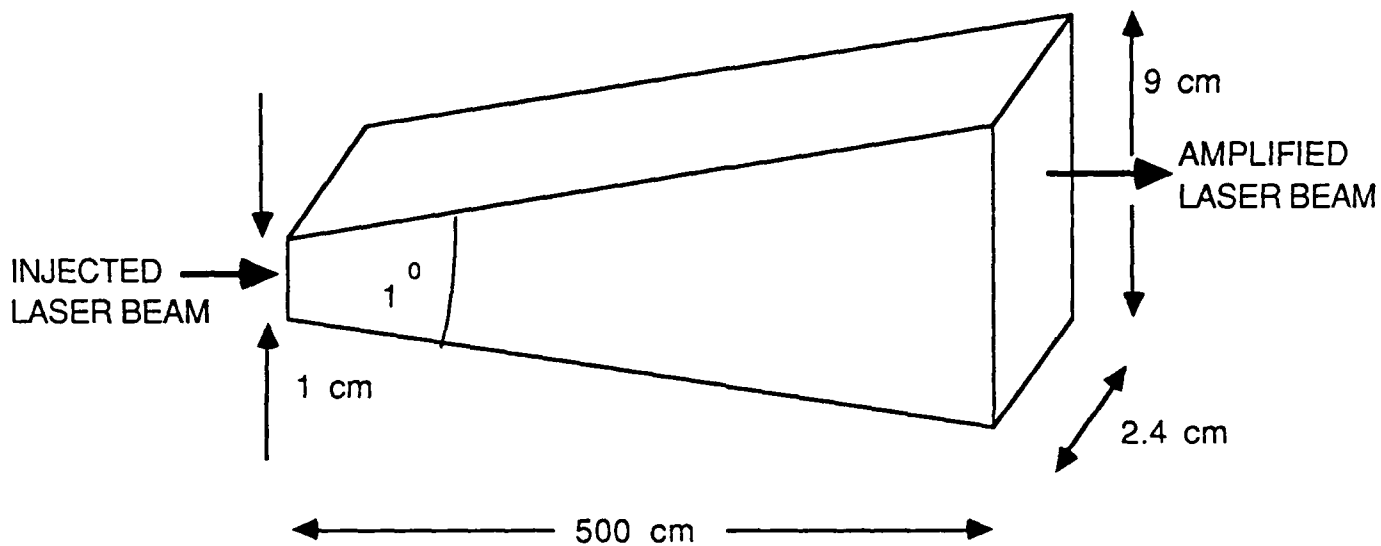
Figure 5.3: Expanding beam amplifier concept

SCIENCE RESEARCH LABORATORY

Table 1: CO_2 Laser Discharge Characteristics

- Discharge Volume $2.4 \times 20 \times 125 \ cm^3$
- Discharge Electric Field $400 \ V/cm$
- Discharge Voltage $8 \ kV$
- Current Density $1 \ A/cm^2$
- Total Current $240 \ A$
- Discharge Impedance $33.3 \ \Omega$
- Energy Delivered to Discharge $72 \ J$

The CO_2 laser to be designed in the proposed effort will be UV preionized. Typically UV preionization results in a low level of electron density ($\simeq 10^6$ - $10^8 \ cm^{-3}$) that has to be avalanche four to six orders of magnitude. This laser will also have a prepulse at the front end of the main discharge pulse. It is convenient to design the prepulse to have a voltage which is approximately twice the voltage of the main discharge pulse which means that the electric field will be about 600-800 kV/cm during this 250 nsec prepulse duration. Figure 5.4 shows the variation of the ground state ionization rate constant ν_a as a function of the applied electric field. At an electric field of 600 V/cm, the value of ν_a is about 2×10^{-10} cm^3/sec, so for a density of $10^{18} \ cm^{-3}$, the ionization rate $\nu_a n_a \sim 10^8$ electrons/cm^3/sec and the electron density will exponentiate every 20 nsec. As discussed earlier in this section, the electron density must increase 4-6 orders of magnitude or 9-14 exponentiations which corresponds to a prepulse duration of 200-300 nsec. At the larger electron densities of 10^{12} cm^{-3} that are required for efficiently pumping CO_2 lasers, the dominant ionization process will be two step ionization from metastable levels. In this ionization process, discharge electrons first produce metastable electronic states and then in a second collision take these excited states into the ionization continuum. Under SDIO/ONR funding, SRL has developed a pulsed CO_2 laser driver which efficiently uses a single circuit to provide the preionizer pulse, the prepulse, and a main discharge pulse.

5.3 OPTICAL CONFIGURATION

An amplifier is much more desirable than an oscillator if a CO_2 laser beam optical

SCIENCE RESEARCH LABORATORY

quality of better than 1.3 XDL and a spectral width of less than 100 kHz are required. However, to reduce the weight of the system the amplifier gain must be as large as possible. This last criterion of large amplifier gain can be met by using the expanding beam concept.[8] This design concept which has been pioneered by and experimentally verified by SRL under SDIO sponsorship makes use of optical beam whose area changes as it propagates through the amplifier. Such a configuration is shown in Fig. 5.3. The injected beam which has a cross-sectional area of 1×2.4 cm^2 expands cylindrically to an area of 9×2.4 cm^2 over the gain length of 500 cm. From this geometry it is clear that the amplifier gain is the product of the area gain g_A and active media gain $\exp(gL)$, where gL just the laser gain length product along a ray through the gain medium. Amplified spontaneous emission (ASE) and parasitic modes that can decrease the laser efficiency depend on (exp gL) only. Hence this geometry lends itself to a much higher gain per stage than the usual rectangular extraction geometry.

This fact is shown graphically in Fig. 5.4 which is a plot of the amplifier gain vs extraction efficiency for two cases. The first curve is for the expanding beam geometry shown in Fig. 5.4. Note as the amplifier gain decreases (this corresponds to increasing the injection level) the extracted efficiency increases. Also shown in Fig. 5.4 is the amplifier gain vs extraction efficiency for the rectangular cavity shown in Fig. 5.5 which has the volume and gain length as the expanding beam laser cavity of Fig. 5.3. The extraction efficiency of the rectangular cavity is always lower than the expanding beam. Even more significant, however, is that the conventional laser cavity design will need isolation for a gain of greater than 100. This becomes clear upon looking at curve 4 that predicts the extraction efficiency of a rectangular geometry in the presence of 1% specular reflection from windows or other optical elements in the beam train. The rapid decrease of the extraction efficiency for stage gains of > 100 is a result of amplified spontaneous emission (ASE). From curve 2 it is clear that the EBL is relatively insensitive to ASE which is due to the beam expansion which reduces the intensity feedback by specular reflection

SCIENCE RESEARCH LABORATORY
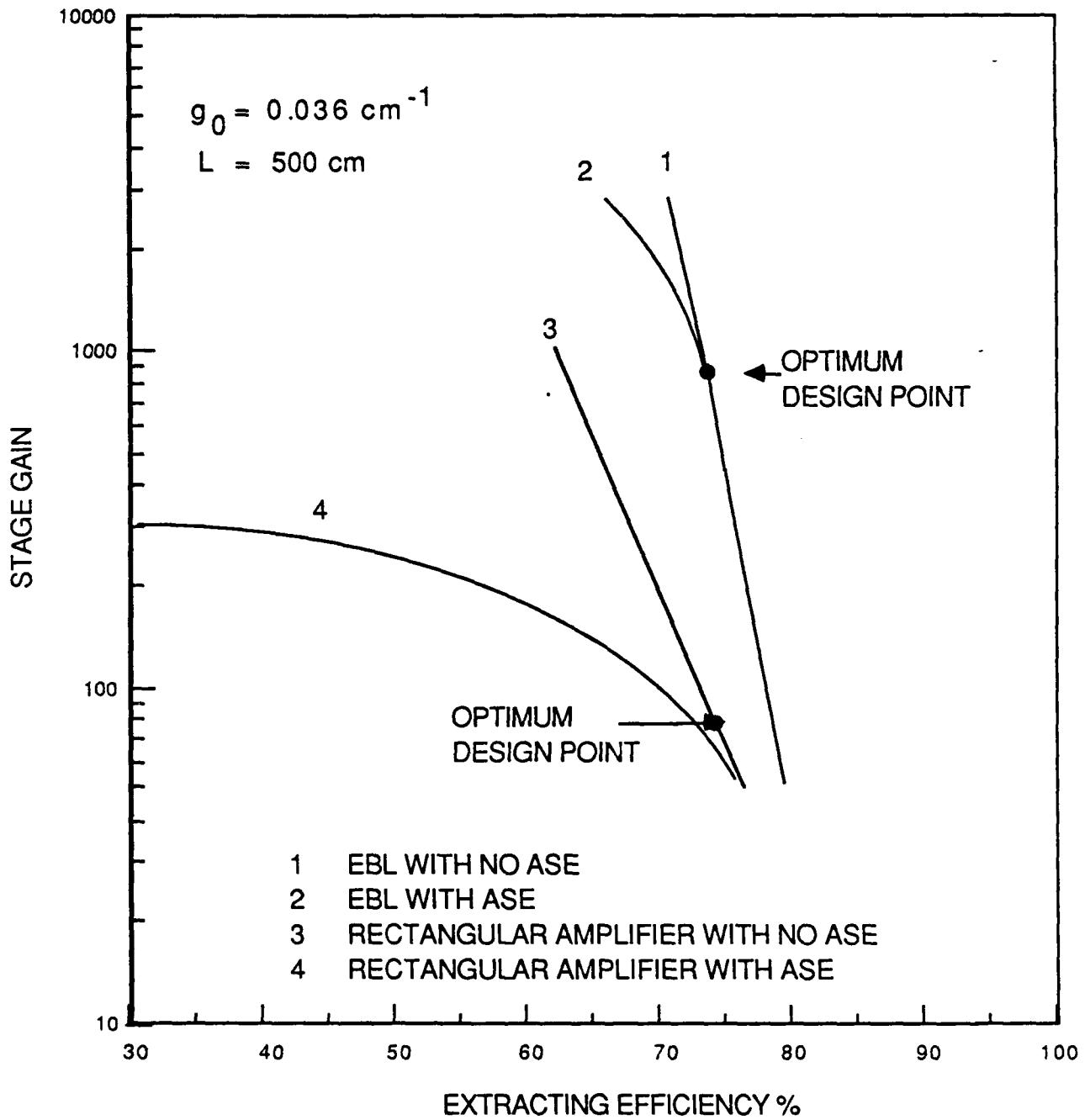
Figure 5.4: Curves showing the extraction efficiency as a function of stage gain for the EBL and the rectangular amplifiers.
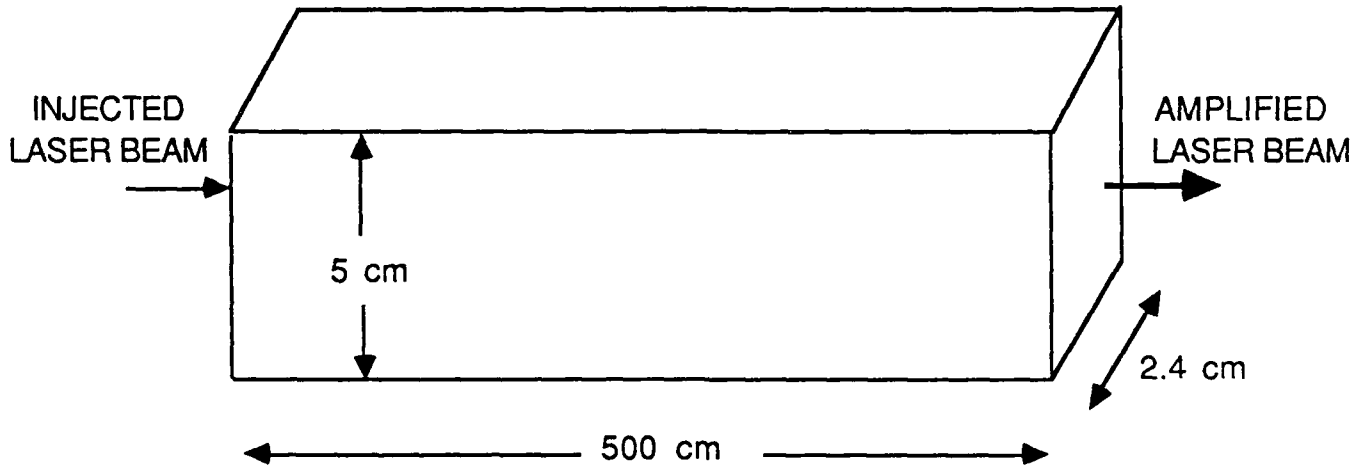
Figure 5.5: Single pass conventional rectangular laser geometry

by an order of magnitude. These ASE calculations are discussed in greater detail in the following subsection. From the curves in Fig. 5.4 it is clear that one cannot build an CO_2 laser amplifier as a single 500 cm gain length for gains > 100 because of ASE and parasitic modes. This can be compared to an amplifier gain of 1000 for the expanding beam geometry.

The active medium as shown in Fig. 5.6 is unconventional and it is difficult to configure a CO_2 laser discharge into such a volume. However, the optical beam can easily be folded and into a rectangular laser discharge volume so the single pass configuration shown in Fig. 5.3 can be reduced to the four pass rectangular discharge region shown in Figs. 5.2b and 5.7. The length of the discharge region is reduced to 125 cm. The cross-sectional area is 20×2.4 cm^2.

5.4 LASER GAIN AND EXTRACTION EFFICIENCY

Having established the discharge conditions and the optical configuration, the laser gain and optical extraction efficiency can be calculated. To accomplish this calculation, SRL has used a combination of CO_2 laser codes which have been developed over the past 4 years. The first is a CO_2 laser/discharge code that predicts the small signal gain for the discharge conditions given in Table 1. The small signal gain as predicted by that code is shown by the curve in Fig. 5.7. It is interesting to note that the gain increases linearly for the first 10 μs indicative of the long life time $\simeq 100$ μs of the upper level. The predicted laser characteristics are summarized in Table 2.

Table 2: Laser Characteristics

- Peak small signal gain 3.65×10^{-2} cm^{-1}
- Injected power   1 kW
- Peak output power   800 kW
- Energy per pulse   12 joules
- Discharge energy deposited   72 joules

SCIENCE RESEARCH LABORATORY

ANODE

CATHODE

20 cm

125 cm

2.4 cm

HIGH
VOLTAGE
INPUT

ELECTRICALLY INSULATING
SIDE WALLS
(WASTE HEAT REMOVAL OCCURS
 THROUGH SIDE WALLS)

CATHODE
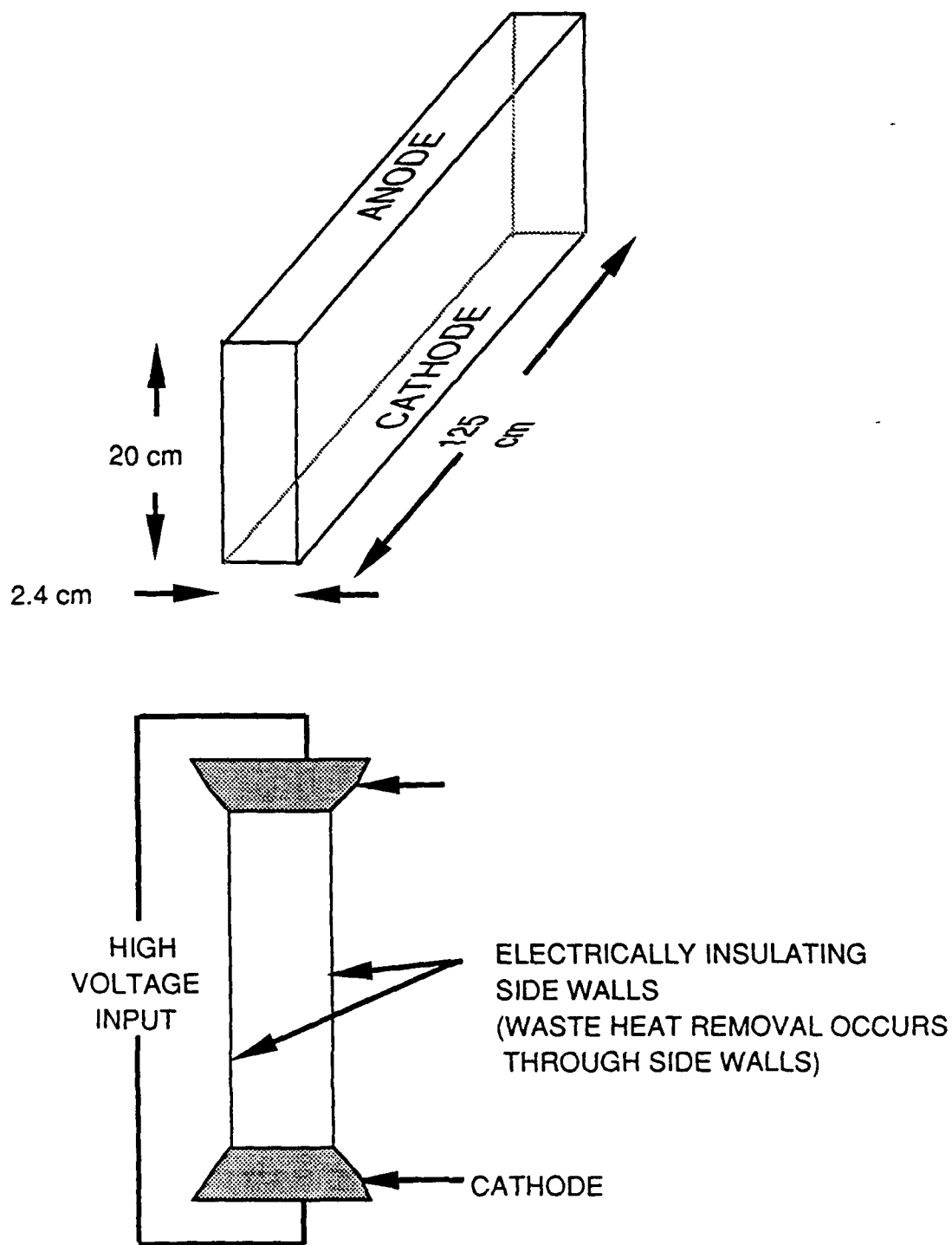
Figure 5.6: Schematic of CO_2 laser head

SCIENCE RESEARCH LABORATORY

TEMPORAL PULSE SHAPE

LASER MIXTURE   = 3/2/1
ENERGY OUTPUT   = 12 Joules
INTRINSIC EFFICIENCY = 16.8%

OUTPUT LASER POWER (kw) vs TIME (μS)

SMALL SIGNAL GAIN

SMALL SIGNAL GAIN (% / cm) vs TIME (μS)
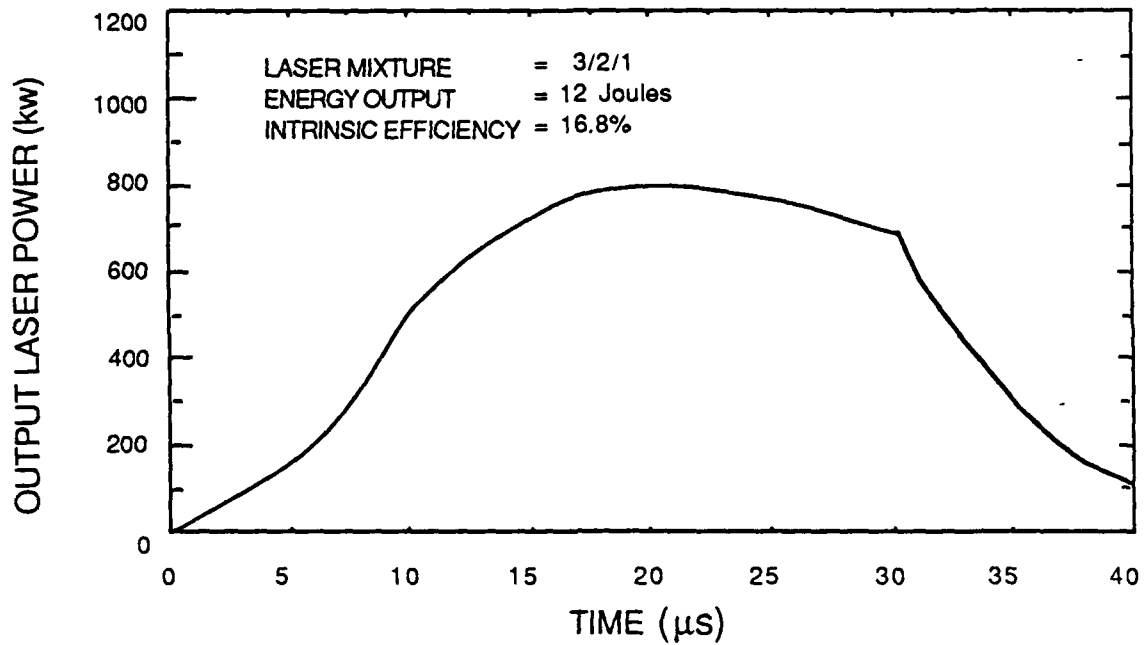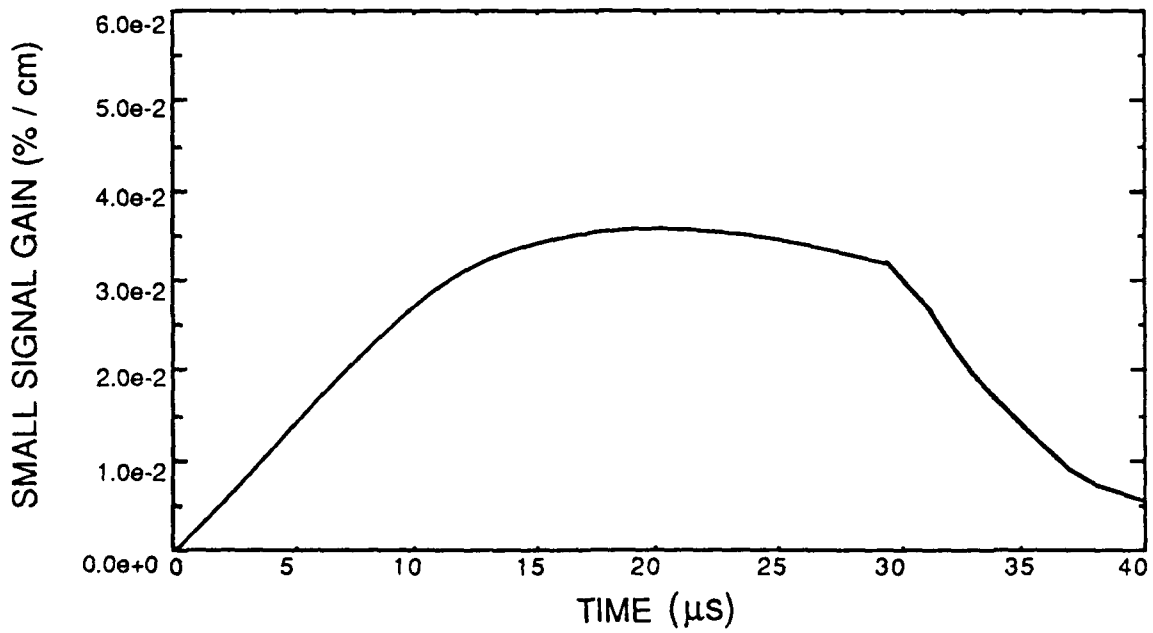
Figure 5.7: Curves showing the temporal small signal gain and output laser power of the CO_2 laser amplifier.

5-12

- Intrinsic Efficiency   16.7%

To calculate the optical extraction efficiency, SRL has used an existing expanding beam code. The inputs to this code are the small signal gain and saturation flux as predicted by the SRL CO_2 kinetics/laser code and the active medium geometry shown in Fig. 5.7. The output laser flux as predicted by the code is shown in the lower curve in Fig. 5.7. The peak output power is almost 800 kW, the integrated single pulse energy is 12 joules and the overall laser power extraction efficiency is 16.7%.

5.5 AMPLIFIED SPONTANEOUS EMISSION (ASE)

The stage gain of a CO_2 laser amplifier will be determined by constraints imposed by ASE. Hence it is important to model the ASE and to estimate the loss of efficiency imposed by this process. One can start by writing the intensity radiated from an elemental volume in the laser

$$\Delta\phi = N^*/\tau = g\phi_s = g_o\phi_s/(1 + \phi/\phi_s) \qquad (5.1)$$

ASE is just the amplification of $\Delta\phi$ along a given direction. The longest dimension, which is usually the laser length along the optical axis, will result in the largest ASE flux

$$\phi_{ASE} = \frac{g_o\phi_s}{4\pi} \int_o^L dr' \frac{\Omega}{(1 + \phi/\phi_s)} exp\Big\{g(r - r')\Big\} \qquad (5.2)$$

In Equation (5.2) Ω is the solid angle subtended by the radiation. From Eq. (5.2) it is clear that ϕ_{ASE} increases exponentially as the gain-length product gL increases. Numerical integration of Eq. (5.2) indicates that efficient laser power extraction from conventional CO_2 laser single pass amplifiers can be obtained up to stage gains of approximately 100.

The effects of ASE are exacerbated by the inhomogeneously broadened CO_2 laser transition in which hole burning on a few rotational lines leave spectral regions with high gain on adjacent rotational lines. ASE from these lines can deplete the inversion prior to collisional mixing into the hole burned regions and subsequent stimulated emission from these lines.

The effects of ASE on laser power extraction efficiency and stage gain are shown in Fig. 5.4. For the EBL amplifier configuration, curve 2 indicates that extraction efficiencies

SCIENCE RESEARCH LABORATORY

as high as 73% can be achieved at a stage gain of 1000 in the presence of ASE and a 1% specular reflection from the cavity windows or other elements within the optical train. This is very close to the extraction efficiency of 73.5% predicted by curve 1 which does not account for ASE. The relative insensitivity of the EBL amplifier to ASE is a direct result of the beam expansion which (1) reduces the intensity feedback from a specular reflection along an axial ray by a factor of 10 and (2) provides a stage gain of 1000 with an integrated gain along a ray of only 100. The remaining factor of 10 in the stage gain is given by the area expansion ratio. For a conventional single pass amplifier with the configuration shown in Fig. 5.6, Curve 3 indicates the relationship between stage gain and laser power extraction efficiency for no ASE, and Curve 4 indicates this relationship in the presence of ASE and a 1% specular reflection from the windows or other elements of the optical train. The precipitous decrease in laser power extraction efficiency for stage gains above 100 in a conventional single pass amplifier in the presence of ASE and a realistic value of specular reflection is clearly shown in Curve 4.

5.6 STEADY-STATE CONDUCTION COOLING

A critical requirement of a CO_2 laser is that of cooling. At a repetition rate of ν (Hz), an extraction of W (J/liter), a volume of V (liters) and an electrical efficiency of η, the amount of heat Q which must be carried away from the laser to maintain it at constant temperature is

$$Q = \frac{\nu W V}{\eta} \tag{5.3}$$

For example, for $\nu = 10$ Hz. $W = 25$ J/liter, $V = 5$ liters and $\eta = 0.1$, values typical of a 1-Atm CO_2 laser, one obtains $Q \approx 10$ kW. Carrying away this much heat requires a flow loop, which increases system weight substantially. In this section the alternative approach of *conduction* cooling will be addressed instead as an advanced concept to minimize the weight of the source laser. As shown in Fig. 5.8, the heat may be conducted away by the sidewalls along a direction perpendicular to the discharge direction. Conduction cooling is a viable option if the laser is operated at a low pressure and a correspondingly
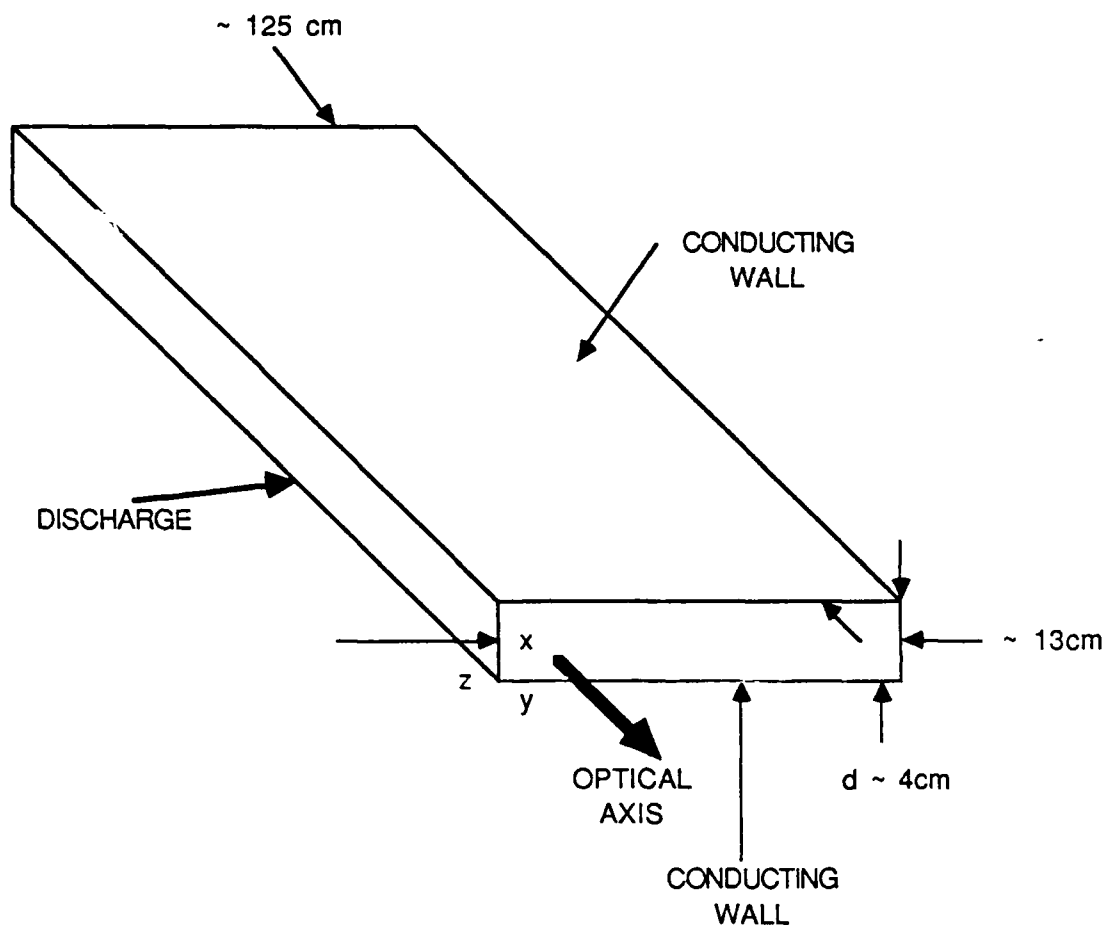
Figure 5.8: Geometry of laser

SCIENCE RESEARCH LABORATORY

low extraction. For example, for $W = 1$ J/liter, $V = 10$ liters, the repetition rate and efficiency mentioned above may be maintained with conduction cooling of only 1 kW. The sacrifices of lower extraction and increased laser-head volume are reasonable when they are linked to the much more significant weight and volume reduction made possible by the abandonment of flow cooling.

5.6.1 Conduction Equations

For a repetitively pulsed device the temperature, density and pressure all vary during each pulse. A repetitively pulsed CO_2 laser applicable to laser radar is expected to have pulses of width ~ 30 μsec. These pulses are so short that conduction within the laser gas may be ignored during each pulse. The equations coupling the temperature, density and pressure may then be reduced to a third-order equation for the density disturbance driven by the pulsed heating. The finite acoustic speed limits the response of density disturbances of scale sizes greater than ~ 1 cm during each pulse. Between pulses the situation is quite different, however. The pulses are far enough (~ 100 msec) apart for gaseous conduction of the heat to be significant. Since the rate of heat conduction is proportional to the temperature gradient, small-scale temperature gradients will tend to conduct away, leaving behind predominantly the largest-scale gradients. After a large number of such pulses, the laser will reach a quasi–steady state, in which the temperature and density are periodic in time with the period of the electrical pumping. In this limit, the effect of each individual electrical pulse on the beam quality is not expected to be severe. However, the cumulative effect of a large number of pulses, balanced against the conduction loss, is expected to lead to steady- state density and temperature profiles which significantly influence the wavefront of the laser beam. This steady-state effect may be calculated approximately by ignoring the pulsed nature of the excitation and treating it as if the heating is uniform in time, with the same average rate as that of the actual repetitively pulsed heating.

For heating which is uniform in time, the equation for the temperature T, including

the effect of thermal conduction of the gas, is

$$c_p \frac{\partial T}{\partial t} - \kappa \nabla^2 T = S \qquad (5.4)$$

where c_p is the specific heat (at constant pressure) per unit volume, κ is the thermal conductivity of the gas, and S is the heating rate per unit volume. Eq. (5.4) may be written in the alternative form[9]

$$\frac{\partial T}{\partial t} - D \nabla^2 T = \frac{S}{c_p} \qquad (5.5)$$

where $D = \kappa/c_p$ is the heat diffusivity, which scales as the product of the acoustic speed and the mean-free path between collisions. It is thus inversely proportional to the gas density. Therefore, if the heating source term S/c_p is kept constant as the density is decreased from 1 atm, the effect of heat conduction increases significantly. This may also be seen directly from Eq. (5.4): if one decreases the density and simultaneously decreases S proportionally, then since κ is independent of density the conduction term takes on increasing significance as the density is lowered.

An estimate of the efficacy of conduction cooling for relevant laser conditions may be made directly from Eq. (5.4). Consider a laser channel of dimensions 4×20 cm^2, with the surfaces separated by $d = 4$ cm maintained at constant temperature T_0. For a 3:2:1 He:N$_2$:CO$_2$ mix at 400°K, we have $\kappa = 1 \times 10^{-3}$W/cm°K. In this geometry the cooling is dominated by the effect of the walls spaced 4 cm apart. Neglecting the other walls, assuming a spatially uniform heat deposition, and taking the steady-state limit (T independent of time), one may integrate Eq. (5.4) analytically to obtain

$$\Delta T(x) = \frac{W \nu}{2 \kappa \eta} x(d - x) \qquad (5.6)$$

where x is the distance from one of the walls. At $\nu = 10$ Hz, $W = 10^{-3}$ J/c ^{3}, $\eta = 0.1$, Eq. (5.4) predicts a steady-state temperature rise of ~ 200 K halfway between the walls.

The 1 J/lit extraction, 10% efficiency and 10 Hz repetition rate will be taken to be the baseline parameters of a CO$_2$ laser amplifier to be used for laser radar. A preliminary

analysis indicates that the $d = 4$ cm spacing gives adequate conduction cooling at $\nu = 10$ Hz; therefore, unless otherwise noted, this spacing will be tentatively considered a baseline parameter, as well. It is anticipated that at higher repetition rates a smaller wall spacing will be required. An alternative, more conservative baseline, with $d = 2.4$ cm, will also be referred to in this report.

5.6.2   Thermal Effect of Pulsed Nature of Heating

One can also solve Eq. (5.4) for the temperature as a function of time, assuming that the energy deposition in the medium is uniform, and that the changes take place at constant pressure. One obtains a maximum temperature rise ΔT_m given by[10]

$$\Delta T_m = \Delta T_p \left[1 + \left(\frac{4}{\pi} \right) \left(\frac{1}{e^v - 1} - \frac{1}{3(e^{9v} - 1)} + \ldots \right) \right] \qquad (5.7)$$

In Eq. (5.7) $\Delta T_p = W/c_p \eta$ is the temperature rise due to a single-pulse energy deposition. and the dimensionless constant v is given by

$$v = \frac{\kappa}{\nu c_p} \left(\frac{\pi}{d} \right)^2 \qquad (5.8)$$

where c_p is the specific heat at constant pressure. For $d = 4$ cm, one obtains $v \approx 1.5$. $\Delta T_p \approx 210$ K, and $\Delta T_m \approx 300$ K.

Finally, it is useful to determine the rate at which temperature nonuniformities of different scale sizes are dissipated by thermal conduction between pulses. Let $\delta T_0(x)$ represent the nonuniform temperature rise at the end of a pulse. Expanding the temperature in Eq. (5.4) in spatial Fourier components yields during the time between pulses

$$c_p \frac{\partial \delta \tilde{T}(k)}{\partial t} + \kappa k^2 \delta \tilde{T}(k) = 0$$

with the solution

$$\delta \tilde{T}(k) = \delta \tilde{T}_0(k) e^{-\kappa k^2 t / c_p}$$

At a repetition rate of ν Hz. the pulses are separated by a time $t = 1/\nu$. Therefore the residual temperature rise of spatial frequency $k_n = \pi n/d$ due to a single previous pulse is

5-18

given by

$$\frac{\delta \tilde{T}_n}{\delta \tilde{T}_{0n}} = e^{-n^2 v} = \exp(\frac{-\kappa \pi^2 n^2}{c_p d^2 \nu})$$

where v is defined in Eq. (5.8), and $n = 1, 2 \ldots$ is an integer which characterizes the spatial frequency as a multiple of π/d. As discussed above, $v \approx 1.5$ when $d = 4$ cm. Therefore, the temperature component with the *lowest* spatial frequency ($n = 1$) supported by the channel decays by a factor of $\sim \exp(1.5) = 4.5$ between pulses. The component with the next lowest spatial frequency ($n = 2$) decays by a factor of $\sim \exp(6) = 400$ between pulses. Thus the small-scale- size nonuniformities quickly dissipate away between pulses, and *to* an excellent approximation only the largest-scale temperature nonuniformity needs to be taken into account.

5.6.3 Scaling of Conduction-Cooled Laser

Eq. (5.6) may be used to scale the laser size as a function of electrical power loading. The steady-state temperature T_c halfway between the walls may be expressed in terms of the electrical power loading $P' = W\nu/\eta$ as

$$T_c - T_0 = \Delta T = \frac{d^2 P'}{8\kappa} \tag{5.9}$$

Thus the temperature rise ΔT is proportional to the power loading and the square of the distance between the walls. This relationship is depicted graphically in Fig. 5.9, which shows the temperature rise as a function of the power loading for various values of channel width (wall separation).

The scaling with pulse repetition frequency (PRF) ν may be obtained by rewriting Eq. (5.9) in the form

$$d^2 = \frac{8\kappa}{(W/\eta)} \frac{T_c - T_0}{\nu} \tag{5.10}$$

In Fig. 5.10 the relationship between channel width and PRF is plotted for various values of temperature rise, assuming a single-pulse electrical energy loading W/η of 10 J/lit. It is seen that at 10 pps and a 4-cm channel width the temperature rise is 200°C.

5-19
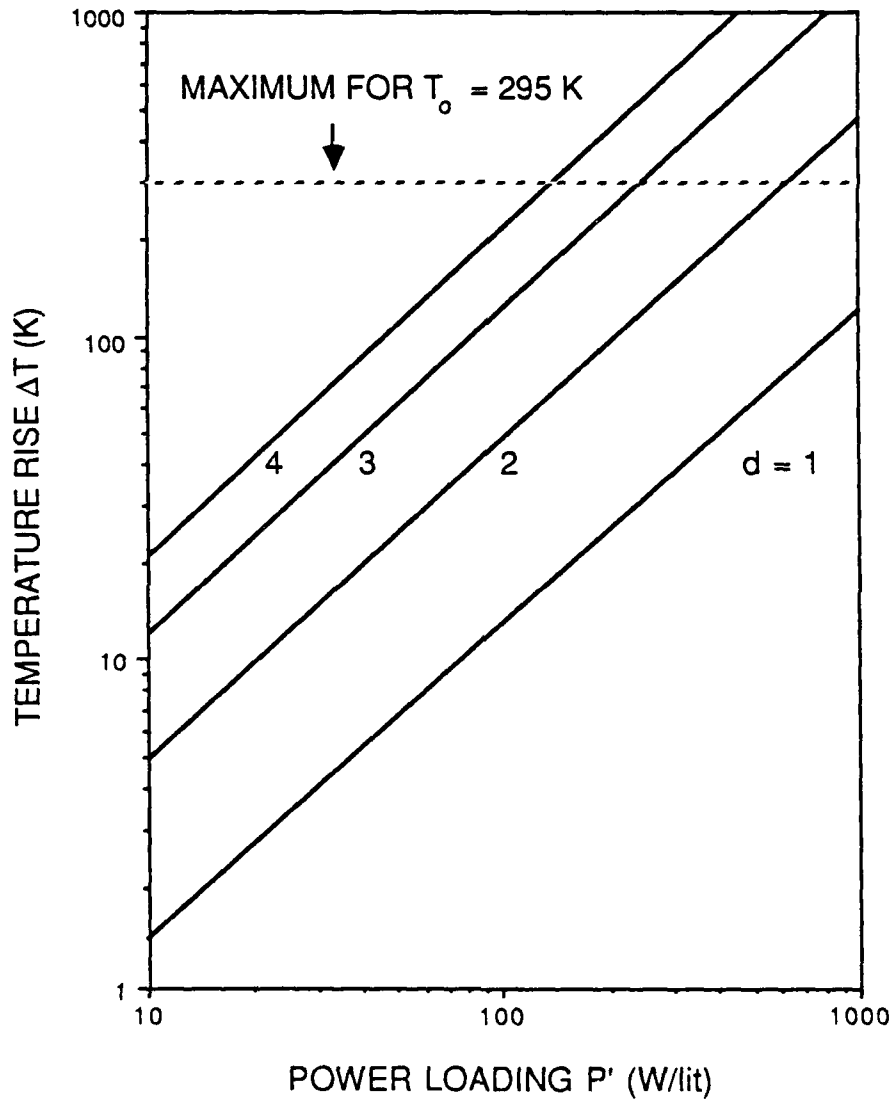
Figure 5.9: Temperature rise versus power loading for various channel widths

SCIENCE RESEARCH LABORATORY
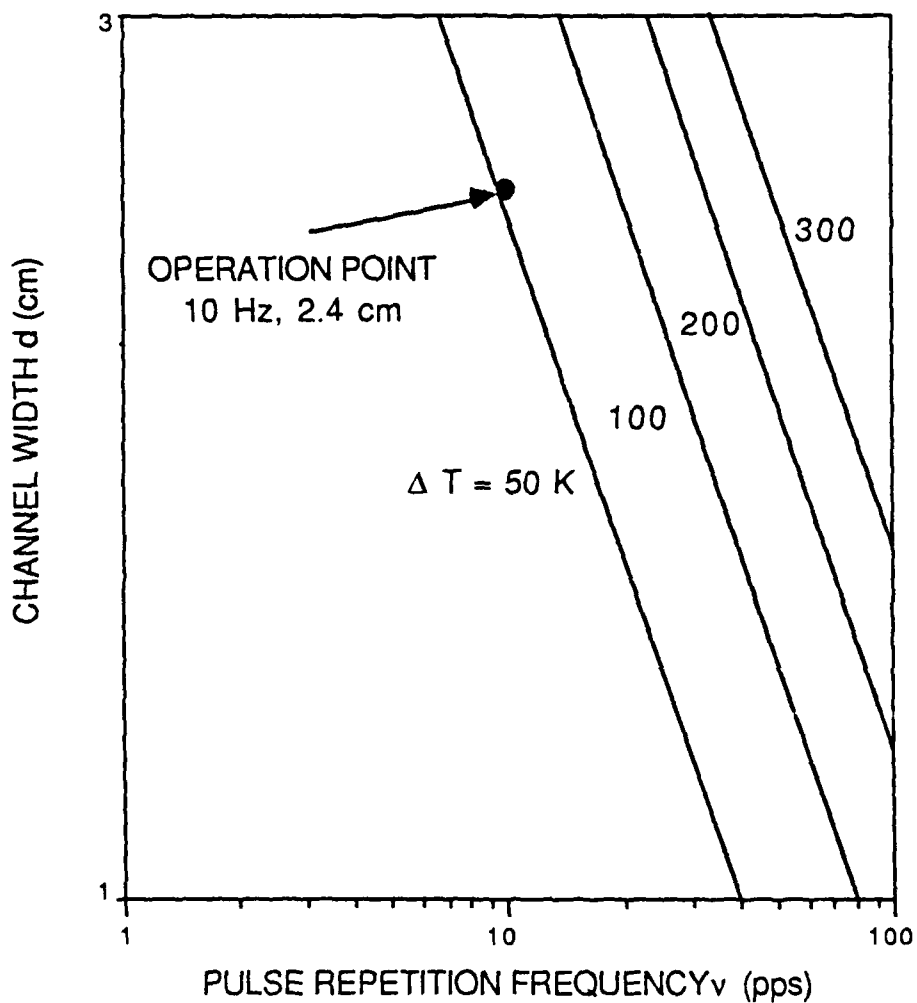
Figure 5.10: Maximum channel width versus PRF for various steady-state temperature rises

5-21

Higher repetition rates will require smaller channel widths in order to maintain the same temperature rise. Table 3 lists steady-state temperatures and transient temperature rises for a laser head with a more conservative 2.4-cm channel spacing operated at various pulse repetition rates (PRF's). At the highest PRF shown (50 Hz) it is necessary to maintain the channel walls at a temperature of 200°K (as indicated in Table 3) in order to prevent the gas from reaching temperatures at which the lasing efficiency would be degraded. The 200°K temperature is still well above the boiling point ($\sim$ 160-170°K) of CO_2 over the estimated pressure range (30-80 torr) which will apply during operation of the laser.

Table 3: Temperature Variation for 2.4-cm-Channel Laser Head

Repetition Rate (Hz)	Steady State Temperature (K)		Transient Temperature Rise (K)	
	At Electrode	At Channel Center	Peak	Beginning of Pulse
10	295	370	210	0
20	295	440	250	30
50	200	560	420	220

5.6.4 Impact of Conduction Cooling on Beam and Spectral Quality Width in the Steady State

In the preceeding section it was shown that for a uniform heat deposition, conduction cooling leads to a steady state with a quadratic temperature variation across the channel [see Eq. (5.6)]. The quadratic variation of the temperature will, via the equation of state, lead to a corresponding variation in density ρ:

$$\rho = A \left(T_0 + \frac{W \nu x (d - x)}{2 \kappa \eta} \right)^{-1} \tag{5.11}$$

where the constant A may be determined from the constraint that the mean value of ρ,

averaged over x, must be independent of the heating. The main aberration coming from this density variation will be a negative cylindrical focus along x, i.e., perpendicular to the channel walls. The associated radius of curvature R may be calculated from

$$\frac{1}{R} = \frac{\lambda}{4\pi}\nabla^2\phi \tag{5.12}$$

where λ is the wavelength, ϕ is the phase aberration, and $\nabla^2\phi$ is evaluated at $x = d/2$, halfway between the channel walls. The relationship between phase and density is

$$\phi = \frac{2\pi L_1}{\lambda}\frac{\beta_g}{\rho_A} \tag{5.13}$$

where β_g is the Gladstone-Dale constant (the refractive index minus unity at standard temperature and pressure [STP]) of the laser gas, ρ_A is the gas density at STP, and L_1 is the propagation length. Combining Eqs. (5.11)-(5.13) yields

$$\frac{1}{R} \approx \frac{8}{3}\frac{L_1}{d^2}\beta_g\frac{\rho_0}{\rho_A}\frac{\mu}{1+\mu} \tag{5.14}$$

where ρ_0 is the initial density of the gas, and μ is given by

$$\mu = \frac{T_c - T_0}{T_0} = \frac{W\nu d^2}{8\kappa\eta T_0} \tag{5.15}$$

Here T_0 is the wall temperature and T_c is the temperature at the center. The radius of curvature for a single pass through the amplifier ($L_1 = 125$ cm) when $\rho_0/\rho_A = 0.04$ and $\mu = 1$ is

$$R \approx 120 \text{ m}$$

which is reasonably large. For 4 passes through the amplifier, with no correction between passes, the radius of curvature would still be ~ 30 m, corresponding to ~ 0.03 Diopters. The cylindrical focus error can easily be compensated statically by giving the laser beam incident on the laser amplifier a cylindrical focus along x. If the amplifier utilizes an expanding beam geometry then the optics producing the expansion (perpendicular to x) will be in place, and all that will be needed is a small modification of these optics to produce

SCIENCE RESEARCH LABORATORY

the relatively small focus along x. Thus, the cylindrical focus, which is the dominant aberration due to the steady-state thermal loading, can easily be compensated and should produce no appreciable beam-quality degradation.

Higher-order aberrations due to the thermal loading may also be present if the electrical heating is not uniform along x. These may be estimated by taking the spatial Fourier transform of Eq. (5.4) in the steady state, yielding

$$T(k) = \frac{S(k)}{\kappa k^2} \tag{5.16}$$

The amplitude of the component of the temperature of spatial frequency k is thus shown to be proportional to the heating nonuniformity of the same spatial frequency and inversely proportional to the square of the spatial frequency. Therefore, as discussed above, small-scale nonuniformities of the steady-state heating do not produce strong temperature and density nonuniformities. The reason is that for a given temperature difference, heat is conducted more rapidly the smaller the scale size of the temperature difference. In the steady state the dominant density disturbance will always be the low-order cylindrical focus, which, as discussed above, is easily compensated. If it turns out to be necessary, it is also possible to compensate some of the higher-order aberrations by utilizing a static adaptive optic which may be adjusted in place to minimize the laser divergence.

It should be noted that the steady-state temperature and density profile distributions have no effect on the spectral purity of the laser. Only the pulsation of the heating, which causes time-dependent changes in the phase, can broaden the spectrum by producing chirp and frequency noise.

A preliminary analysis, sketched above, thus indicates that, as far as the steady state is concerned, conduction cooling to channel walls is a viable technique for carrying away the heat generated in a pulsed CO_2 laser amplifier operated at a low pressure (0.04 atm). The heat generated by each electrical pulse is sufficient to raise the temperature of the laser gas significantly, on the order of $\sim 300\,°C$. However, most of this heat conducts away to the walls between pulses. After several laser pulses, a quasi–steady-state temperature

SCIENCE RESEARCH LABORATORY

and density profile appears. It is comparable with the profile that one would obtain if the pulses were replaced by continuous heating at the same rate. The profile is dominated by a quadratic cylindrical focus which, for four passes through the amplifier, is expected to be $\sim$ 0.03 Diopters. This negative focus is transverse to the beam-expansion direction, and is easily removed with a slight modification of the focussing optics. It is noteworthy that the negative focus does not appear until the laser amplifier is operated for several pulses so that it reaches its steady-state thermal balance. Higher-order aberrations due to the steady-state heating are predicted to be small, since the temperature gradients which drive them are strongly dissipated by heat conduction. However, it is possible to remove these aberrations, as well, by utilizing a relatively simple static adaptive-optics system. The steady-state heating should have no effect on the spectral purity of the amplified laser beam.

5.7 ELECTRICALLY GENERATED DENSITY DISTURBANCES

The electrical energy used to pump the laser medium will unavoidably have some degree of spatial nonuniformity. This will result in the generation of acoustical and entropy disturbances, which will in turn produce refractive-index nonuniformities, an increased spectral width, and beam-quality degradation in the laser. Because the channel walls of the discharge-pumped laser are solid, there is no intrinsic spatial discontinuity in the pump-energy distribution, such as that which occurs in an e-beam-pumped laser.[11] Still, if the laser medium of interest, discharge-pumped by $\sim$ 10 J/lit in a $\sim$ 30-μsec pulse, were used as an oscillator, it would be extremely difficult to maintain the pumping uniform enough to make the oscillator beam quality and spectral quality acceptable. However, as will be shown, the beam-quality degradation and frequency noise are not so severe if the laser medium is used instead as an amplifier. It is expected that the dominant source of the discharge nonuniformities will be nonuniform UV preionization. It is thus possible to make the laser light average over the discharge nonuniformity by ensuring that the UV-preionizing structure changes along the direction of propagation of the laser light.

The distance over which this structure must change significantly in order to ensure good beam quality and frequency purity will determined in detail. In this report, a preliminary estimate of the requirements for good beam quality will be made.

5.7.1 Density Response to Nonuniform Pumping

The geometry of the laser is shown in Fig. 5.8. The dominant direction of discharge nonuniformity is expected to lie along the direction x transverse to the channel surfaces. Thus, the contributions of nonuniform pumping to density variations along the discharge direction y and the optic axis z may be neglected, and to a good approximation the perturbation ρ of the density satisfies a one-dimensional wave equation of the form[12]

$$\frac{\partial}{\partial t}\left(\frac{\partial^2}{\partial t^2} - u^2\frac{\partial^2}{\partial x^2}\right)\rho = (\gamma - 1)\frac{\partial^2 Q}{\partial x^2} \tag{5.17}$$

where $Q(x,t)$ is the heating rate, u is the speed of sound, and γ is the ratio of specific heats of the lasing gas. To determine the relevant characteristics of the solutions to these equations one may impose boundary conditions $\rho = 0$, $Q = 0$ at the walls $x = 0$, $x = d$, which imply that ρ and Q may be expanded in discrete Fourier series as

$$\begin{aligned}
\rho(x,t) &= \sum_n \rho_n(t)\sin(k_n x) \\
Q(x,t) &= \sum_n Q_n(t)\sin(k_n x)
\end{aligned} \tag{5.18}$$

where $k_n = \pi n/d$ ($n = 1, 2, \ldots$) are the allowed spatial frequencies. These are not the most general boundary conditions, but the pertinent characteristics of the solutions will not depend on the boundary conditions except as discussed specifically below.

Substituting Eq. (5.18) into Eq. (5.17) yields

$$\frac{\partial}{\partial t}\left[\frac{\partial^2}{\partial t^2} + (k_n u)^2\right]\rho_n = -(\gamma - 1)k_n^2 Q_n(t) \tag{5.19}$$

A reasonable approximation is to consider the heating rate to be constant over the interval $0 \le t \le \tau$, where τ is the pulsewidth of the electrical pumping. Thus, $Q(x,t)$ may be expressed as $H(x)/\tau$, where $H(x)$ is the total electrical single-pulse energy loading per

5-26

unit volume. Similarly, $Q_n(t) = H_n/\tau$. The solution of Eq. (5.19) during the pulse is then

$$\rho_n(t) = -\left(\frac{\gamma - 1}{u^2}\right) \bar{H} h_n \left[\frac{u k_n t - \sin(u k_n t)}{u k_n \tau}\right] \tag{5.20}$$

where $\bar{H}$ is the mean energy loading per unit volume, given by

$$\bar{H} = \frac{1}{d} \int_0^d H(x) \, dx \tag{5.21}$$

and

$$h_n = \frac{2}{d} \int_0^d \left(\frac{H(x)}{\bar{H}}\right) \sin(k_n x) \, dx \tag{5.22}$$

is the normalized n^{th} Fourier component of the energy loading distribution.

It is useful to consider the form of Eq. (5.20) in the short-time and long-time regimes. $k_n = \pi n/d$ is the frequency of the nth acoustic mode of the channel. For each mode n of wavelength $2\pi/k_n = 2d/n$, one may make the following two observations: (i) When not enough time has passed for a sound wave to have travelled across an acoustic wavelength ($u k_n t < 1$), $\sin u k_n t \approx u k_n t$ so that $\rho_n \sim t^3$. This is the well-known transient "t^3" regime of thermal blooming. (ii) For longer times ($u k_n t \gg 1$), corresponding to many acoustic transits across an acoustic wavelength, the blooming reaches the steady state, and ρ_n is instead proportional to t. Thus, the density will respond more strongly to small-scale energy-loading nonuniformities (with $u k_n \tau \gg 1$) than to larger-scale nonuniformities (with $u k_n \tau < 1$).

In the following, spatial averages (over x) will be denoted by $< \ldots >_x$, and time averages by $< \ldots >_t$. As will be shown in the next section, the beam quality is determined by the spatial variance of the density perturbation, averaged over the pulse. Using Eq. (5.20), the time-averaged variance may be expanded into its spatial Fourier components, with the result

$$<< \rho^2 >_x >_t = \frac{1}{2} B^2 \sum_n h_n^2 I_n \tag{5.23}$$

where B, which has the dimensions of a density, is given by

$$B = \left[\frac{(\gamma - 1)\bar{H}}{u^2}\right] \tag{5.24}$$

5-27

and $I_n = I(\theta = uk_n\tau)$ is the response function of the nth acoustic mode of the channel to the energy- loading pulse of length τ:

$$I(\theta) = \frac{1}{\theta^3}\left[\frac{\theta^3}{3} - 2\sin\theta + \frac{1}{2}\theta(1 + \theta\cos\theta) - \frac{1}{4}\sin 2\theta\right] \qquad (5.25)$$

The behavior of I as a function of the normalized pulsewidth θ is shown in Fig. 5.11. It is seen that the transition between the short- and long-time regimes is relatively sharp, and that a good approximation for the function $I(\theta)$ is

$$I = \begin{cases} \theta^4/252, & \text{if } \theta < 3; \\ \frac{1}{3}, & \text{if } \theta > 3. \end{cases} \qquad (5.26)$$

The t^4 dependence at short times corresponds to the t^6 dependence of ρ^2 implicit in Eq. (5.20), corrected for the fact that at a constant heating rate B^2 would be proportional to t^2.

5.7.2 Beam Quality

The energy loading nonuniformity and the density disturbance which it causes will in general not be independent of position z along the optic axis of the laser. In fact, the nonuniformities will occur in layers along z, with successive layers spatially uncorrelated with each other. The phase aberrations from each layer will therefore add randomly to one another, much like a random walk. The following calculation will concentrate first on the eff·ct of a single layer. The addition of many layers will be carried out subsequently.

The phase aberration $\phi(x,t)$ seen by a ray propagating along z across a single layer is directly proportional to $\rho(x,t)$:

$$\phi(x,t) = \alpha\rho(x,t) = \frac{2\pi L_0}{\lambda}\frac{\beta_g}{\rho_A}\rho(x,t) \qquad (5.27)$$

where L_0 is the correlation length along z (i.e., the thickness of the layer), λ is the wavelength of the laser light, β_g is the Gladstone-Dale constant (the difference between the refractive index of the amplifying medium and unity at standard temperature and pressure [STP]), and ρ_A is the density of the amplifying medium at STP. $\phi(r,t)$ may be
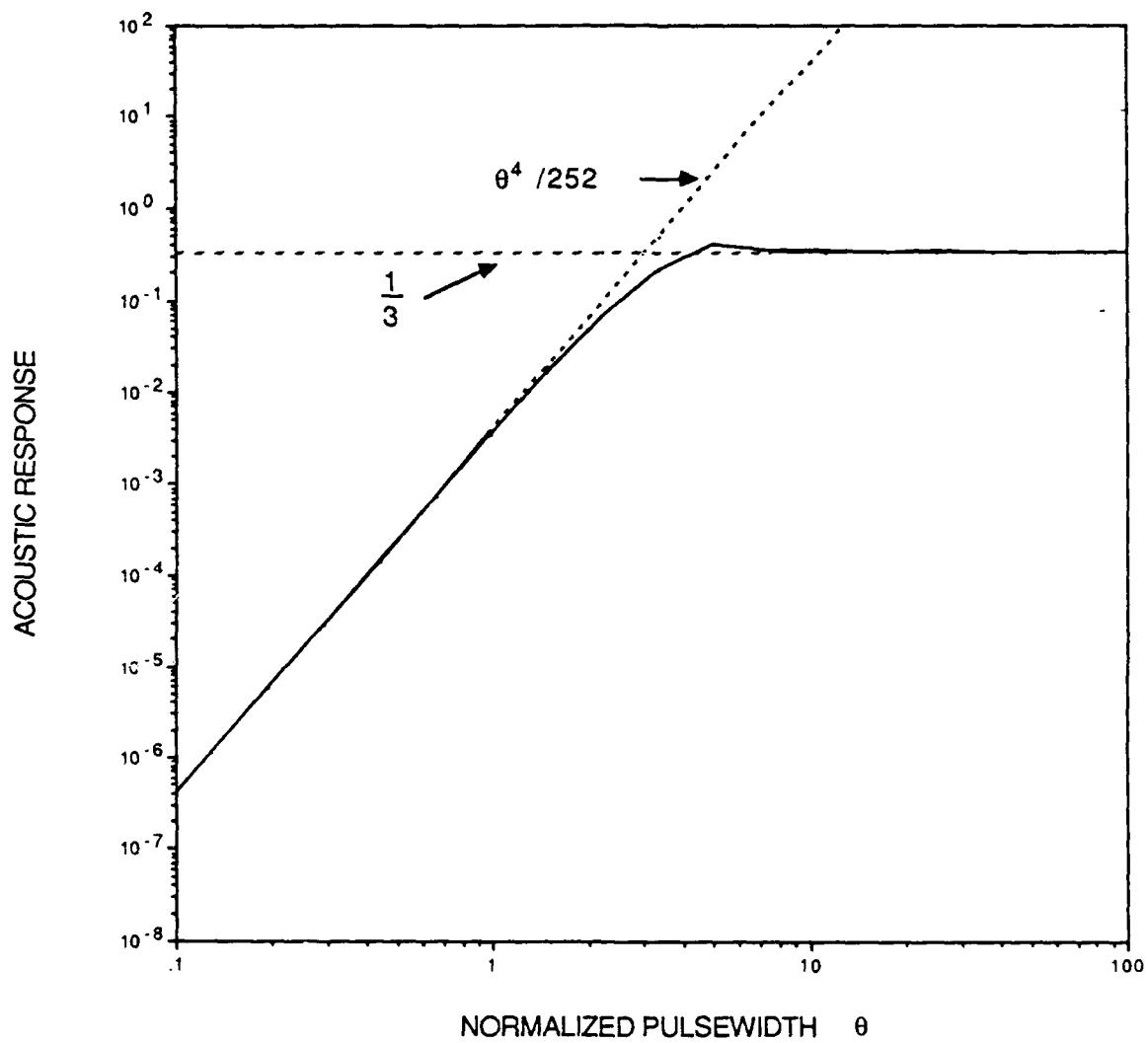
Figure 5.11: Acoustic response versus normalized pulsewidth

5-29

expanded in a Fourier series of the form

$$\phi(x,t) = \sum_n \phi_n(t) \sin k_n x \tag{5.28}$$

where $\phi_n = \alpha\rho_n$, and the spatial variance of the phase aberration, averaged over time, may similarly be expanded as

$$<< \phi^2 >_x>_t = \frac{1}{2}\Phi^2 \sum_n h_n^2 I_n \tag{5.29}$$

Here $\Phi = \alpha B$ is given explicitly by the following convenient expression:

$$\Phi = \frac{2\pi L_0}{\lambda}\beta_g \left(\frac{\gamma-1}{\gamma}\right)\left(\frac{\bar{H}}{p_A}\right) \tag{5.30}$$

where p_A is the standard pressure (1.01×10^5 Nt/m^2, or, in energy density units, 101 J/lit.) Note that Φ depends only on the energy loading per unit volume and the cell length; in particular, it is independent of pressure. However, at low gas pressures and correspondingly low energy loading, Φ can be reasonably low. A typical value of Φ is 0.31 radians at $L_0 = 5$ cm, $\lambda = 10$ μm, $\beta_g = 3 \times 10^{-4}$, $\gamma = 1.5$, and $\bar{H} = 10$ J/lit.

Beam quality is determined by the relative value of the peak far-field intensity, known as the Strehl ratio.[12] In principle, the Strehl ratio depends on both the phase and intensity nonuniformities in the near field. In practice, however, the contribution of the intensity nonuniformity to deviations of the Strehl ratio from unity is usually negligible. For the case at hand the Strehl ratio $S(t)$ may then be written as

$$S(t) = \left| < e^{i\phi(x,t)} >_x \right|^2 \tag{5.31}$$

where, as above, the brackets $< \ldots >_x$ denote a spatial average over the near-field beam (i.e., over x). Expanding the exponent in powers of ϕ yields

$$S(t) \approx 1 - \left(< \phi^2 >_x - < \phi >_x^2 \right) \tag{5.32}$$

to order ϕ^2. In general, one is interested in the temporal average of the beam quality. Let $\tilde{S}$ be the time average of $S(t)$. It follows from Eq. (5.32) that

$$\tilde{S} \approx 1 - << \phi^2 >_x>_t + << \phi >_x^2>_t \tag{5.33}$$

5-30

When $|\phi- <\phi>| \geq 1$ this approximation breaks down, and higher powers of ϕ must be included. If the energy-loading distribution satisfies Gaussian-normal statistics then the power series may be summed, yielding

$$\tilde{S} \approx \exp\left[- <<\phi^2>_x>_t + <<\phi>_x^2>_t\right] \tag{5.34}$$

[For other statistical distributions of the energy loading Eq. (5.34) is correct only to order ϕ^2; Eq. (5.34) and all subsequent equations describing beam quality should in general be considered to be correct only to this order.]

The presence of hard boundaries confining the gas in a fixed volume forces the mean density, averaged over x, to be a constant, independent of t. Therefore $<\phi>_x= 0$. Combining Eqs. (5.26), (5.29), and (5.30), one arrives at the following result:

$$\tilde{S} \approx \exp\left\{-\frac{1}{2}\Phi^2\left[\left(\frac{\pi u \tau}{d}\right)^4 \sum_{n<n_0} n^4 h_n^2 + \frac{1}{3}\sum_{n>n_0} h_n^2\right]\right\} \tag{5.35}$$

where

$$n_0 = \frac{3}{\pi}\frac{d}{u\tau} \tag{5.36}$$

is approximately the number of acoustic transits across the channel during the electrical pulse. By way of example, for $d = 4$ cm, $\tau = 30$ μsec, and $u \approx 400$ m/sec, the value of n_0 is ~ 3.2.

It should be noted that beam quality is often measured in "number of times diffraction limited" (XDL). The relationship between XDL and $\tilde{S}$ is

$$XDL = \frac{1}{\sqrt{\tilde{S}}} \tag{5.37}$$

so that Eq. (5.35) implies that

$$XDL \approx \exp\left\{+\frac{1}{4}\Phi^2\left[\left(\frac{\pi u \tau}{d}\right)^4 \sum_{n<n_0} n^4 h_n^2 + \frac{1}{3}\sum_{n>n_0} h_n^2\right]\right\} \tag{5.38}$$

The above results apply to the propagation through a single correlation length (along z) of the density disturbance. Since successive layers are spatially uncorrelated, the propagation through several correlation lengths results in the addition of the squares of the

5-31

phase errors. The generalizations of Eqs. (5.35) and (5.38) are thus

$$\tilde{S} \approx \exp\left\{-\frac{1}{2}\Phi^2\frac{L}{L_0}\left[\left(\frac{\pi u \tau}{d}\right)^4\sum_{n<n_0}n^4h_n^2 + \frac{1}{3}\sum_{n>n_0}h_n^2\right]\right\} \qquad (5.39)$$

and

$$XDL \approx \exp\left\{+\frac{1}{4}\Phi^2\frac{L}{L_0}\left[\left(\frac{\pi u \tau}{d}\right)^4\sum_{n<n_0}n^4h_n^2 + \frac{1}{3}\sum_{n>n_0}h_n^2\right]\right\} \qquad (5.40)$$

where L is the total distance travelled by the laser beam through the amplifier, so that L/L_0 is the number of correlation lengths traversed by the laser beam.

It is useful to break the right-hand side of Eq. (5.40) into two parts, as follows:

$$XDL \approx \exp\left\{+\frac{1}{4}\Phi^2\frac{L}{L_0}[\delta_L + \delta_S]\right\} \qquad (5.41)$$

where δ_L and δ_S are the contributions from large- and small-scale nonuniformities, respectively, in the electrical loading:

$$\begin{aligned}
\delta_L &= \left(\frac{\pi u \tau}{d}\right)^4\sum_{n<n_0}n^4h_n^2 \\
\delta_S &= \frac{1}{3}\sum_{n>n_0}h_n^2
\end{aligned} \qquad (5.42)$$

δ_L is the contribution of transient thermal blooming caused by large-scale nonuniformities (scale size $> u\tau$) in the electrical energy loading. Because of the factor of $(\pi u \tau n/d)^4$ in this term, it is generally small (see Fig. 5.10). On the other hand, δ_S is due to the steady-state thermal blooming caused by small-scale nonuniformities (scale size $< u\tau$) in the energy loading. Because of the relatively strong steady-state response of the medium to the smaller scales, it is δ_S which must be carefully monitored in the design of the laser amplifier.

A useful alternative expression for δ_S is

$$\delta_S \approx \frac{2}{3} < h_S^2 >_x = \frac{2}{3}[h_{S,rms}]^2 \qquad (5.43)$$

where $h_S(x)$ is the small-scale fractional modulation in the energy loading:

$$h_S(x) = \left.\frac{H(x) - \bar{H}}{\bar{H}}\right|_S \qquad (5.44)$$

5-32

Combining Eq. (5.44) with the definition of Φ yields

$$XDL \approx \exp\left\{+\frac{1}{6}\left(\frac{2\pi}{\lambda}\beta_g\frac{\gamma-1}{\gamma}\frac{\bar{H}}{p_A}\right)^2 LL_0[h_{S,rms}]^2\right\} \tag{5.45}$$

For a given required XDL, Eq. (5.45) may be used to determine the acceptable range of L_0 and rms variation in the energy loading. By way of example, for three passes through a 125-cm amplifier one has $L = 375$ cm. With $\lambda = 10$ μm, $\beta_g = 2 \times 10^{-4}$, $\gamma = 1.5$, and for $\bar{H} = 10$ J/liters, Eq. (5.45) reduces to

$$XDL \approx \exp\left\{+\frac{L_0(h_{S,rms})^2}{9}\right\} \tag{5.46}$$

where L_0 is in cm. Eq. (5.46) implies that energy-loading nonuniformities as large as $\sim 20 - 30\%$ rms are consistent with excellent beam quality (1.1 XDL) if the correlation length is of the order of 10 cm or less.

This preliminary analysis thus indicates that the requirements for little effect on beam quality from the acoustics driven by a single pulse are relatively easy to achieve. A more detailed analysis, including realistic deviations from Gaussian-normal statistics, will be carried out during.

5.7.3 Frequency Noise

A second important effect of the density changes during the pulse is changes in the frequency of the amplified laser light. In general, these frequency changes may be divided into two distinct parts: chirp and frequency "noise." The chirp ν_{ch} is the change in the instantaneous central frequency of the light, while the noise $\delta\nu$ is associated with deviations from the instantaneous central frequency, i.e., creation of Fourier components at other frequencies. For a laser amplifier with solid walls, the chirp should be nearly zero if the laser beam uniformly fills the entire region between the walls (i.e., if the laser intensity is independent of x). Deviations from uniformity may produce some chirp.

5.7.4 Mode-Medium Instability

Another effect that could in principle prove relevant to controlling the beam quality of a pulsed CO_2 laser is the mode-medium instability (MMI), which has been described in detail

in Ref. 11. The MMI is due to the interaction between the laser intensity distribution, the dependence of the heating rate on the laser inversion, the acousto-density response of the gaseous medium to the heating distribution, and the refraction/diffraction of light by the density disturbance.

It is anticipated that a CO_2 laser amplifier of the type used for laser radar will not suffer any significant loss from MMI. As was shown by Flusberg et. al., the instability is important in a laser oscillator,[12] but does not cause a loss of beam quality in a laser amplifier.[14,15] In addition, even in an oscillator, the rate at which the instability grows depends on density; at a density of 30-40 torr the degradation in oscillator beam quality should occur on a time scale of ~ 100 μsec, hence there should be no significant effect on the beam quality of a 30-μsec pulse.

5.7.5 Persistent Acoustic Disturbances

Another important effect on beam quality is that of persistent acoustic disturbances, which are created by the heat deposition during each pulse. Between pulses these disturbances relax from the combined effects of viscous damping in the gas and imperfect acoustic reflections from the solid boundaries. For a repetitively pulsed laser, each successive pulse "feeds" the various acoustic modes of the laser cavity. Each mode decays between pulses but is driven again by successive pulses. The result is a steady state between the driving impulses due to the pulsed heat deposition on the one hand and the damping by viscosity and finite reflectivity on the other. For a small enough wall reflectivity the acoustics should damp away so rapidly that no significant buildup should take place.

The effect of persistent acoustic disturbances will be analyzed, and the wall reflectivity loss required to limit the effect on beam quality will be determined.

5.8 ALL SOLID STATE RF CO_2 LASER PULSER

RF pulse generators with output powers of several tens of megawatts are not presently available in compact lightweight packages (i.e. < 30 kg). SRL proposes employing magnetic switches which will result in a compact, lightweight RF pulse generator capable of driving

the laser head discussed in the preceeding sections of this chapter.

The use of CO_2 lasers in laser radar has sparked new interest in improving the reliability of discharge lasers and their associated pulsed power drivers. Early attempts at driving the lasers directly with thyratrons or spark gaps have resulted in modulator lifetimes of only a few hundred hours. All-solid- state nonlinear magnetic drivers have greatly alleviated this problem. The use of nonlinear magnetic pulse compressor technology has allowed operation at repetition rates up to several kilohertz with greatly improved reliability and reduced maintenance. SCR-commutators combined with nonlinear magnetic pulser compressors allow for the development of an all solid state pulse generator. The basic principle underlying nonlinear magnetic driver operation involves using a saturable core which is an inductor in a resonant circuit. In the unsaturated state the saturable inductor exhibits a large inductance and once saturated the inductance is reduced by the change in permeability of the saturable core. This change in inductance is typically a factor of several thousand. The core is designed to saturate at the peak of the charging current waveform from the previous stage and once saturated rapidly transfers the stored energy to the following stage. In so doing the energy is conserved but temporally compressed resulting in increased peak power. This nonlinear saturation phenomenon shifts the frequency of this resonant circuit by the square root of the permeability shift as the core saturates. These stages are typically cascaded (Fig. 5.12) and energy is coupled faster and faster from one stage to the next.

A possible RF pulser design would be a frozen wave line to build an all solid state pulse power. A frozen wave line consists of a transmission line distributed into many isolated segments. These segments are individually charged to potentials corresponding to those of the desired output wave. The segments are then simultaneously connected together allowing the wave to propagate along the line to the laser load.

5.8.1   Conceptual Design of an All Solid State Pulser

The use of CO_2 lasers in laser radar has sparked new interest in improving the reliability
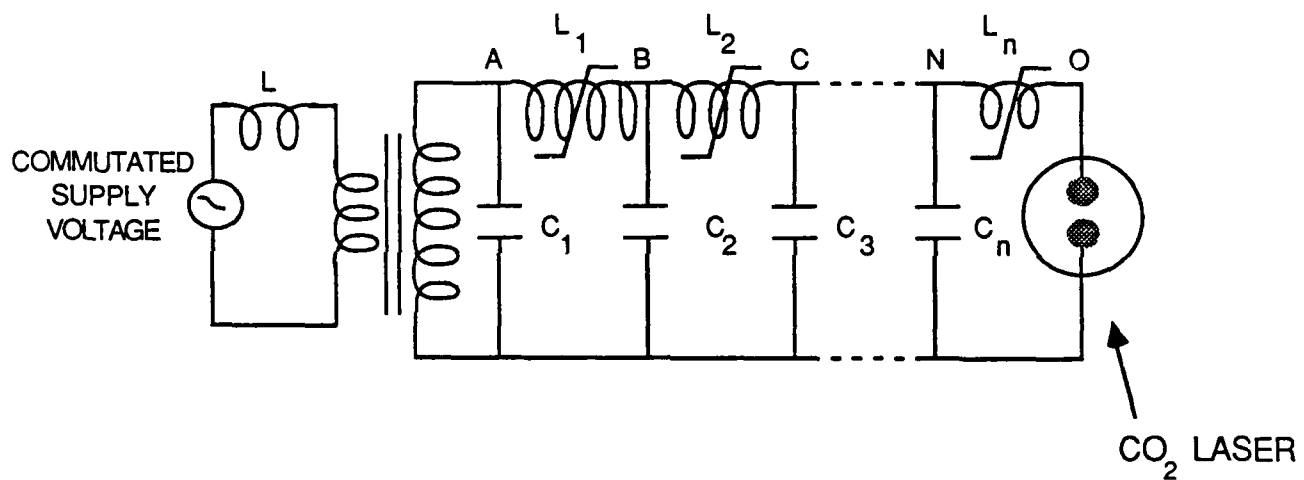
SCIENCE RESEARCH LABORATORY

Figure 5.12: Typical magnetic switch operation

of CO_2 lasers and their associated pulsed power drivers. Early attempts at driving the lasers directly with thyratrons resulted in significant energy dissipation in the thyratron which led to thyratron lifetimes of only a few hundred hours.

Nonlinear magnetic pulse compressors have greatly alleviated this problem. The output stages of these units are sufficiently rugged to dissipate the required fraction of the drive energy reflected from the nonlinear load. However, thyratrons are still used in many cases to supply the input commutation for these nonlinear magnetic pulse compressors and represent a weak link. The use of nonlinear magnetic pulse compressor technology has greatly eased the dI/dt problems for the thyratrons but the high average current still leads to a thyratron tube life which is unacceptable with respect to reliability and maintenance.

The use of solid state devices in place of thyratrons and spark gaps is the key to developing a reliable pulse power system. The nonlinear magnetic circuits which provide the necessary temporal compression are inherently reliable as they contain no active elements. Both high pressure (spark gaps) and low pressure (thyratrons) gas discharge devices have a finite lifetime. Electrode erosion with subsequent gas contamination and insulator degradation will eventually degrade the performance of these devices. SCRs like nonlinear magnetic compressors do not rely on plasma formation or material displacement to function. An SCR operating within its ratings will essentially last forever. Solid state devices were originally developed by Bell Laboratories for space based applications where maintenance was not possible. Solid state switches, however, will only operate outside their ratings once. They are not very forgiving in this respect, for exceeding the maximum voltage, rms current or dI/dt ratings even instantaneously will result in irreversible damage.

In this effort, Science Research Laboratory plans to exploit recent progress in Silicon Controlled Rectifier (SCR) and saturable core magnetic switch technology to develop all solid state RF drivers which meet all of the performance specifications for advanced, compact lightweight CO_2 laser radar systems. SCRs can be used in conjunction with metglass

saturable core magnetic switches to develop all solid state modules. In addition to the substantial SCR size advantage over thyratrons, SCRs do not require filament transformers, bias supplies and considerable other ancillary equipment. The SCRs size advantage is predominately derived from the increased density of conduction electrons in silicon as opposed to the low pressure gas in the thyratron. In addition these all-solid-state SCR-switched drivers can be engineered to operate for greater than 10^{11} shots at greater than 95% efficiency to minimize waste heat rejection.

The design of efficient high gain pulse compression stages relies on the careful control of the magnetic fields surrounding the core volume. Optimization of this packing factor is crucial in magnetic switch design and is accomplished by enclosing the core in a tightly fitting conducting housing. The multiple turns are formed as coaxial transmission lines which pass through this housing. Circulating currents set up in this housing exclude the magnetic flux and contain it in the desired volumes.

The design of efficient high gain pulse compression stages relies on the careful control of the magnetic fields surrounding the core volume. The losses in a compression stage are linearly proportional to the volume of core material used and it can be shown that the core volume requirement for this saturable inductor is given by:

$$\text{volume} = \text{gain}^2 \cdot \text{Pulse Energy} \cdot \left(\frac{\mu_o \cdot \pi^2}{4 \cdot (\Delta B_s \cdot \text{pf})^2} \right) \tag{5.47}$$

where ΔB_s is the available flux swing of the material (with appropriate biasing given by $+B_s - (-B_s) = 2B_s$), gain is defined as the temporal compression factor ($\tau_{charge}/\tau_{discharge}$), and pf is the packing factor. The packing factor is defined as

$$\frac{\int_{V_f} H^2 dv}{\int_{\text{all space}} H^2 dv} \tag{5.48}$$

where V_f is the actual volume occupied by the ferri- (ferro) magnetic core material excluding all interlaminar insulation and voids. Optimization of this packing factor is crucial in magnetic switch design and is accomplished by enclosing the core in a tightly fitting conducting housing. The multiple turns are formed as coaxial transmission lines which pass

SCIENCE RESEARCH LABORATORY

through this housing. Circulating currents set up in this housing exclude the magnetic flux and contain it in the desired volumes.

With the saturable material completely enclosed in conducting coaxial housings, the voltage per turn associated with the dB/dt of the core appears across a single narrow gap on the outside diameter of each housing. Connecting the coaxial transmission lines in the inner and outer housings with radial transmission lines across the top and bottom of the core completes the turns. The impedance of these transmission lines are adjusted so that

$$Z_{LINE} \approx \sqrt{\frac{2 \cdot L_{sat}}{C}} \tag{5.49}$$

while simultaneously every effort is made to minimize $L_{sat} \cdot C$ which is proportional to the square of the pulse length. Here L_{sat} and C refer to the saturated inductance of the reactor and the value of the storage capacitance respectively.

In addition to optimizing the core structure, increased SCR protection and efficiency is provided by grading the storage capacitors throughout the chain so that they gradually increase in capacitance in the direction of the output. This introduces a controlled level of voltage reversal per stage which acts to slow the progress of the reflected pulse by providing some reset. A reversed waveform cannot propagate efficiently back through a fully-reset pulser as long as the gain per stage exceeds a factor of two. Grading the capacitors in this manner also increases the efficiency. Core losses introduce a resistive component to the impedance which couples storage capacitors in each stage. Unless each successive capacitor is larger in value than its predecessor, this resistive term will cause positive charge to be left on the preceding capacitor after the discharge cycle is completed and will enhance propagation of pulses in the reverse direction.

SRL is herein proposing to apply this same technology to the challenge of generating RF pulses in a compact lightweight driver. This RF generator will be capable of supplying a 75 joule, 20 MHz RF pulse with a 30 μsec pulse duration at a repetition rate exceeding 100 pps.

SCIENCE RESEARCH LABORATORY

The basic concept of the frozen wave line was originally conceived over 50 years ago and is illustrated in Fig. 5.13. A pulse forming network is divided into multiple segments isolated by switches. The elements are charged from a DC supply in such a way that the desired output wave appears on the line. This wave is in essence frozen into the line and prevented from propagating down the line by the presence of the open switches. The switches are then closed simultaneously and the wave is propagates down the transmisssion line to the output terminals. While this idea appears simple enough, the switch technology has not existed until recently which could extend this concept to high power (megawatts) at high repetition rate (100 pps) in the frequency range of interest (10-20 MHz).

Recent developments in the field of nonlinear magnetic pulse compression technology provide a solution to the switching problem. Nonlinear magnetic pulse compression technology is now employed to drive CO_2 and rare gas halide excimer lasers, copper vapor lasers, and free electron lasers. These modulators have all generated DC pulses, but now we have identified two techniques whereby this technology can be employed to generate RF pulses.

The concept shown schematically in Fig. 5.14 uses two separate nonlinear, magnetically-switched charging networks which charge the isolated line elements to alternate polarities. Here the PFN network elements can be segments of transmission lines but the concept still applies in the case where simple capacitors replace these elements as shown. Transmission line segments have some advantages if a square wave output is desired as the individual discrete line segments can be center charged rather than end charged. Saturable inductors located between the elements are designed to saturate at the conclusion of the charging pulse thereby connecting all the elements of the line together and allowing the RF wave to propagate down the line to the output. This frozen wave generator design is a bit more complicated than the version described below but does allow for center charging and eliminates transformer coupling problems.

SCIENCE RESEARCH LABORATORY
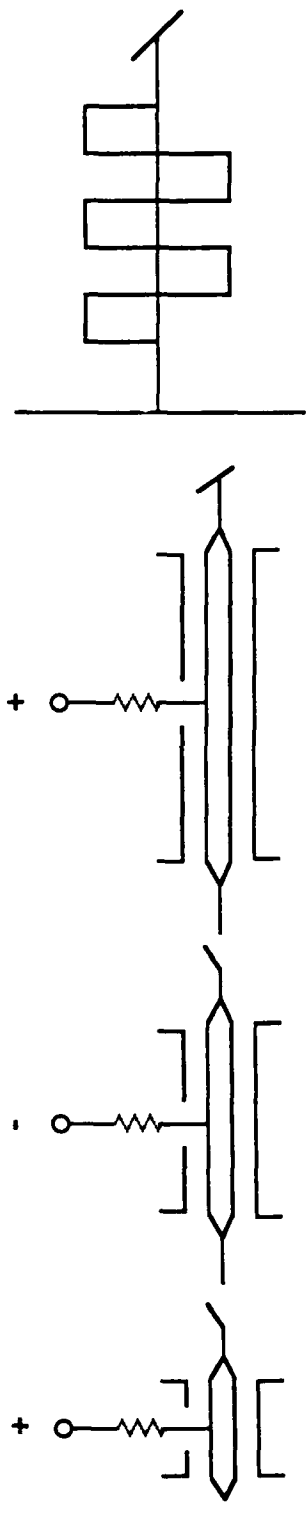
IDEAL FROZEN WAVE LINE USING TRANSMISSION LINE SEGMENTS
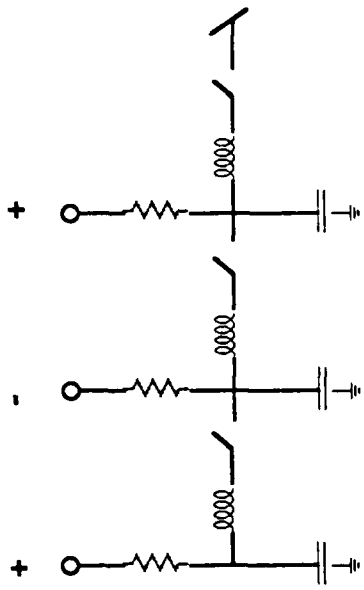
IDEAL FROZEN WAVE LINE USING LUMPED ELEMENTS

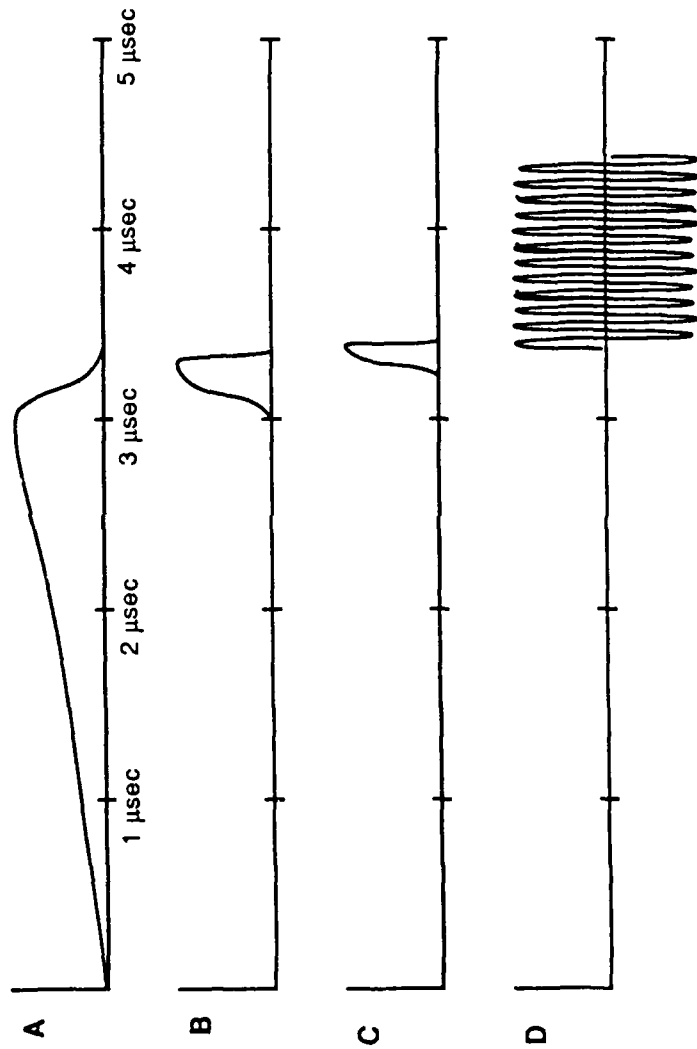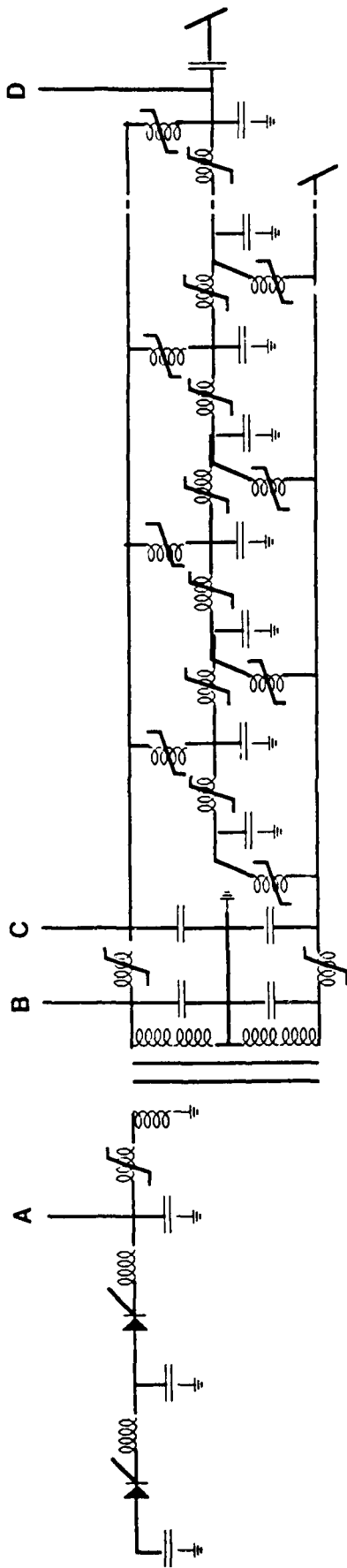Figure 5.13: Ideal frozen wave lines

Figure 5.14: Simplified schematic of frozen wave generator

The second concept illustrated in Fig. 5.15 uses saturable transformers between elements. The transformers are used to create the wave on the line while in the unsaturated state. At the conclusion of the charging pulse, the core material making up the transformers is designed to saturate. Once this saturation occurs, the line is decoupled from the nonlinear magnetic charging system and the saturated transformers now act as the inductors of a lumped element transmission line.
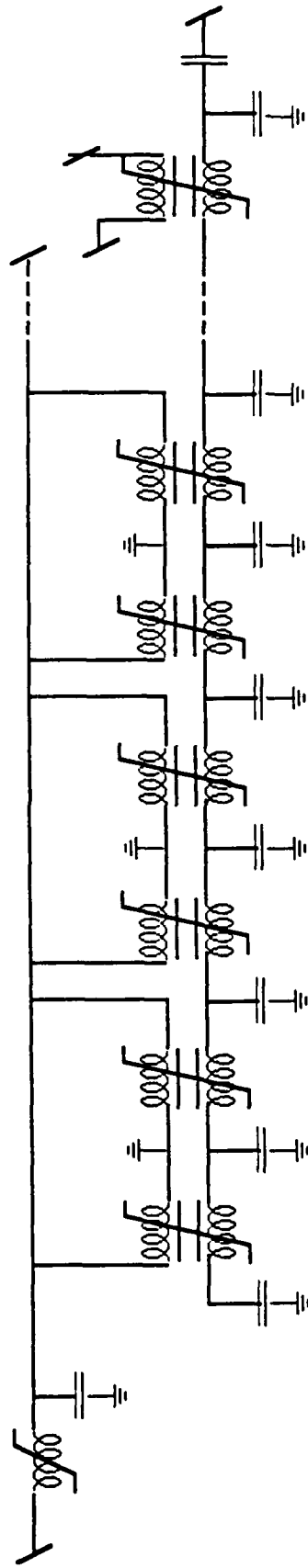
SCIENCE RESEARCH LABORATORY

Figure 5.15: Frozen wave line using saturable transformers

REFERENCES

1. W.L. Nighan, and W.J. Wiegand, Appl. Phys. Lett. 25, 633 (1974).

2. E.F. Jaeger, and A.V. Phelps, Bull. Am. Phys. Soc. 19, 147 (1974).

3. S.M. Meerkov, and G.I. Shapiro, Avtomatika i Telemekhanika (in Russian), 6, 12, (1976).

4. J.D. Daugherty, J.A. Mangano, and J.H. Jacob, Appl. Phys. Lett. 28, 581 (1976).

5. D.H. Douglas-Hamilton, Private communication.

6. D.H. Douglas-Hamilton and R.S. Lowder, Avco Everett Research Laboratory Kinetics Handbook (1974) unpublished.

7. C.E. Caldonia, et al., "Analysis of Metastable State Production and Energy Transfer", Report # AFWAL-TR-86-2078 (1986).

8. J.H. Jacob, M. Rokni, R.E. Klinkowstein and S. Singer "Expanding Beam Concept for Building Very Large Excimer Laser Amplifiers", Appl. Phys. Lett 48, 318, (1986).

9. H. Carlslaw and J. Jaeger, *Conduction of Heat in Solids, Second Edition*, Clarendon Press, Oxford, 1986.

10. J. Daugherty, "Electron-Beam Ionized Lasers," in *Principles of Lasers Plasmas*, edited by G. Bekefi, Wiley, 1976.

11. E. Pugh, J. Wallace, J. Jacob, D. Northam, and J. Daugherty, "Optical Quality of Pulsed Electron-Beam Sustained Lasers," *Applied Optics 13*, pp. 2512-2517, 1974.

12. A. Flusberg, D. Korff, T. Cronburg, and G. Theophanis, "Mode-Medium Instability in Pulsed CO_2 Lasers," *Proceedings, International Conference on Lasers '83*, STS Press, McLean, Virginia, 1983, pp. 503-511.

13. M. Born and E. Wolf, *Principles of Optics, Fourth Edition*, Pergamon Press, 1970, pp. 460–462.

14. G. Theophanis, A. Flusberg, and R. Litte, "Pulsed Electric Discharge Laser Technology Development Program, EDL Focusability, and Van Test," Avco Everett Research Laboratory Final Technical Report, U.S. Army Missile Command Directed Energy Directorate, 1984.

15. G. Theophanis, A. Flusberg, and D. Korff, "Pulsed Electric Discharge Laser Technology Development Program, Lost Energy Testing," Avco Everett Research Laboratory Final Technical Report, U.S. Army Missile Command Directed Energy Directorate, 1984.

SCIENCE RESEARCH LABORATORY